Master's thesis

NTNU
Norwegian University of Science and Technology
Faculty of Information Technology and Electrical Engineering
Department of Engineering Cybernetics

Kjetil Halse

Online Parameter Estimation for State of Health and State of Charge Estimation with Joint and Dual Extended Kalman Filters

Master's thesis in Cybernetics and Robotics
Supervisor: Damiano Varagnolo
Co-supervisor: Daniel Grübl and Walter Caharija
June 2024

NTNU
Norwegian University of
Science and Technology

Kjetil Halse

Online Parameter Estimation for State of Health and State of Charge Estimation with Joint and Dual Extended Kalman Filters

Master's thesis in Cybernetics and Robotics
Supervisor: Damiano Varagnolo
Co-supervisor: Daniel Grübl and Walter Caharija
June 2024

Norwegian University of Science and Technology
Faculty of Information Technology and Electrical Engineering
Department of Engineering Cybernetics

NTNU
Norwegian University of
Science and Technology

Abstract

In recent decades, lithium-ion batteries (LIB) have become the leading technology in energy storage. Due to their many advantageous properties, they are widely implemented in various applications. However, these batteries are not everlasting, nor are they the easiest to control safely. States such as State of Charge (SOC) and State of Health (SOH) are two critical conditions that are important to monitor for the safe and efficient use of the battery.

Various solutions exist for estimating these states, ranging from Coulomb-counting-based methods to more advanced Kalman filters and particle filters. Kalman filters, in particular, are a common method for estimating SOC. Different forms of SOH, such as capacity and resistance changes due to aging, can also be estimated using Kalman filters.

In this thesis, three variations of the Kalman filter are implemented. Because of the non-linear behavior of the battery, the extended type of Kalman filter is chosen, since this filter linearizes the non-linear system. The first implemented filter is the Extended Kalman Filter (EKF), which estimates SOC. The second filter is the Joint Extended Kalman Filter (JEKF), which is an expanded version of the EKF. In addition to estimating SOC, it also estimates SOH in terms of changes in capacity and internal resistance. The third implemented filter is the Dual Extended Kalman Filter (DEKF), an advanced type of JEKF that estimates the same states. All three filters, EKF, JEKF, and DEKF, are implemented in two versions using two different battery models: the Rint model and the Thevenin model. To assess their precision, the resulting implemented filters are evaluated against a reference capacity test performed on battery data.

Simulations and test cases performed on publicly available long-term battery data show good capacity estimation from the JEKF and DEKF with a margin of error of less than 5%. The tests also indicate a much better SOC estimation by JEKF and DEKF compared to EKF when the battery is aged. However, for a new battery, this difference is not present. The thesis concludes that DEKF, and especially JEKF, are useful filters for SOH estimation of LIB, not only because of the SOH estimation but also due to their SOC estimation capabilities when the battery ages.

Sammendrag

I de siste tiårene har litium-ion-batterier (LIB) blitt den ledende teknologien innen energilagring. På grunn av dens mange gode egenskaper blir de implementert i en rekke ulike applikasjoner. Dessverre er ikke batteriene evigvarende, og de er heller ikke de enkleste å kontrollere trygt. Derfor er det kritisk å overvåke tilstander som State of Charge (SOC) og State of Health (SOH) for å sikre trygg og effektiv bruk av batteriet.

Det finnes ulike metoder for estimering av disse tilstandene, fra Coulombmeter til mer avanserte Kalman-filtre og partikkelfiltre. Kalman-filtre er spesielt vanlige for estimering av SOC. I tillegg kan Kalman-filtre brukes til å estimere ulike aspekter av SOH, som endringer i kapasitet og intern motstand i batteriet.

I denne oppgaven er tre varianter av Kalman-filteret implementert. På grunn av batteriets ikke-lineære oppførsel er 'Extended' Kalman-filter valgt, siden dette filteret lineariserer det ikke-lineære systemet. Det første implementerte filteret er Extended Kalman Filter (EKF), som kun estimerer SOC. Det andre filteret er Joint Extended Kalman Filter (JEKF), som er en utvidet versjon av EKF. I tillegg til å estimere SOC, estimerer dette filteret også SOH i form av endringer i kapasitet og intern motstand. Det tredje implementerte filteret er Dual Extended Kalman Filter (DEKF), en avansert type JEKF som estimerer de samme tilstandene. Alle tre filtrene, EKF, JEKF, og DEKF, er laget i to versjoner ved bruk av ulike batterimodeller: Rint-modellen og Thevenin-modellen. Presisjonen til filtrene blir evaluert ved å sammenligne dem med resultatene fra en referansekapasitetstest utført på batteridata.

Utførte simuleringer på offentlig tilgjengelige langtids-batteridata viser at de implementerte filtrene estimerer kapasiteten godt, med en feilmargin på under 5%. Testene viser også til en mye bedre SOC-estimering fra JEKF og DEKF sammenlignet med EKF når batteriet er aldret. For et nytt batteri er denne forskjellen derimot ikke like mye til stede. Oppgaven konkluderer med at DEKF, og spesielt JEKF, er nyttige filtre for SOH-estimering av LIB, ikke bare på grunn av SOH-estimeringen, men også på grunn av deres forbedrede SOC-estimeringer når batteriet aldres.

Preface

This master's thesis is completed in the final semester of the master's program Cybernetics and Robotics at NTNU Trondheim. The work continues from the Specialization Project [1] done in the Fall semester of 2023, which primarily focused on state of charge estimation and was based on the work done in Dreyer Svendsen's Master Thesis, finalized in June 2023 [2]. Some parts of the theory mentioned in this thesis are based on the theory sections from my Specialization Project, with further modifications and clarifications.

To fully understand the content of this thesis, it is highly recommended to have prior knowledge in cybernetics, statistics, automation, and battery technology.

This work has been conducted with guidance from Siemens Energy. Their expertise and ongoing support have significantly contributed to the completion of this project and have motivated its practical application.

I want to thank my supervisor from NTNU, Damiano Varagnolo, for his support and guidance throughout both semesters. I am also deeply grateful to my co-supervisors from Siemens Energy, Daniel Grübl and Walter Caharija, for their weekly invaluable tips and advice, which ensured continuous progress in my work from start to finish.

Kjetil Halse
Trondheim, June 2024

Contents

Abstract i

Sammendrag ii

Preface iii

List of Figures xi

List of Tables xiii

Abbrevations xiv

1 Introduction **1**

1.1 Background 1

1.2 Previous work 2

1.3 Problem description 3

1.4 Contributions 3

1.5 Structure of the report 3

2 Lithium Ion Batteries **4**

2.1 Basics on lithium-ion battery 4

2.1.1 Capacity 7

2.1.2 State of Charge 7

2.1.3 State of Health 7

2.1.4 Open Circuit Voltage 8

2.1.5 Hysteresis 9
2.1.6 Polarization voltages 9
2.2 Aging mechanism 10
2.2.1 Capacity fade 10
2.2.2 Power fade - internal resistance 10
2.2.3 More specific aging 10
2.3 Battery modelling 11
2.3.1 Rint model 12
2.3.2 Thevenin model - RC1 13
2.3.3 Other battery models 14
2.3.4 Model the battery aging 14
3 State Estimations 15
3.1 Sequential probabilistic inference and the Kalman filter 15
3.2 Observability analysis for state estimation 16
3.3 Extended Kalman Filter 17
3.4 Combined state and parameter estimation 18
3.4.1 Joint Extended Kalman Filter 19
3.4.2 Dual Extended Kalman Filter 20
3.5 Root mean square and mean absolute error 23
3.6 Nonlinear least squares estimation 24
4 Method 25
4.1 State and parameter estimation implementation 25
4.1.1 Extended Kalman Filter 26
4.1.2 Joint Extended Kalman Filter 27
4.1.3 Dual Extended Kalman Filter 29
4.1.4 Tuning parameters 30

4.2 Observability analysis for the JEKF-RC1 32
4.3 Preparation of battery dataset 33
4.3.1 Modification to dataset 34
4.3.2 Battery reference capacity 34
4.3.3 OCV - SOC curve 35
4.3.4 Parameter identification 36
4.4 Test cases 38
4.4.1 Ground truth 38
4.4.2 Test case 1 - EKF versus Joint and Dual EKF 38
4.4.3 Test case 2 - SOH estimation 40
4.4.4 Test case 3 - Convergence of estimator 40
5 Results 41
5.1 Identified initial parameters 41
5.2 Identified OCV - SOC curve 42
5.3 Test case 1 - EKF versus Joint and Dual EKF 43
5.3.1 New cell 43
5.3.2 Aged cell 47
5.3.3 Capacity estimation error for new and aged cell 50
5.3.4 Internal resistance estimation new versus aged 51
5.4 Test case 2 - SOH estimation 52
5.4.1 Cell 13 - Skewed low room temperature 53
5.4.2 Cell 20 - Skewed high room temperature 55
5.4.3 Cell 21 - Skewed low 40°C 57
5.4.4 Cell 25 - Skewed high 40°C 59
5.5 Test case 3 - Convergence of estimator 61
5.5.1 Capacity estimates 61

5.5.2 Internal resistance Rint model 61
5.5.3 Internal resistance RC1 model 62
5.6 Computation time 62
6 Discussion 63
6.1 Comparison of SOC estimates - Test case 1 63
6.2 Comparison of SOH estimators - Test case 2 64
6.3 Convergence of estimation - Test case 3 65
6.4 Estimator computation time comparison 66
6.5 Further work 67
7 Conclusion 68
Bibliography 69

Figures

2.1 Visualization showing the discharge of a Lithium-Ion Battery cell [10]. 6

2.2 Relationship between OCV and SOC for three types of cell chemistries. NMC[2] and LFP[2], LCO (Section 5.2, this work). 8

2.3 ECM of the Rint model. 12

2.4 ECM of the RC1/Thevenin model. 13

3.1 Schematic of the EKF and JEKF. 19

3.2 Schematic of the Dual Extended Kalman filter. 23

4.1 Reference capacity test for all 28 cells in dataset [34]. 34

4.2 Bar plot showing first and last measured capacity for all the 28 cells. 35

4.3 Measured voltage during slow discharge - charge test. 35

4.4 Low current approximation OCV curve of the cell. 36

4.5 Pulsed discharge test. 37

4.6 Extract from current, voltage and temperature measurements for new cell 21. . 39

4.7 Extract from current, voltage and temperature measurements for aged cell 21. . 39

5.1 Least square algorithm solving parameter fitting to R and RC1 model. 41

5.2 Comparison of SOC estimation using EKF-R, JEKF-R, and DEKF-R for new cell number 25, operated at an ambient temperature of 40°C. 43

5.3 Comparison of SOC estimation using EKF-RC1, JEKF-RC1, JEKF-RC1-Ext, and DEKF-RC1 for new cell number 25, operated at an ambient temperature of 40°C. See Table 5.2 for estimation errors. 44

5.4 SOC estimation error bar chart for new cell number 25. 44

5.5 Comparison of output voltage estimation using EKF-R, JEKF-R, and DEKF-R for new cell number 25, operated at an ambient temperature of 40°C. 45

5.6 Comparison of output voltage estimation using EKF-RC1, JEKF-RC1, JEKF-RC1-Ext and DEKF-RC1 for new cell number 25, operated at an ambient temperature of 40°C. 45

5.7 Output voltage estimation bar chart for new cell number 25. 46

5.8 Comparison of SOC estimation using EKF-R, JEKF-R, and DEKF-R for aged cell number 25, operated at an ambient temperature of 40°C. 47

5.9 Comparison of SOC estimation using EKF-RC1, JEKF-RC1, JEKF-RC1-Ext and DEKF-RC1 for aged cell number 25, operated at an ambient temperature of 40°C. 47

5.10 SOC estimation error bar chart for aged cell number 25. 48

5.11 Comparison of Output Voltage Estimation using EKF-RC1, JEKF-RC1, JEKF-RC1-Ext and DEKF-RC1 for aged cell number 25, operated at an ambient temperature of 40°C. 48

5.12 Comparison of output voltage estimation using EKF-RC1, JEKF-RC1, JEKF-RC1-Ext and DEKF-RC1 for aged cell number 25, operated at an ambient temperature of 40°C. 49

5.13 Output voltage estimation bar chart for aged cell number 25. 49

5.14 Capacity estimation for new cell. 50

5.15 Capacity estimation for aged cell. 50

5.16 Estimated R_0 for new cell test case 1 for JEKF-R and DEKF-R. 51

5.17 Estimated R_0 for new cell test case 1 for JEKF-RC1 and DEKF-RC1. 51

5.18 Estimated R_0 for aged cell test case 1 for JEKF-R and DEKF-R. 51

5.19 Estimated R_0 for aged cell test case 1 for JEKF-RC1 and DEKF-RC1. 51

5.20 Comparison of capacity estimates from JEKF and DEKF against reference capacity test for cell number 13. 53

5.21 Simulation results for estimated R_0 using JEKF-R and DEKF-R filter of cell number 13, compared to least square estimates. 53

5.22 Simulation results for estimated R_0 using JEKF-RC1 and DEKF-RC1 filter of cell number 13, compared to least square estimates. 54

5.23 Simulation results for estimated R_0 and R_1 using JEKF-RC1-Ext filter of cell number 13, compared to least square estimates. 54

5.24 Simulation results for estimated C_1 using JEKF-RC1-Ext filter of cell number 13, compared to least square estimates. 54

5.25 Comparison of capacity estimates from JEKF and DEKF against reference capacity test for cell number 20. 55

5.26 Simulation results for estimated R_0 using JEKF-R and DEKF-R filter of cell number 20, compared to least square estimates. 55

5.27 Simulation results for estimated R_0 using JEKF-RC1 and DEKF-RC1 filter of cell number 20, compared to least square estimates. 56

5.28 Simulation results for estimated R_0 and R_1 using JEKF-RC1-Ext filter of cell number 20, compared to least square estimates. 56

5.29 Simulation results for estimated C_1 using JEKF-RC1-Ext filter of cell number 20, compared to least square estimates. 56

5.30 Comparison of capacity estimates from JEKF and DEKF against reference capacity test for cell number 21. 57

5.31 Simulation results for estimated R_0 using JEKF-R and DEKF-R filter of cell number 21, compared to least square estimates. 57

5.32 Simulation results for estimated R_0 using JEKF-RC1 and DEKF-RC1 filter of cell number 21, compared to least square estimates. 58

5.33 Simulation results for estimated R_0 and R_1 using JEKF-RC1-Ext filter of cell number 21, compared to least square estimates. 58

5.34 Simulation results for estimated C_1 using JEKF-RC1-Ext filter of cell number 21, compared to least square estimates. 58

5.35 Comparison of capacity estimates from JEKF and DEKF against reference capacity test for cell number 25. 59

5.36 Simulation results for estimated R_0 using JEKF-R and DEKF-R filter of cell number 25, compared to least square estimates. 59

5.37 Simulation results for estimated R_0 using JEKF-RC1 and DEKF-RC1 filter of cell number 25, compared to least square estimates. 60

5.38 Simulation results for estimated R_0 and R_1 using JEKF-RC1-Ext filter of cell number 25, compared to least square estimates. 60

5.39 Simulation results for estimated C_1 using JEKF-RC1-Ext filter of cell number 25, compared to least square estimates. 60

5.40 Estimated capacity for *new* cell in test case 3. 61

5.41 Estimated capacity for *aged* cell in test case 3. 61

5.42 Estimated R_0 for *new* cell in test case 3 for JEKF-R and DEKF-R. 61

5.43 Estimated R_0 for *aged* cell in test case 3 for JEKF-R and DEKF-R. 61

5.44 Estimated R_0 for *new* cell in test case 3 for JEKF-RC1 and DEKF-RC1. 62

5.45 Estimated R_0 for *aged* cell in test case 3 for JEKF-RC1 and DEKF-RC1. 62

Tables

2.1 Charging and discharging reactions in a Li-Ion Battery for general cell chemistries. M is a metal, often CO, Fe, Ni, or Mn. 6

4.1 Initial tuning state and covariances. 30

4.2 Tuned process noise parameters. 30

4.3 Tuned measurement noise parameters. 31

4.4 Summary of the seven battery test procedures from NASA Randomized Battery Usage [34]. 33

5.1 Identified coefficients for the OCV and dOCV curves. 42

5.2 Calculated RMSE and MAE SOC estimation errors for new cell number 25. . . . 44

5.3 Calculated RMSE and MAE output estimation errors for new cell number 25. . . 46

5.4 Calcultated RMSE and MAE SOC estimation errors for aged cell number 25. . . . 48

5.5 Calcultated RMSE and MAE output estimation errors for aged cell number 25. . 49

5.6 Capacity estimation error for new cell. 50

5.7 Capacity estimation error for aged cell. 50

5.8 Capacity estimation errors cell 13 (RMSE and MAE). 53

5.9 Capacity estimation errors cell 20 (RMSE and MAE). 55

5.10 Capacity estimation errors cell 21 (RMSE and MAE). 57

5.11 Capacity estimation errors cell 25 (RMSE and MAE). 59

5.12 Average computation time per iteration for the implemented Kalman filters using Matlab, and simulation setup from 4.4. 62

Abbrevations

Ah	Ampere hours
BMS	Battery Management System
CC-CV	Constant Current - Constant Voltage
DEKF	Dual Extended Kalman Filter
DOD	Depth of Discharge
ECM	Equivalent Circuit Model
EKF	Extended Kalman Filter
JEKF	Joint Extended Kalman Filter
LCO	Lithium Cobalt Oxide
LIB	Lithium-Ion Battery
LFP	Lithium Iron Phosphate
MAE	Mean Absolute Error
MMSE	Minimum Means Squared Error
NMC	Nickel Manganese Cobalt
OCV	Open Circuit Voltage
RMSE	Root Mean Square Error
SOC	State of Charge
SOH	State of Health

Chapter 1

Introduction

1.1 Background

In recent years, lithium-ion batteries (LIBs) have become a critical and essential component across a broad spectrum of technologies. They are foundational in powering everything from vehicles and vessels to smaller devices such as flashlights and mobile phones. The constantly improving efficiency and increased capacity of these batteries have paved the way for expanded uses, such as energy storage systems for various applications. For example, storing energy from renewable sources in large battery packs allows for the supply of electricity during periods of high demand, effectively balancing the energy grid and enhancing the reliability of renewable energy systems.

The demand for efficient energy storage is escalating, especially as reliance on renewable energy sources like wind and solar power continues to grow. These sources provide fresh energy that must be consumed or stored immediately. This need is captured in the assertion that "The Renewable-Energy Revolution Will Need Renewable Storage" [3], highlighting the critical role of storage solutions in maximizing the benefits of renewable energy.

The use of LIBs to store energy from renewable sources directly supports the United Nations Sustainable Development Goals, particularly Goal 7: 'Affordable and Clean Energy', and Goal 13: 'Climate Action'. The LIBs enable the storage of energy generated from renewables, such as solar and wind energy, reducing reliance on fossil fuels. This promotes environmental sustainability by lowering greenhouse gas emissions and enhancing energy access, making it more reliable and affordable globally. Therefore, the development of large-scale, well-functioning LIB systems plays a crucial role in transitioning to a more sustainable energy infrastructure.

LIBs have become the preferred choice for rechargeable batteries in a wide range of applica-

tions. This preference is largely due to their high energy density, which allows them to store more energy in a compact size. Additionally, they have a low self-discharge rate, meaning they retain their charge well over time [4].

When working with LIBs, it is crucial to monitor certain key states to ensure their effective and safe operation. One such state is the State of Charge (SOC), which indicates the remaining energy stored in the battery. Understanding the SOC helps in managing the energy supply and preventing over-discharge, which can damage the battery. Another vital parameter to monitor is the State of Health (SOH). The SOH provides insight into the condition of the battery, indicating how much the battery's capacity has diminished over time and how much its internal resistance has increased. Monitoring the SOH is essential for predicting the battery's lifespan and ensuring its reliability [5].

1.2 Previous work

Over the past decades, significant research has focused on state estimation techniques for LIBs. Various methods have been developed to accurately estimate the SOC and the SOH of these batteries, which are critical for their efficient and safe operation.

One of the most extensively studied techniques is the Kalman filter. Different variations of Kalman filters, such as the Extended Kalman Filter (EKF), Unscented Kalman Filter (UKF), and Sigma Point Kalman Filter, have been applied to estimate the SOC with success. Particle filters have also demonstrated strong performance in SOC estimation due to their ability to handle non-linearities and non-Gaussian noise [6].

In the work by Dreyer Svendsen [2], the precision of the EKF is highlighted. This study compares the EKF to a Sigma Point Kalman Filter and a Moving Horizon Estimator, demonstrating the advantages and limitations of each method in different scenarios.

Research by [7] investigates the changes in battery model parameters over time. The study finds that the capacitance in a modeled RC element generally decreases, and the internal resistance increases as the battery ages. Furthermore, it is shown that lower temperatures increases internal resistance and decrease capacitance, which can significantly impact the performance and lifespan of the battery.

1.3 Problem description

The accurate estimation of the SOC and SOH in LIBs is a critical challenge in battery management systems (BMS). As the battery ages, the inconsistency of an estimator becomes apparent, potentially leading to safety risks.

Most existing estimators either focus solely on SOC or do not account for the gradual changes in battery capacity and internal resistance, which are key parameters for SOH estimation. The challenge is further compounded when trying to maintain accuracy across a wide range of operating conditions and over the entire lifespan of the battery.

This thesis addresses these challenges by implementing and evaluating online estimators that can simultaneously estimate SOC and SOH. By utilizing the capabilities of the Joint Extended Kalman Filter (JEKF) and the Dual Extended Kalman Filter (DEKF), this work aims to provide a solution that maintains consistent accuracy in both health and charge estimation simultaneously for new and aged batteries, ensuring reliable performance throughout the battery's operational life. The performance of these estimators will be compared with a standard Extended Kalman Filter (EKF) that estimates only SOC and not SOH, serving as a benchmark.

1.4 Contributions

This thesis provides insights into the effectiveness of an online estimator, specifically using different versions of the EKF, in simultaneously estimating the SOC and SOH of LIBs. By using datasets for LIBs under various load conditions and temperatures over their entire lifespan, this research offers a comprehensive evaluation of the EKF's performance in real-world scenarios.

1.5 Structure of the report

The thesis is structured as follows. In Chapter 2, the theory surrounding LIB will be presented, including how to model these batteries. Chapter 3 introduces estimation techniques, focusing on different Kalman filters for state and parameter estimation. Chapter 4 walks through the methods used, from the implementation of the SOC and SOH estimators to the preparation of a battery dataset. In Chapter 5, results from different test cases will be presented, followed by a discussion in Chapter 6. The final chapter, Chapter 7, concludes the main findings from the work.

Chapter 2

Lithium Ion Batteries

This chapter covers the fundamental and essential theories related to lithium-ion batteries (LIBs) that are crucial for understanding the subsequent material in this report. It will explain how LIBs store energy and how the voltage varies in different modes such as charging, discharging, and in open-circuit conditions. The chapter will then delve into battery modeling techniques, from the basic Rint model to the more advanced Thevenin model. Note that parts of this chapter are similar to the theory chapter from the specialization project [1], written by the same author.

The first section will explain the basics of LIB theory, including the construction of the cell and definitions such as capacity, State of Charge (SOC), State of Health (SOH), and how the cell voltage depends on the SOC. The next section will describe some aging mechanisms in the cell, followed by a section in battery modeling.

2.1 Basics on lithium-ion battery

The reason for the widely adopted use of LIBs is their exceptional space and weight efficiency compared to other types of rechargeable battery cells on the market, such as Nickel-Cadmium (NiCd) or Nickel-Metal Hydride (NiMH) cells. LIBs also have a superior low self-discharge rate, which indicates how much the battery drains when not in use. Additionally, LIBs can be manufactured in a wide range of sizes and shapes, making them suitable for a variety of applications, from powering electric vessels to flashlights.

The LIBs are created by connecting one or more lithium-ion cells in series or parallel, depending on the desired current or voltage for the application. Multiple batteries can then be connected in series or parallel to create a battery module. For instance, if one has a 3.3V bat-

tery cell, it can be assembled into a ≈100V module by connecting 30 cells in series. The current specification for the module with cells in series is the same as for a single cell. To accommodate higher current demands, multiple modules can be connected in parallel, allowing the total current to be the sum of the currents from all the modules. For example, if each module provides a maximum current of 10A, connecting 10 modules in parallel would result in a total maximum current of 100A.

A LIB consists of a positive electrode called the "cathode," made of "$LiMO_2$," where M represents a type of metal, and a negative electrode called the "anode," often made of graphite (C, carbon) due to its low potential and safety [8]. Different cathodes have varying properties. Three commonly used cells are Nickel Manganese Cobalt (NMC), Lithium Iron Phosphate (LFP), and Lithium-Cobalt Oxide (LCO). The LFP cell uses $LiFePO_4$ as the cathode, the NMC cell has a cathode made of $LiNiMnCoO_2$, and the LCO cell features a cathode made of Lithium Cobalt Oxide($LiCoO_2$). The cells used in the dataset later in this thesis are LCO cells.

Each of these cell types has different characteristics regarding performance and degradation. LFP cells are known for their excellent thermal stability and long cycle life, making them highly resistant to degradation. However, they typically have a lower energy density compared to NMC and LCO cells. NMC cells strike a balance between energy density, safety, and longevity, offering higher capacity than LFP cells but with slightly faster degradation over time. LCO cells have high energy density and are commonly used in consumer electronics. However, they tend to degrade faster than LFP and NMC cells, especially under high load conditions and elevated temperatures [9].

Inside the cell, the two electrodes are separated by a separator that allows lithium ions to flow freely while blocking the flow of electrons. This setup forces the electrons to travel through an external circuit, creating an electric current. Additionally, there is an electrolyte through which the lithium ions move (see Figure 2.1 for visualization).

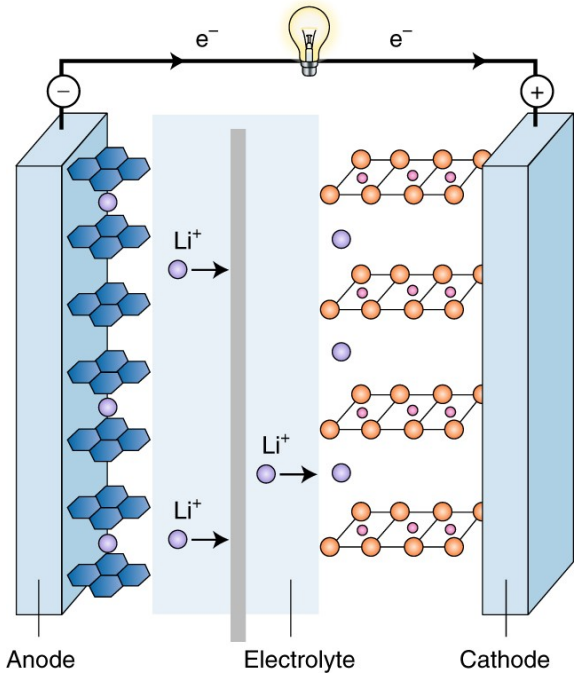

Figure 2.1: Visualization showing the discharge of a Lithium-Ion Battery cell [10].

	Charge	**Discharge**
Anode (-)	$C_6 + \mathrm{Li}^+ + e^- \rightarrow \mathrm{LiC}_6$	$\mathrm{LiC}_6 \rightarrow C_6 + \mathrm{Li}^+ + e^-$
Cathode (+)	$\mathrm{LiM}O_2 \rightarrow \mathrm{Li}^+ + \mathrm{MO}_2 + e^-$	$\mathrm{Li}^+ + \mathrm{MO}_2 + e^- \rightarrow \mathrm{LiM}O_2$
Total	$\mathrm{LiM}O_2 + C_6 \rightarrow \mathrm{LiC}_6 + \mathrm{MO}_2$	$\mathrm{LiC}_6 + \mathrm{MO}_2 \rightarrow \mathrm{LiM}O_2 + C_6$

Table 2.1: Charging and discharging reactions in a Li-Ion Battery for general cell chemistries. M is a metal, often CO, Fe, Ni, or Mn.

During the charging process of the cell, a current is pushed through the positive terminal, causing electrons to flow toward the negative terminal. Within the cell, the following occurs: at the cathode, Li^+ ions are liberated, accompanied by the release of electrons. These electrons travel through the external circuit to the anode, while the Li^+ ions pass through the separator to reach the anode. At the anode, these ions react and form LiC_6. The chemical equation illustrating this process is shown in Table 2.1.

Conversely, during the discharging process, connecting a load between the terminals allows current to flow, and the reaction essentially reverses the charging process. To sum up, during discharging, Li^+ ions flow inside the cell, and electrons flow outside the cell through a conducting material (wire) when the battery is in use. The direction of the current depends on the load, determining whether the cell is charging or discharging.

2.1.1 Capacity

The capacity of a battery describes its ability to store and deliver energy, typically measured in ampere-hours (Ah). It indicates how much charge a fully charged battery can deliver. For example, a fully charged battery with a capacity of 10 Ah can deliver a current of 10 Amperes for one hour, at a discharge rate of 1C. At a discharge rate of 2C, it delivers 20 Amperes for 30 minutes. The C rate denotes the speed of battery charging or discharging. For instance, 1C signifies a charging or discharging time of one hour, while 0.5C corresponds to a duration of two hours ($\frac{1}{0.5C} = 2h$).

Determining the charging time is not always straightforward, as the actual capacity changes over time and is influenced by factors such as temperature, charging/discharging rate, State of Health (SOH), and other variables. The capacity of the battery is denoted as $q(t)$, while the total capacity is denoted as Q.

2.1.2 State of Charge

The State of Charge (SOC) of a battery is closely related to its capacity and is expressed as a scalar value ranging from 0 to 1 (0% to 100%), given by:

$$\text{SOC}(t) = z(t) = \frac{q(t)}{Q} \tag{2.1}$$

The SOC describes how much energy is currently available in a battery as a percentage of its full capacity. It is a crucial state to monitor and control to ensure the battery is used and managed most efficiently.

2.1.3 State of Health

The State of Health (SOH) of a battery describes its condition compared to when it was new. The definition of SOH can vary, but it is commonly expressed as a percentage, where 100% indicates that the current capacity is equal to the nominal capacity (a new, fully functional battery).

$$\text{SOH} = \frac{Q_{\text{Ah, current}}}{Q_{\text{nominal}}} \cdot 100\% \tag{2.2}$$

Here, $Q_{\text{Ah, current}}$ is the current capacity of the battery, and Q_{nominal} is the nominal capacity of the battery when new.

SOH can also be calculated based on the internal resistance of the battery. As the battery ages, its internal resistance tends to increase, which affects its performance.

2.1.4 Open Circuit Voltage

The open circuit voltage (OCV) is defined as the voltage of the LIB when it is at rest. At rest refers to the state when there is no load connected, meaning there is no current flow through the cell. The OCV of the battery is mainly a function of SOC, where typically a higher SOC leads to a higher OCV. This means that if the function OCV(SOC) is known, and the cell is at rest, it is possible to get an approximation of the SOC by measuring the OCV. When a load is connected to the cell, the voltage will change immediately because of the internal resistance, and other chemical effects. This effect makes it challenging to measure the SOC when the cell is in use. The OCV is also influenced by temperature, SOH, and other factors [11], which again makes it harder to estimate the SOC. Figure 2.2 shows the approximated OCV-SOC relationship from three different types of cell chemistries. It can be seen that not all cells are straightforward to estimate SOC from the OCV since the curve is flat in the middle area.

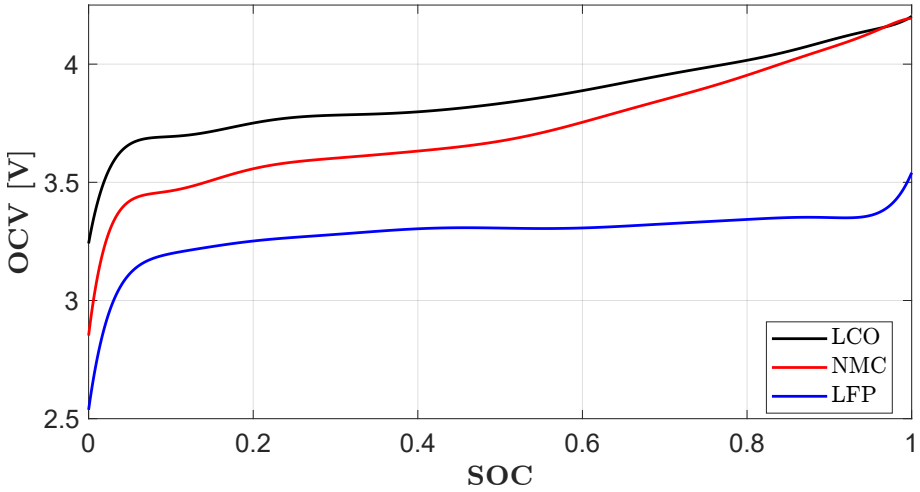

Figure 2.2: Relationship between OCV and SOC for three types of cell chemistries. NMC[2] and LFP[2], LCO (Section 5.2, this work).

There are several ways to determine the OCV(SOC) function. One way is to do a low current test [6]. A normal approach for this type of test is to discharge a fully charged cell at a very slow rate, for example at the rate of C/25 (25 hours). When the current is this low the terminal voltage will be very close to the actual OCV at this SOC. It is also advantageous to do the same test, but in reverse, meaning charge the cell from 0% to 100 % at the same rate and find the average OCV. Another way to find the function is to do an incremental OCV-SOC test, which charges the cell for a certain amount of charge, and then lets the cell rest for a while, measures the voltage, and does this until the cell is fully charged. Then the measured points

can interpolate to get the approximated OCV for the whole SOC span 0 - 100 %. The OCV - SOC relationship does change both with temperature and aging, but these changes are generally very small [7].

2.1.5 Hysteresis

In LIBs, hysteresis is a phenomenon resulting from internal chemical dynamics, causing the voltage response to depend on previous states. For example, if a battery is being discharged and then switches to charging, the voltage will differ compared to a scenario where it has been charged, paused, and then charged again. This behavior indicates that the voltage is not solely a function of the current SOC but also of the battery's charging and discharging history.

2.1.6 Polarization voltages

Polarization voltage in a LIB occurs when there is a flow of electrons. It is described as the deviation of the cell's terminal voltage from its OCV due to current flow through the battery [12].

The polarization voltage in the battery is expressed as:

$$V_{\text{polarization}} = V_{\text{terminal}} - V_{\text{ocv}} \tag{2.3}$$

This is the difference between the OCV of the battery and the measured voltage at the terminals. After a long rest period for the battery, the polarization voltages drop to zero [13], allowing the OCV to be measurable at the terminals.

This polarization voltage can be divided into multiple components:

$$V_{\text{polarization}} = V_{\text{ohmic}} + V_{\text{concentration}} + V_{\text{electrochemical}} \tag{2.4}$$

Ohmic polarization is instantaneous and disappears when the current is zero. In contrast, concentration and electrochemical polarization can persist for some time before they return to zero [14]. Understanding the behavior of these voltage components and incorporating them into the battery model will improve the performance of prediction filters. Accurately modeling these voltages allows for more precise estimation.

2.2 Aging mechanism

As batteries are used, their capabilities and specifications change, leading to performance degradation until they no longer meet the required standards. The two main measures of aging are *capacity fade* and *power fade*. LIBs are complex chemical systems, and their aging process is even more intricate. The fade in capacity and power results from various processes and interactions, rather than a single cause [15]. Aging occurs primarily in the anode and the cathode, although the LIB electrolyte also ages, particularly where it contacts the electrodes.

2.2.1 Capacity fade

Capacity fade in batteries is understood as the gradual reduction in the battery's ability to store charge, leading the total capacity the battery can hold to decrease. This phenomenon results from complex electrochemical processes within the battery. A few aspects that lead to this fade are cyclic aging, which occurs due to the repeated charge and discharge cycles that a battery undergoes. Calendric aging, which is when the batteries degrade over time. Other factors such as depth of discharge (DOD) and temperature influence how fast the degradation and capacity fade happen.

DOD is a measure of how much of the battery's capacity is used relative to its total capacity, expressed as a percentage. Higher DOD values indicate deeper discharges, which can accelerate the aging process and contribute to capacity fade.

2.2.2 Power fade - internal resistance

Power fade in batteries is characterized by a decreased ability to deliver power. Since resistance and power in the cell are tightly coupled, increased internal resistance is often referred to as power fade [16]. The primary degradation leading to power fade is the increasing internal resistance within the battery. As batteries age and undergo repeated charge and discharge cycles, their power capability declines. This decline occurs due to various processes affecting different parts of the battery, including the active materials, electrolytes, and separators, all of which deteriorate over time.

2.2.3 More specific aging

Aging in LIB involves complex processes at both the positive and negative electrodes. In the negative electrode, aging is predominantly characterized by the formation of a solid-electrolyte interphase (SEI) layer, which forms during initial charging and continues to grow over time,

causing a decrease in cell capacity and an increase in resistance. At the positive electrode, aging typically results from the dissolution of metal ions such as manganese or cobalt, leading to a loss of active material and, consequently, reduced battery capacity. Additionally, both electrodes experience structural changes and degradation due to cycling stresses, such as phase transitions and electrolyte decomposition, which further diminish the battery's performance and lifespan.

2.3 Battery modelling

To help predict and estimate the SOC, SOH, and other internal states of a battery, appropriate models of the battery cells are beneficial. In this section, the two most commonly used models will be presented. There are many types of models, and their complexity, performance, and accuracy vary. Therefore, it is essential to choose the best-fitting model for the given application.

The primary goal of an Equivalent Circuit Model (ECM) is to replicate a battery's characteristics as accurately as possible. This includes predicting how the terminal voltage will respond to changes in SOC and various operating conditions. Consequently, the model should account for the polarization voltages present within the battery to ensure that it provides an accurate representation of the terminal voltage.

Common for all the models is the state $z(t)$, which is the SOC at time t. The current, $i(t)$, acts as the known input to the system. The OCV($z(t)$) is a nonlinear function (pre-modeled) that provides the OCV of the battery at a given SOC (see Section 2.1.4).

All the models are based on the **Coulomb counting** method, a straightforward equation that integrates the current over time [17].

$$\Delta Q = \int \eta(t) i(t)\, dt \tag{2.5}$$

The above equation 2.5 can further be formulated in relation to SOC as follows:

$$z(t) = \text{SOC}(t) = \text{SOC}(0) - \frac{1}{Q} \cdot \int_0^t \eta(t) \cdot i(t)\, dt \tag{2.6}$$

Here, η is the charge/discharge efficiency, which depends on temperature and the C-rate. η is a number in the range $[0, 1]$, often close to 1. While it is possible to calculate the SOC solely from this model, it is not recommended. This model is open-loop, relying on the initialization and current measurements. Current sensors are not known for their high precision, leading to

potential deviations in the calculations. Additionally, the capacity Q must be known and accurate for the calculations to be reliable. The accuracy of Coulomb counting is heavily dependent on the initial value SOC(0) and the precise knowledge of Q, as indicated in Equation 2.6.

2.3.1 Rint model

The most simple ECM is the *Rint model* (R model), for internal resistance [18]. The Rint model consists of a non-linear voltage source V_S and a resistor R_0. The internal resistance (R_0), models the voltage drop within the battery when current flows through it, namely the ohmic polarization (2.1.6). This model does not have very high accuracy and does not have any way to describe the other polarization voltages inside the LIB [18], but it offers simplicity in return.

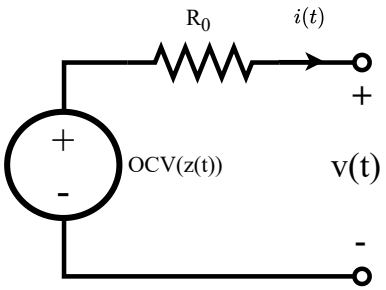

Figure 2.3: ECM of the Rint model.

The dynamic equations of this model are as follows:

$$\dot{z}(t) = -\frac{i(t)}{Q} \tag{2.7}$$

$$v(t) = \text{OCV}(z(t)) - R_0 i(t) \tag{2.8}$$

where z is the SOC, Q is the total capacity [Ah], $i(t)$ is the current flowing through the battery, and $v(t)$ is the voltage across the battery terminals.

To use this model in an online discrete estimator, the equations need to be discretized:

$$z_{k+1} = z_k - \frac{\Delta t}{Q} i_k \tag{2.9}$$

$$v_k = \text{OCV}(z_k) - R_0 i_k \tag{2.10}$$

2.3.2 Thevenin model - RC1

The Thevenin model (1RC / RC1) builds upon the Rint model by adding an RC network in series with R_0. The purpose of the RC network is to simulate the other polarization voltages, as mentioned in Section 2.1.6. There are also ECMs that incorporate multiple RC circuits in series to model the different polarization effects. However, a significant drawback of this approach is the increasing complexity in model parametrization, which becomes more cumbersome as additional RC circuits are added.

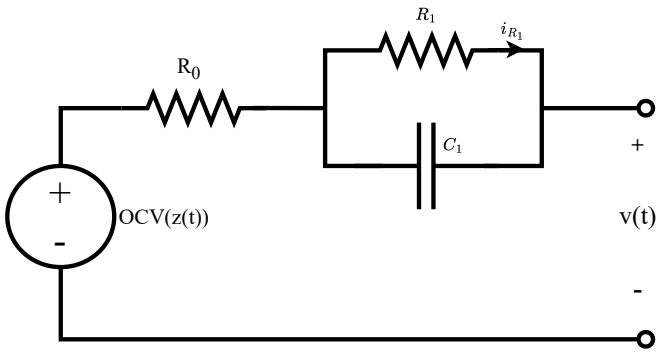

Figure 2.4: ECM of the RC1/Thevenin model.

The dynamic equations of this model are as follows:

$$\dot{z}(t) = -\frac{i(t)}{Q} \tag{2.11}$$

$$\dot{i}_{R_1}(t) = -\frac{1}{R_1 C_1} i_{R_1}(t) + \frac{1}{R_1 C_1} i(t) \tag{2.12}$$

$$v(t) = \text{OCV}(z(t)) - R_0 i(t) - R_1 i_{R_1}(t) \tag{2.13}$$

Compared to the Rint model, the Thevenin model introduces the state $i_{R_1}(t)$, representing the current through R_1 in the RC network, which captures the transient response of the battery due to polarization effects.

Discretizing this system leads to the following dynamics [19]:

$$z_{k+1} = z_k - \frac{\Delta t}{Q} \cdot i_k \tag{2.14}$$

$$i_{R_1,k+1} = e^{\left(\frac{-\Delta t}{R_1 \cdot C_1}\right)} i_{R_1,k} + \left(1 - e^{\left(\frac{-\Delta t}{R_1 \cdot C_1}\right)}\right) i_k \tag{2.15}$$

$$v_k = \text{OCV}(z_k) - R_1 i_{R_1,k} - R_0 i_k \tag{2.16}$$

2.3.3 Other battery models

Advanced battery models have been developed to capture a more comprehensive range of behaviors within LIBs, including all polarization voltages and hysteresis effects. Examples include the n-RC model, which consists of multiple RC circuits, each representing different polarization phenomena, and the enhanced self-correcting model, which incorporates a nonlinear hysteresis component. While these models offer more detailed insights into battery dynamics, they also introduce greater complexity and substantially increase computational demands.

2.3.4 Model the battery aging

As the battery ages, the parameters in the models will change. Using model-based estimators without updating these parameters as the cell ages will result in increasingly poor estimation performance due to larger deviations in the model parameters.

From Section 2.2, some aging mechanisms are explained. From a battery model perspective, aging mechanisms are stated as slow changes in capacity and internal resistance. Compared to SOC, these parameters change very slowly. When applied to filtering methods, they are therefore assumed to stay constant but with added noise to account for their gradual changes over time.

Chapter 3

State Estimations

This chapter will go through basics of state estimations. First, the principle of sequential probabilistic inference and observability analysis. Thereafter, it presents a general Extended Kalman filter (EKF). Then, two more advanced versions of the EKF for parameter estimation are explained, before error calculations and the nonlinear least squares algorithm is mentioned.

3.1 Sequential probabilistic inference and the Kalman filter

Sequential probabilistic inference is used to find a state estimate that minimizes the error between the true and estimated state [20]. This concept involves calculating a new estimate at each timestep by using all previous estimations and new information (measurements). The estimate is based on process and sensor noise, making the solution probabilistic.

The Kalman Filter is, in short, the optimal minimum mean squared error state estimator (MMSE) for linear systems where all noises are Gaussian. However, since the Rint and RC1 models include a nonlinear measurement model, this linear filter cannot be applied directly.

The problem can be represented using two probability distributions: $p(x_k \mid x_{k-1})$, which represents the process model, and $p(z_k \mid x_k)$, known as the measurement model. Here, x_k represents the current state, and z_k represents the current measurement. Based on these distributions and an assessment of the uncertainties, a Bayesian problem is formed, which can be solved using a Kalman filter [21]. The properties of the Markov model must be maintained for this model to hold:

$$p(x_k \mid x_1, ..., x_{k-2}, x_{k-1}, z_1, ..., z_{k-2}, z_{k-1}) = p(x_k \mid x_{k-1}) \tag{3.1}$$

$$p(z_k \mid x_1, ..., x_{k-2}, x_{k-1}, x_k, z_1, ..., z_{k-2}, z_{k-1}) = p(z_k \mid x_k) \tag{3.2}$$

3.2 Observability analysis for state estimation

An essential aspect of being able to estimate the state and parameters of a system is that the system is observable.

For linear systems, where the state space system is defined as:

$$\dot{x} = Ax + Bu \tag{3.3}$$

$$y = Cx + Du \tag{3.4}$$

the observability matrix is given by:

$$\mathcal{O} = \begin{bmatrix} C & CA & CA^2 \ldots & CA^{n-1} \end{bmatrix}^T \tag{3.5}$$

A system is considered observable if the observability matrix $\mathcal{O}$ has full rank, meaning that the rank of $\mathcal{O}$ is equal to the number of states n in the system [22]. This ensures that it is possible to determine the state of the system from the output measurements.

In contrast to linear systems where observability is considered as a binary property, either observable or not, nonlinear systems may have many degrees of observability. This means that the strength of observability and whether the system is observable can vary significantly based on the state of the system. This is critical when analyzing a nonlinear system [23].

Observability analysis of a nonlinear system can be done in many ways. The simplest method is to linearize the system. The disadvantage of this method is that it often leads to incorrect results under different conditions or states the system might be in. The more precise method is based on using the Lie-derivatives.

Considering the nonlinear state dynamics and measurement functions of a system:
$f(x,u) = [f_1(x,u) \quad \ldots \quad f_n(x,u)]^T$ and $h(x,u) = [h_1(x,u) \quad \ldots \quad h_m(x,u)]^T$ then the Lie derivative is defind as follows [22]:

$$L_f h = \frac{\partial h}{\partial x} f = \sum_{i=1}^{n} \frac{\partial h}{\partial x_i} f_i \tag{3.6}$$

where the zeroth order Lie derivative is defined as h itself.

The observability matrix is then defined below in Equation 3.7 :

$$\mathcal{O}(x_k) = \frac{\partial l(x)}{\partial x} \qquad \text{where } l(x_k) = \begin{bmatrix} L_f^0 h_1(x_k) \\ \dots \\ L_f^0 h_m(x_k) \\ L_f^1 h_1(x_k) \\ \dots \\ L_f^{n-1} h_m(x_k) \end{bmatrix} \tag{3.7}$$

The theorem states the following: The system is locally observable at x_k if the matrix $\mathcal{O}(x_k)$ has n linearly independent rows, where n is the number of states in the system. This means that the matrix must have full row rank.

3.3 Extended Kalman Filter

The Extended Kalman Filter (EKF) is used to estimate the states of a nonlinear dynamical system. It starts with the general nonlinear dynamical system:

$$\dot{x} = f(x, u, w) \tag{3.8}$$
$$y = h(x, u, v) \tag{3.9}$$

where w and v are model and measurement noises, respectively. The EKF operates similarly to the Linear Kalman Filter but requires linearization at each timestep due to the nonlinear functions. Sequential probabilistic inference is valid for nonlinear systems if all the random variables are assumed to be Gaussian.

The algorithm used for the EKF, based on [24], [25], and [16], is outlined below:

Given the dicrete nonlinear model:

$$x_{k+1} = f(x_k, u_k, w_k) \qquad w_k \sim \mathcal{N}(0, \sigma_w^2) \tag{3.10}$$
$$y_k = h(x_k, u_k, v_k) \qquad v_k \sim \mathcal{N}(0, \sigma_V^2) \tag{3.11}$$

Defines first-order linearization:

$$\hat{\mathbf{A}}_k = \left.\frac{\partial f(\mathbf{x}_k, \mathbf{u}_k, \mathbf{w}_k)}{\partial \mathbf{x}_k}\right|_{\mathbf{x}_k=\hat{\mathbf{x}}_k} \qquad \hat{\mathbf{B}}_k = \left.\frac{\partial f(\mathbf{x}_k, \mathbf{u}_k, \mathbf{w}_k)}{\partial \mathbf{w}_k}\right|_{\mathbf{w}_k=\bar{\mathbf{w}}}$$
$$\hat{\mathbf{C}}_k = \left.\frac{\partial h(\mathbf{x}_k, \mathbf{u}_k, \mathbf{v}_k)}{\partial \mathbf{x}_k}\right|_{\mathbf{x}_k=\hat{\mathbf{x}}_k} \qquad \hat{\mathbf{D}}_k = \left.\frac{\partial h(\mathbf{x}_k, \mathbf{u}_k, \mathbf{v}_k)}{\partial \mathbf{v}_k}\right|_{\mathbf{v}_k=\bar{\mathbf{v}}}$$

Initialize the state estimate $\hat{x}_0^+$ and covariance $\Sigma_{x,0}^+$ for $k = 0$.

$$\hat{x}_0^+ = \mathbb{E}[x_0], \quad \Sigma_{x,0}^+ = \mathbb{E}[(x_0 - \hat{x}_0^+)(x_0 - \hat{x}_0^+)^T].$$

Computation and estimation for k > 0:

Prediction step:

$$\hat{x}_k^- = f(\hat{x}_{k-1}^+, u_{k-1}, \bar{w})$$
$$\Sigma_{x,k}^- = A_{k-1}\Sigma_{x,k-1}^+ A_{k-1}^T + B_{k-1}\Sigma_{\bar{w}} B_{k-1}^T$$

Update step:

$$\Sigma_{y,k} = C_k \Sigma_{x,k}^- (C_k)^T + D_k \Sigma_{\bar{v}} (D_k)^T$$
$$L_k = \Sigma_{x,k}^- (C_k)^T \Sigma_{y,k}^{-1}$$
$$\hat{x}_k^+ = \hat{x}_k^- + L_k\left[y_k - h(\hat{x}_k^-, u_k, \bar{v})\right]$$
$$\Sigma_{x,k}^+ = \Sigma_{x,k}^- - L_k \Sigma_{y,k} (L_k)^T$$

End Algorithm

3.4 Combined state and parameter estimation

The EKF is an efficient filter for predicting maximum-likelihood estimates of the states for nonlinear systems. It can also be used to estimate the parameters of a model. This strategy is named the *dual estimation* problem. This means that both the states and the parameters of a dynamical system are estimated, online and simultaneously [25]. The dual estimation problem is a method that switches between using the model to estimate the state and using the state to estimate the model.

A state space model can be expanded to include the slowly time-varying parameters in the

model, named θ. The new extended nonlinear state space system is then given:

$$x_{k+1} = f(x_k, \theta_k, u_k, w_k) \qquad w_k \sim \mathcal{N}(0, \sigma_w^2) \tag{3.12}$$

$$\theta_{k+1} = \theta_k + r_k \qquad r_k \sim \mathcal{N}(0, \sigma_r^2) \tag{3.13}$$

$$y_k = h(x_k, \theta_k, u_k, v_k) \qquad v_k \sim \mathcal{N}(0, \sigma_V^2) \tag{3.14}$$

In this model, the states are dependent on the varying parameters in the model, and the parameters itself is designed as constant, with added gaussian noise.

The online state and parameter estimation methods can be divided into two different approaches: Joint EKF and Dual EKF. The Joint EKF solves the state and parameter systems in parallel by augmenting a new state vector, $[x^T, \theta^T]^T$, and treating the problem as an expanded EKF. In contrast, the Dual EKF updates and solves the state and parameter vectors sequentially in two separate EKFs [26].

3.4.1 Joint Extended Kalman Filter

The Joint Extended Kalman Filter (JEKF) is an expanded version of the EKF. In addition to the normal states, it includes parameters in the state vector. This inclusion is feasible when the measurement model depends on both the state and the parameters. By augmenting the state vector to include these parameters, the JEKF can simultaneously estimate both the states and the parameters [27].

Figure 3.1 shows the flow of the EKF and JEKF.

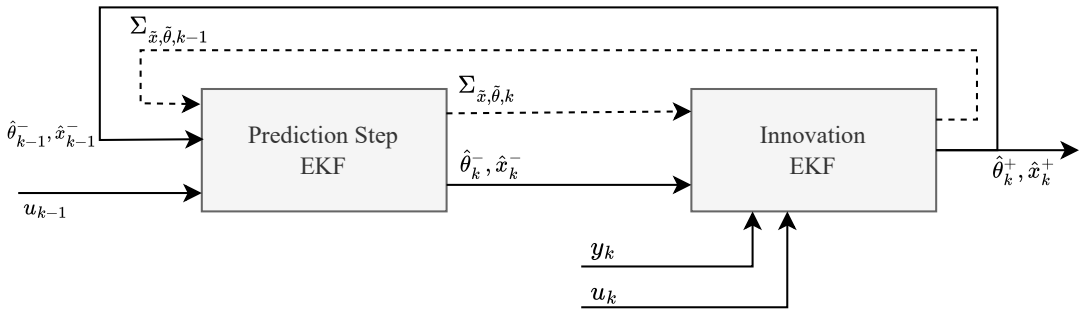

Figure 3.1: Schematic of the EKF and JEKF.

The augmented state space model for the JEKF can be formulated as follows [16]:

$$\begin{bmatrix} x_k \\ \theta_k \end{bmatrix} = \begin{bmatrix} f(x_{k-1}, u_{k-1}, w_{k-1}, \theta_{k-1}) \\ \theta_{k-1} + r_{k-1} \end{bmatrix} \tag{3.15}$$

$$y_k = h(x_k, u_k, v_k, \theta_k) \tag{3.16}$$

, where w_k, r_k and v_k are assumed independent Gaussian white noise, with covariance matrices defined as Σ_w, Σ_r and Σ_v. It can be expressed in a more comprehensive state space model, defining $\mathbf{X} = [\mathbf{x}, \theta]^T$ and $W = [\mathbf{w}, \mathbf{r}]^T$:

$$\mathbf{X}_k = F(\mathbf{X}_{k-1}, \mathbf{u}_{k-1}, \mathbf{W}_{k-1}), \qquad \mathbf{W}_k \sim \mathcal{N}(0, \Sigma_W) \tag{3.17}$$

$$\mathbf{y}_k = h(\mathbf{X}_k, \mathbf{u}_k, \mathbf{v}_k), \qquad \mathbf{v}_k \sim \mathcal{N}(0, \Sigma_v) \tag{3.18}$$

The definitions for the Jacobian matrices used in the JEKF are similar to the EKF. However, the inclusion of additional parameters in the state vector results in larger and more complex matrix calculations, increasing the computational load and computation time. Despite these differences, the algorithm used to run the JEKF follows the same steps as the EKF.

3.4.2 Dual Extended Kalman Filter

The Dual Extended Kalman Filter (DEKF) is a more advanced method compared to the JEKF, as it combines two EKFs. The calculations for the Jacobian matrices become tricky, requiring the use of the chain rule and recursive calculations. The first EKF is for state estimation, and the second EKF is for parameter estimation.

Since the DEKF splits the state and parameter vector, it loses some information that the JEKF stores in the covariance matrices. However, this approach simplifies the computation demands during each update step, even though it introduces additional complexity in the overall implementation and the recursive calculation of the Jacobian matrices.

The algorithm for the DEKF from [16] is given below.

Given the two discrete nonlinear models:

$$x_{k+1} = f(x_k, u_k, \theta_k, w_k) \qquad \theta_{k+1} = \theta_k + r_k,$$

$$y_k = h(x_k, u_k, \theta_k, v_k) \qquad d_k = g(x_k, u_k, \theta_k, e_k).$$

where w_k, v_k, r_k, and e_k are independent Gaussian noise processes with means $\bar{w}$, $\bar{v}$, zero, and $\bar{e}$ and covariance matrices $\Sigma_{\bar{w}}$, $\Sigma_{\bar{v}}$, Σ_r, and Σ_e, respectively.

Defines first order linearization: Defines first order linearization:

$$\hat{\mathbf{A}}_k = \left.\frac{\partial f(\mathbf{x}_k, \mathbf{u}_k, \hat{\boldsymbol{\theta}}_k^-, \mathbf{w}_k)}{\partial \mathbf{x}_k}\right|_{\mathbf{x}_k=\hat{\mathbf{x}}_k} \qquad \hat{\mathbf{B}}_k = \left.\frac{\partial f(\mathbf{x}_k, \mathbf{u}_k, \hat{\boldsymbol{\theta}}_k^-, \mathbf{w}_k)}{\partial \mathbf{w}_k}\right|_{\mathbf{w}_k=\bar{\mathbf{w}}}$$
$$\hat{\mathbf{C}}_k^{\mathbf{x}} = \left.\frac{\partial h(\mathbf{x}_k, \mathbf{u}_k, \hat{\boldsymbol{\theta}}_k^-, \mathbf{v}_k)}{\partial \mathbf{x}_k}\right|_{\mathbf{x}_k=\hat{\mathbf{x}}_k} \qquad \hat{\mathbf{D}}_k^{\mathbf{x}} = \left.\frac{\partial h(\mathbf{x}_k, \mathbf{u}_k, \hat{\boldsymbol{\theta}}_k^-, \mathbf{v}_k)}{\partial \mathbf{v}_k}\right|_{\mathbf{v}_k=\bar{\mathbf{v}}}$$
$$\hat{\mathbf{C}}_k^{\boldsymbol{\theta}} = \left.\frac{\partial g(\hat{\mathbf{x}}_k, \mathbf{u}_k, \boldsymbol{\theta}, \mathbf{e}_k)}{\partial \boldsymbol{\theta}}\right|_{\boldsymbol{\theta}=\boldsymbol{\theta}_k} \qquad \hat{\mathbf{D}}_k^{\boldsymbol{\theta}} = \left.\frac{\partial g(\hat{\mathbf{x}}_k, \mathbf{u}_k, \boldsymbol{\theta}, \mathbf{e}_k)}{\partial \mathbf{e}_k}\right|_{\mathbf{e}_k=\bar{\mathbf{e}}}.$$

Initialize the state and parameter estimate and covariance for $k = 0$, including the recursive variables β and $\hat{\mathbf{C}}_0^{\boldsymbol{\theta}}$.

$$\hat{\theta}_0^+ = \mathbb{E}[\theta_0], \qquad \Sigma_{\theta,0}^+ = \mathbb{E}[(\theta_0 - \hat{\theta}_0^+)(\theta_0 - \hat{\theta}_0^+)^T],$$
$$\hat{x}_0^+ = \mathbb{E}[x_0], \qquad \Sigma_{x,0}^+ = \mathbb{E}[(x_0 - \hat{x}_0^+)(x_0 - \hat{x}_0^+)^T]$$
$$\beta_0 = 0 \qquad \hat{\mathbf{C}}_0^{\boldsymbol{\theta}} = 0$$

Computation and estimation for k > 0:

Parameter prediction:

$$\hat{\theta}_k^- = \hat{\theta}_{k-1}^+$$
$$\Sigma_{\theta,k}^- = \Sigma_{\theta,k-1}^+ + \Sigma_r$$

State prediction:

$$\hat{x}_k^- = f(\hat{x}_{k-1}^+, u_{k-1}, \hat{\theta}_k^-, \bar{w})$$
$$\Sigma_{x,k}^- = A_{k-1}\Sigma_{x,k-1}^+ A_{k-1}^T + B_{k-1}\Sigma_{\bar{w}} B_{k-1}^T$$

State update:

$$\Sigma_{y,k} = C_k^x \Sigma_{x,k}^- (C_k^x)^T + D_k^x \Sigma_{\bar{v}} (D_k^x)^T$$
$$L_k^x = \Sigma_{x,k}^- (C_k^x)^T \Sigma_{y,k}^{-1}$$
$$\hat{x}_k^+ = \hat{x}_k^- + L_k^x \left[y_k - h(\hat{x}_k^-, u_k, \hat{\theta}_k^-, \bar{v}) \right]$$
$$\Sigma_{x,k}^+ = \Sigma_{x,k}^- - L_k^x \Sigma_{y,k} (L_k^x)^T$$

Parameter update:

$$\begin{aligned}
\Sigma_{d,k} &= C_k^\theta \Sigma_{\theta,k}^- (C_k^\theta)^T + D_k^\theta \Sigma_e (D_k^\theta)^T \\
L_k^\theta &= \Sigma_{\theta,k}^- (C_k^\theta)^T \Sigma_{d,k}^{-1} \\
\hat{\theta}_k^+ &= \hat{\theta}_k^- + L_k^\theta \left[y_k - g(\hat{x}_k^-, u_k, \hat{\theta}_k^-, e) \right] \\
\Sigma_{\theta,k}^+ &= \Sigma_{\theta,k}^- - L_k^\theta \Sigma_{d,k} (L_k^\theta)^T
\end{aligned}$$

End Algorithm

The tricky part of this algorithm, in comparison to the JEKF, is the computation of $\hat{\mathbf{C}}_k^{\boldsymbol{\theta}}$, done in the parameter update step. This involves defining the Jacobian matrix $\hat{\mathbf{C}}_k^{\boldsymbol{\theta}}$ and computing it using a recursive calculation, as outlined below [28].

$$\hat{\mathbf{C}}_k^{\boldsymbol{\theta}} = \left. \frac{\partial g(\hat{\mathbf{x}}_k, \mathbf{u}_k, \mathbf{e}_k)}{\partial \boldsymbol{\theta}} \right|_{\boldsymbol{\theta}=\boldsymbol{\theta}_k} \tag{3.19}$$

$$\frac{\partial g(\hat{\mathbf{x}}_k, \mathbf{u}_k, \mathbf{e}_k)}{\partial \boldsymbol{\theta}} = \frac{\partial g(\hat{\mathbf{x}}_k, \mathbf{u}_k, \boldsymbol{\theta})}{\partial \boldsymbol{\theta}} + \frac{\partial g(\hat{\mathbf{x}}_k, \mathbf{u}_k, \boldsymbol{\theta})}{\partial \hat{\mathbf{x}}_k} \frac{d\hat{\mathbf{x}}_k^-}{d\boldsymbol{\theta}} \tag{3.20}$$

Here, $\frac{d\hat{\mathbf{x}}_k^-}{d\boldsymbol{\theta}}$ is defined as $\boldsymbol{\beta}_k$, which needs to be computed recursively.

$$\boldsymbol{\beta}_k = \frac{\partial f(\hat{\mathbf{x}}_{k-1}^+, \mathbf{u}_{k-1}, \boldsymbol{\theta})}{\partial \boldsymbol{\theta}} + \frac{\partial f(\hat{\mathbf{x}}_{k-1}^+, \mathbf{u}_{k-1}, \boldsymbol{\theta})}{\partial \hat{\mathbf{x}}_{k-1}^+} \frac{d\hat{\mathbf{x}}_{k-1}^+}{d\boldsymbol{\theta}} \tag{3.21}$$

$$\frac{d\hat{\mathbf{x}}_{k-1}^+}{d\boldsymbol{\theta}} = \boldsymbol{\beta}_{k-1} - \mathbf{L}_{k-1}^x \hat{\mathbf{C}}_{k-1}^x \tag{3.22}$$

From Equations 3.21 and 3.22, it is evident that the computation of $\boldsymbol{\beta}_k$ requires a recursive update, where each step depends on the previous state and measurement update. The schematic of theDEKF is shown in Figure 3.2, illustrating the dual estimation process for states and parameters.

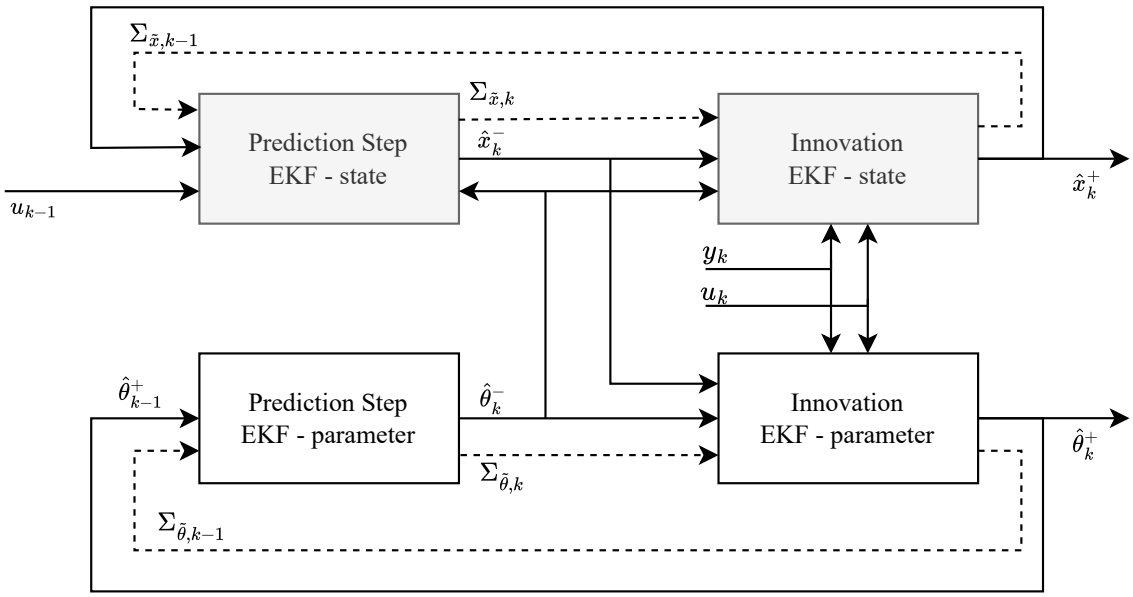

Figure 3.2: Schematic of the Dual Extended Kalman filter.

3.5 Root mean square and mean absolute error

Two widely used metrics for error evaluation are the Root Mean Square Error (RMSE) and Mean Absolute Error (MAE). For a number of n measurements y, and a number of n estimates $\hat{y}$, this metrics is given as:

$$\text{RMSE} = \sqrt{\frac{1}{n}\sum_{i=1}^{n}(\hat{y}_i - y_i)^2} \tag{3.23}$$

$$\text{MAE} = \frac{1}{n}\sum_{i=1}^{n}|\hat{y}_i - y_i| \tag{3.24}$$

The RMSE calculates the square root of the average of the squared differences between estimated values and true values. This means RMSE gives more weight to larger errors than smaller ones. The MAE measures the average magnitude of the errors between estimates and true values, simply averaging the absolute errors.

The difference in their applications is that RMSE is particularly useful when large deviations are undesirable. RMSE will never be lower than MAE, but they will be equal if all errors are the same. Comparing RMSE with MAE is helpful for assessing the variance in errors. If RMSE and MAE are significantly different, it indicates a lot about the variance of the errors [29].

3.6 Nonlinear least squares estimation

Non-linear least squares estimation is a method for parameter estimation in statistical models characterized by nonlinear relationships between dependent and independent variables. This technique is used to identify parameter values that optimally describe data through a predetermined model structure, for instance, a given battery model [30].

The general principle of nonlinear least squares estimation involves minimizing the sum of the squared deviations between observed values and the predicted values by the model. For a dataset containing n points, where y_i are the observed values and $f(x_i, \theta)$ is the model function dependent on parameters θ, the objective is to solve the following optimization problem:

$$S(\theta) = \sum_{i=1}^{n} [y_i - f(x_i, \theta)]^2$$

where $S(\theta)$ represents the total sum of squared residuals to be minimized in an objective function. Different solvers, such as the Gauss-Newton are commonly used.

Chapter 4

Method

In this chapter, the methodology used for the implementation of the filters is summarized. The first part, Section 4.1, presents the implementation of the various filters. Following this, Section 4.2 summarizes an observability analysis of the system. Then, in Section 4.3, the battery dataset is presented and assumptions are explained. Finally, Section 4.4 describes the simulation setup.

4.1 State and parameter estimation implementation

In this project, seven variations of Kalman filters have been implemented. These include two versions of the EKF, three versions of the JEKF, and two versions of the DEKF. To clearly distinguish among these in the results and discussions, the filters are named as follows: EKF-R, EKF-RC1, JEKF-R, JEKF-RC1, JEKF-RC1-Ext (extended), DEKF-R, and DEKF-RC1. The designations 'R' and 'RC1' indicate the battery model employed in each filter (Section 2.3).

EKF-R and EKF-RC1 maintain a constant battery model throughout the estimations. All variations of JEKF and DEKF include the parameter estimation of capacity (Q) and internal resistance (R_0). In addition, JEKF-RC1-Ext, which is based on the RC1/Thevenin battery model, also estimates R_1 and C_1. In contrast, JEKF-RC1 and DEKF-RC1 have constant parameters for R_1 and C_1, set to the initially identified values.

These filters, along with their respective algorithms explained in Chapter 3, have been implemented as functions in MATLAB. Note that SOC is mentioned as z in this chapter.

4.1.1 Extended Kalman Filter

The implementation of EKF-R and EKF-RC1 is straightforward. Using the discretized battery models (Rint and RC1 from Section 2.3), the state-space model is defined as follows. Since the states in EKF-R are explicitly mentioned in EKF-RC1, only the model for EKF-RC1 is shown here.

$$x_{k+1} = f(x_k, u_k, w_k) = \begin{bmatrix} z_{k+1} \\ i_{R_1,k+1} \end{bmatrix} = \begin{bmatrix} z_k - \frac{\Delta t}{Q}(i_k + w_k) \\ e^{-\frac{\Delta t}{R_1 C_1}} i_{R_1,k} + \left(1 - e^{-\frac{\Delta t}{R_1 C_1}}\right)(i_k + w_k) \end{bmatrix} \tag{4.1}$$

$$y_k = h(x_k, u_k, v_k) = \text{OCV}(z_k) - R_0 i_k - R_1 i_{R_1,k} + v_k \tag{4.2}$$

From the model above the noises (v_k and w_k) can strongly be related to the current and voltage-sensor noise. The estimator for this system is implemented using the EKF algorithm from Section 3.3, which is based on [16] and [31]. The linearization step needed for this algorithm to work is as follows:

$$\hat{A}_k = \left.\frac{\partial f(x_k, u_k, w_k)}{\partial x_k}\right|_{x_k = \hat{x}_k^+} = \begin{bmatrix} 1 & 0 \\ 0 & e^{-\frac{\Delta t}{R_1 C_1}} \end{bmatrix} \tag{4.3}$$

$$\hat{B}_k = \left.\frac{\partial f(x_k, u_k, w_k)}{\partial w_k}\right|_{w_k = \bar{w}} = \begin{bmatrix} -\frac{\Delta t}{Q} \\ 1 - e^{-\frac{\Delta t}{R_1 C_1}} \end{bmatrix} \tag{4.4}$$

$$\hat{C}_k = \left.\frac{\partial h(x_k, u_k, v_k)}{\partial x_k}\right|_{x_k = \hat{x}_k^-} = \begin{bmatrix} \frac{\partial \text{OCV}(z_k)}{\partial z_k} & -R_1 \end{bmatrix} \tag{4.5}$$

$$\hat{D}_k = \left.\frac{\partial h(x_k, u_k, v_k)}{\partial v_k}\right|_{v_k = \bar{v}} = 1 \tag{4.6}$$

The tuning parameter used in this filter is summarized in Section 4.1.4.

4.1.2 Joint Extended Kalman Filter

The JEKF is implemented in three versions. This is done to be able compare the performance and accuracy as the complexity and number of states increase. The first filter JEKF-R is based on the Rint model, adding estimation of two parameters: internal resistance and capacity. The second filter, JEKF-RC1 uses the RC1 model as its basis and estimates the same parameters as the JEKF-R. Additionally, a third and most advanced filter JEKF-RC1-Ext is implemented, still using the RC1 model. This model adds two new parameters in the state vector, namely R_1 and C_1, from the RC1 circuit (Figure 2.4).

Since the states of the JEKF-R and JEKF-RC1 include all the states used in the JEKF-RC1-Ext, the matrices for the JEKF-RC1-Ext are shown below. The implementation details of JEKF-R and JEKF-RC1 are explicitly defined in the following matrices and will therefore not be mentioned further.

For the implemented JEKF-RC1-Ext, the state vector X is defined as

$$X_k = \begin{bmatrix} z_k & i_{R_1,k} & R_{0,k} & Q_k & R_{1,k} & C_{1,k} \end{bmatrix}^T$$

and the noise vector is defined as

$$W_k = \begin{bmatrix} w_k^i & w_k^{R_0} & w_k^Q & w_k^{R_1} & w_k^{C_1} \end{bmatrix}^T.$$

The resulting discrete state space system is then defined as:

$$X_{k+1} = F(X_k, u_k, W_k) = \begin{bmatrix} z_k - \frac{\Delta t}{Q_k}(i_k + w_k^i) \\ e^{-\frac{\Delta t}{(R_1 C_1)_k}} i_{R_1,k} + \left(1 - e^{-\frac{\Delta t}{(R_1 C_1)_k}}\right)(i_k + w_k^i) \\ R_{0,k} + w_k^{R_0} \\ Q_k + w_k^Q \\ R_{1,k} + w_k^{R_1} \\ C_{1,k} + w_k^{C_1} \end{bmatrix} \tag{4.7}$$

$$y_k = h(X_k, u_k, v_k) = OCV(z_k) - R_{0,k} i_k - R_{1,k} i_{R_1,k} + v_k \tag{4.8}$$

The linearization step done in the JEKF following the EKF algorithm is done as follows:

$$\hat{A}_k = \left.\frac{\partial F}{\partial X}\right|_{x_k=\hat{x}_k^+} = \begin{bmatrix} 1 & 0 & 0 & \frac{\Delta t}{Q^2 i_k} & 0 & 0 \\ 0 & e^{-\frac{\Delta t}{R_1 C_1}} & 0 & 0 & \frac{\Delta t i_{R_1} e^{-\frac{\Delta t}{C_1 R_1}} - \Delta t i e^{-\frac{\Delta t}{C_1 R_1}}}{C_1 R_1^2} & \frac{\Delta t i_{R_1} e^{-\frac{\Delta t}{C_1 R_1}} - \Delta t i e^{-\frac{\Delta t}{C_1 R_1}}}{C_1^2 R_1} \\ 0 & 0 & 1 & 0 & 0 & 0 \\ 0 & 0 & 0 & 1 & 0 & 0 \\ 0 & 0 & 0 & 0 & 1 & 0 \\ 0 & 0 & 0 & 0 & 0 & 1 \end{bmatrix} \tag{4.9}$$

$$\hat{B}_k = \left.\frac{\partial F}{\partial W}\right|_{w_k=\bar{w}_k} = \begin{bmatrix} -\frac{\Delta t}{Q} & 0 & 0 & 0 & 0 \\ 1 - e^{-\frac{\Delta t}{R_1 C_1}} & 0 & 0 & 0 & 0 \\ 0 & 1 & 0 & 0 & 0 \\ 0 & 0 & 1 & 0 & 0 \\ 0 & 0 & 0 & 1 & 0 \\ 0 & 0 & 0 & 0 & 1 \end{bmatrix} \tag{4.10}$$

$$\hat{C}_k = \left.\frac{\partial h}{\partial X}\right|_{x_k=\hat{x}_k^-} = \begin{bmatrix} \frac{\partial \mathrm{OCV}(z_k)}{\partial z_k} & -R_{0,k} & -i_k & 0 & -i_{R_1,k} & 0 \end{bmatrix} \tag{4.11}$$

$$\hat{D}_k = \left.\frac{\partial h}{\partial v_k}\right|_{v_k=\bar{v}_k} = 1 \tag{4.12}$$

4.1.3 Dual Extended Kalman Filter

The DEKF is implemented in two versions, one with the Rint model as a basis, and the other one with the RC1 model. Since the DEKF-RC1 contains all the states used in the DEKF-R, the matrices for the DEKF-RC1 are shown below. The implementation details of DEKF-R are explicitly defined in the following matrices and will therefore not be mentioned further.

State filter:

$$x_k = \begin{bmatrix} z_k \\ i_{R_1} \end{bmatrix} = \begin{bmatrix} z_{k-1} - \frac{\Delta t}{Q}(i_{k-1} + w_k^i) \\ \exp\left(\frac{-\Delta t}{R_1 C_1}\right) i_{R_1,k-1} + \left(1 - \exp\left(\frac{-\Delta t}{R_1 C_1}\right)\right)(i_{k-1} + w_k^i) \end{bmatrix} \tag{4.13}$$

$$y_k = OCV(z_k) - R_0 i_k + v_k^x \tag{4.14}$$

Parameter filter:

$$\theta_k = \begin{bmatrix} R_{0,k} \\ Q_k \end{bmatrix} = \begin{bmatrix} R_{0,k-1} \\ Q_{k-1} \end{bmatrix} + W_k^\theta \tag{4.15}$$

$$y_k = OCV(z_k) - R_0 i_k + v_k^\theta \tag{4.16}$$

Linearization of the systems:

$$\hat{A}_k = \left.\frac{\partial f}{\partial x_k}\right|_{x_k = \hat{x}_k^+} = \begin{bmatrix} 1 & 0 \\ 0 & e^{-\frac{\Delta t}{R_1 C_1}} \end{bmatrix} \qquad \hat{B}_k = \left.\frac{\partial f}{\partial w_k}\right|_{w_k = \bar{w}_k} = \begin{bmatrix} -\frac{\partial t}{Q} \\ 1 - e^{-\frac{\Delta t}{R_1 C_1}} \end{bmatrix} \tag{4.17}$$

$$\hat{C}_k^x = \left.\frac{\partial h}{\partial x_k}\right|_{x_k = \hat{x}_k^-} = \begin{bmatrix} \frac{\partial \mathrm{OCV}(z_k)}{\partial z_k} & -R_1 \end{bmatrix} \qquad \hat{D}_k^x = \left.\frac{\partial h}{\partial v_k^x}\right|_{v_k^x = \bar{v}_k^x} = 1 \tag{4.18}$$

$$\hat{C}_k^\theta = \left.\frac{\partial h}{\partial \theta}\right|_{\theta_k = \hat{\theta}_k^-} = \begin{bmatrix} -i & 0 \end{bmatrix} + \begin{bmatrix} \frac{\partial \mathrm{OCV}(z_k)}{\partial z_k} & -R_1 \end{bmatrix} \beta_k \qquad \hat{D}_k^\theta = \left.\frac{\partial f}{\partial v_k^\theta}\right|_{v_k^\theta = \bar{v}_k^\theta} = 1 \tag{4.19}$$

where β_k is computed recurcively as (Section 3.4.2 for detailed explanation).:

$$\beta_k = \begin{bmatrix} 0 & \frac{\Delta t}{Q^2} i \\ 0 & 0 \end{bmatrix} + \begin{bmatrix} 1 & 0 \\ 0 & e^{-\frac{\Delta t}{R_1 C_1}} \end{bmatrix} \cdot (\beta_{k-1} - L_{k-1}^x \cdot \hat{C}_{k-1}^\theta) \tag{4.20}$$

The DEKF algorithm is then implemented as shown in Section 3.4.2.

4.1.4 Tuning parameters

The final tuning parameters, including the initial state, initial state covariances, and noise covariances, are set equal across all filters, except for the measurement noise $\Sigma_{V,\text{EKF}}$, which is set lower for EKF-R and EKF-RC1 to ensure greater robustness against capacity changes.

The initial state values and their covariances are initialized as follows:

State	Initial Value $[x_0]$	Variance $[\Sigma_{x_0}]$
z	0.6	0.1^2
i_{R_1}	0 A	0.01^2
R_0	$86m\Omega$	$(0.015 \cdot 86\ \text{m}\Omega)^2$
Q	2.1 Ah	$(0.015 \cdot 2.1\ \text{Ah})^2$
R_1	$56m\Omega$	$(0.015 \cdot 56\ \text{m}\Omega)^2$
C_1	500 F	$(0.2 \cdot 500\ \text{F})^2$

Table 4.1: Initial tuning state and covariances.

Define τ as the number of seconds in a month:

$$\tau = 3600 \times 24 \times 30$$

Then tuned the **process noise** parameters as follows:

Parameter	Variance [Noise]	Description
$\Sigma_{w_k^i}$	0.1^2	Noise for current sensor.
$\Sigma_{w_k^{R_0}}$	$\left(\frac{50R_{0,k=0}}{\tau}\right)^2$	Noise R_0
$\Sigma_{w_k^Q}$	$\left(\frac{50Q_{k=0}}{\tau}\right)^2$	Noise Capacity
$\Sigma_{w_k^{R_1}}$	$\left(\frac{50R_{1,k=0}}{\tau}\right)^2$	Noise R_1
$\Sigma_{w_k^{C_1}}$	$\left(\frac{50C_{1,k=0}}{\tau}\right)^2$	Noise C_1

Table 4.2: Tuned process noise parameters.

The **measurement noise** covariance matrix Σ_ν is tuned differently for the EKF compared to the JEKF and the DEKF:

Filter	Variance [Noise]	Description
$\Sigma_{\nu,\text{JEKF and DEKF}}$	0.1^2	Measurement noise for JEKF and DEKF
$\Sigma_{\nu,\text{EKF}}$	0.05^2	Measurement noise for EKF

Table 4.3: Tuned measurement noise parameters.

The difference in this tuning is due to the fact that, since the EKF does not account for parameter changes, it is more vulnerable to inaccuracies. By decreasing Σ_ν, the confidence in the voltage measurement (and the OCV(SOC) function) is increased. This adjustment allows the EKF to converge more quickly to the correct SOC by relying more heavily on the voltage measurement.

4.2 Observability analysis for the JEKF-RC1

An observability analysis has been conducted for the system using the JEKF-RC1 model. Below, the dynamic state space system is presented, followed by the computation of the observability matrix using the Lie derivative method explained in Section 4.2.

$$\dot{X} = F(X,u) = \begin{bmatrix} \dot{z} \\ \dot{i}_{R_1} \\ \dot{R}_0 \\ \dot{Q} \end{bmatrix} = \begin{bmatrix} -\frac{i}{Q} \\ -\frac{1}{R_1C_1} i_{R_1} + \frac{1}{R_1C_1} i \\ 0 \\ 0 \end{bmatrix} \tag{4.21}$$

$$y = h(X,u) = \text{OCV}(z) - R_0 i - R_1 i_{R_1} \tag{4.22}$$

Computing the first four Lie derivatives as described in Section 3.2, the observability matrix is constructed as follows:

$$\mathcal{O}(x) = \begin{bmatrix} \frac{dOCV(z)}{dz} & -R_1 & -i & 0 \\ -\frac{i}{Q}\frac{d^2OCV(z)}{dz^2} & \frac{R_1}{(R_1C_1)} & 0 & \frac{i}{(-Q)^2}\frac{dOCV(z)}{dz} \\ (-\frac{i}{Q})^2\frac{d^3OCV(z)}{dz^3} & -\frac{R_1}{(R_1C_1)^2} & 0 & \frac{2\cdot i^2}{(-Q)^3}\frac{d^2OCV(z)}{dz^2} \\ (-\frac{i}{Q})^3\frac{d^4OCV(z)}{dz^4} & \frac{R_1}{(R_1C_1)^3} & 0 & \frac{3\cdot i^3}{(-Q)^4}\frac{d^3OCV(z)}{dz^3} \end{bmatrix} \tag{4.23}$$

By mathematical induction, the k-th Lie derivative can be generalized as follows:

$$\nabla L_f^k h = \begin{bmatrix} \left(-\frac{i}{Q}\right)^k \frac{d^{k+1}\text{OCV}(z)}{dz^{k+1}} & \frac{R_1}{(R_1C_1)^k}(-1)^{k+1} & \begin{cases} -i & \text{if } k=0 \\ 0 & \text{otherwise} \end{cases} & \frac{ki^k}{(-Q)^{k+1}}\frac{d^k\text{OCV}(z)}{dz^k} \end{bmatrix} \tag{4.24}$$

By the analysis done above, it can be concluded that the system is observable ($\mathcal{O}$ full rank) when there exists at least **two** integers $k \in \mathbb{Z}^+$ such that:

$$\frac{d^k\text{OCV}}{dz^k} \neq 0 \quad \text{and} \quad i \neq 0 \tag{4.25}$$

This means that if the battery being estimated has the current $i = 0$, the observability matrix does not have full rank. This makes sense, since from the measurement function it can be seen that there is no way to estimate the internal resistance if the current is zero. An interesting note to this conclusion of the observability analysis is that the observability relies on the nonlinearity of the OCV(z) function [32].

4.3 Preparation of battery dataset

The dataset used in this thesis is from the *Prognostics Data Repository* at NASA, furthermore *dataset 11*: "Randomized Battery Usage" [33] [34]. This dataset consists of 7 different tests, where each test is performed on four Lithium Cobalt-Oxide (LCO) cells, resulting in a total of 28 cells. This cell has the lower cut-off voltage set to $3.2V$ and the upper cut-off voltage set to $4.2V$, and the nominal capacity at 2.1 Ah. Table 4.4 shows the different test performed by NASA.

Test Number	Cells Nr	Description
1	9, 10, 11, 12	Charge Discharge Room Temperature
2	3, 4, 5, 6	Uniform Distributed Discharge
3	1, 2, 7, 8	Room Temperature Variable Recharging Periods
4	25, 26, 27, 28	Skewed High 40 °C
5	17, 18, 19, 20	Skewed High Room Temperatur
6	21, 22, 23, 24	Skewed Low 40 °C
7	13, 14, 15, 16	Skewed Low Room Temperature

Table 4.4: Summary of the seven battery test procedures from NASA Randomized Battery Usage [34].

In the simulations conducted in this thesis, it is chosen to use data from test numbers 4 to 7 (Table 4.4) from *NASA Randomized Battery Usage* [34]. These tests involve continuous charge and discharge cycles with variable discharge currents, ranging from 0.5A to 5A. The discharge process is referred to as a "random walk." A predetermined probability distribution of discharge currents is selected for each minute. The distinction between 'Skewed High' and 'Skewed Low' lies in the likelihood of discharging at high currents. 'Skewed High' tests have a higher probability of discharging at higher currents, leading to a quicker discharge of the battery, whereas 'Skewed Low' tests are more likely to discharge at lower currents. Once the cells reach the lower cutoff voltage, they are charged at a constant current of 2A until reaching the upper cutoff voltage, at which point the charging switches to constant voltage until the current falls below the threshold of 20mA. This charging type is known as the CC-CV charging method.

These tests are conducted at different ambient temperatures, including room temperature and 40 °C, resulting in four datasets labeled as *Skewed High* and *Skewed Low*, each with two temperature variations.

4.3.1 Modification to dataset

The dataset primarily contains measurements of voltage, current, and temperature. However, during certain cycles, there have been charging sessions that were not recorded. This can lead to instabilities in the estimator, causing incorrect estimations. In this test, no provisions were made to account for such circumstances. In real scenarios, a straightforward solution could be to restart the estimator if such errors are detected. Areas from the data where this occurs have been removed, and the battery data has been spliced together when the cell is fully charged. This ensures a continuous data stream from start to finish, which makes physical sense for a battery cell. Additionally, the data has been interpolated to a time step of `dt = 1s` to make the simulations more consistent.

4.3.2 Battery reference capacity

A reference capacity check is performed on the cells periodically, after every 50 random walk discharge cycles. This means that the batteries have been discharged 50 times between each capacity check. The results from this test provide a benchmark for the nominal capacity of the batteries and can be compared with the estimates from the filters.

In this capacity check, batteries are first charged to a voltage of 4.2V. Following this, they are discharged at a rate of 1A until the voltage falls to the lower threshold of 3.2V. After discharging, the batteries are recharged at a constant current of 2A. When the voltage reaches 4.2V, the charging method switches to constant voltage mode, which continues until the charging current drops below 0.01A.

Figure 4.1 and 4.2 shows the available reference capacity checks from all 28 cells in dataset [34].

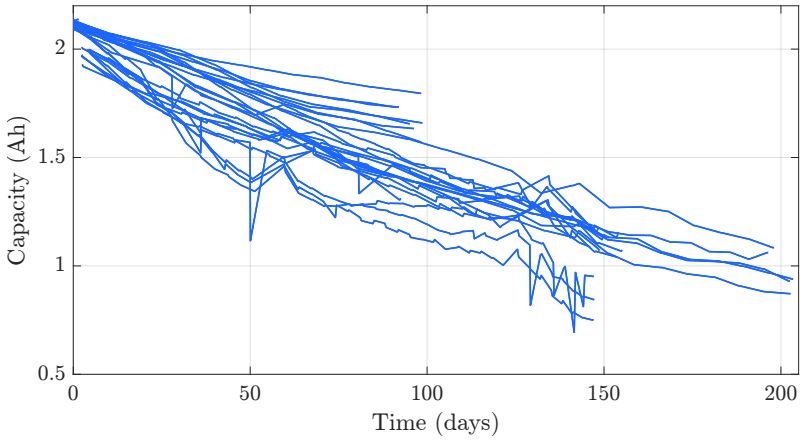

Figure 4.1: Reference capacity test for all 28 cells in dataset [34].

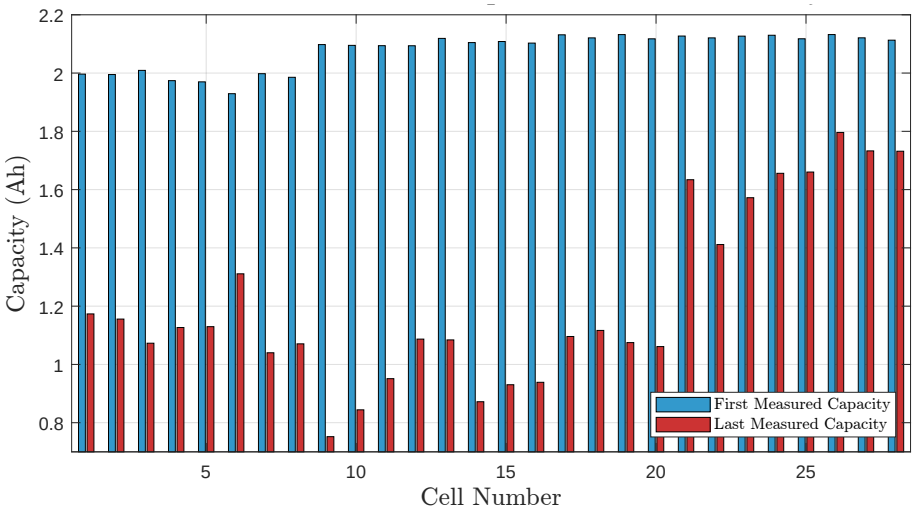

Figure 4.2: Bar plot showing first and last measured capacity for all the 28 cells.

4.3.3 OCV - SOC curve

The data also contains a slow discharge-charge test, and it is reasonable to use this test to approximate the OCV - SOC relationship for the LCO cell. In this test, the current was set to 0.04A, which refers to the current rate of $\approx C/53$. Figure 4.3 shows the measured voltage during this test.

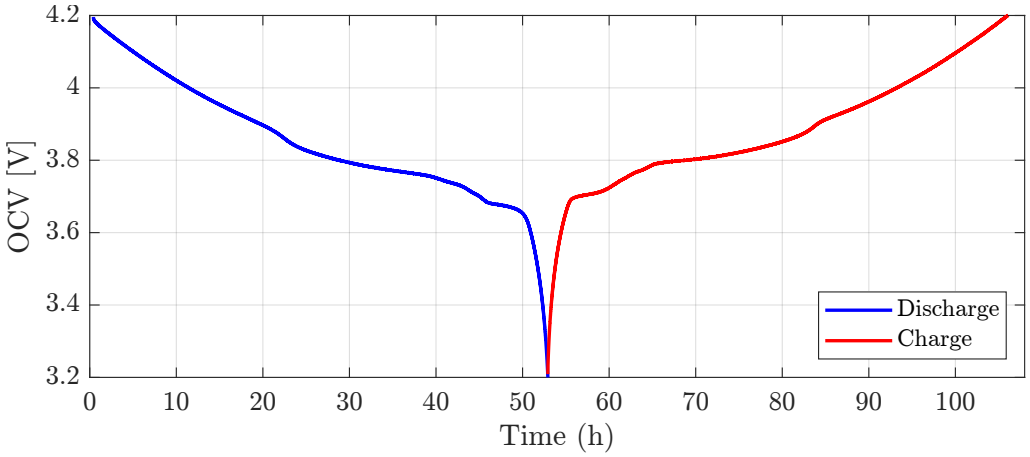

Figure 4.3: Measured voltage during slow discharge - charge test.

It should be noted that since there is a current flowing through the cell, there may be some ohmic polarization and hysteresis present in the cell. Especially the hysteresis causes the charge and discharge curves to be slightly different. Therefore, an average of these two curves (see Figure 4.4) is calculated to get the closest approximation of the relationship.

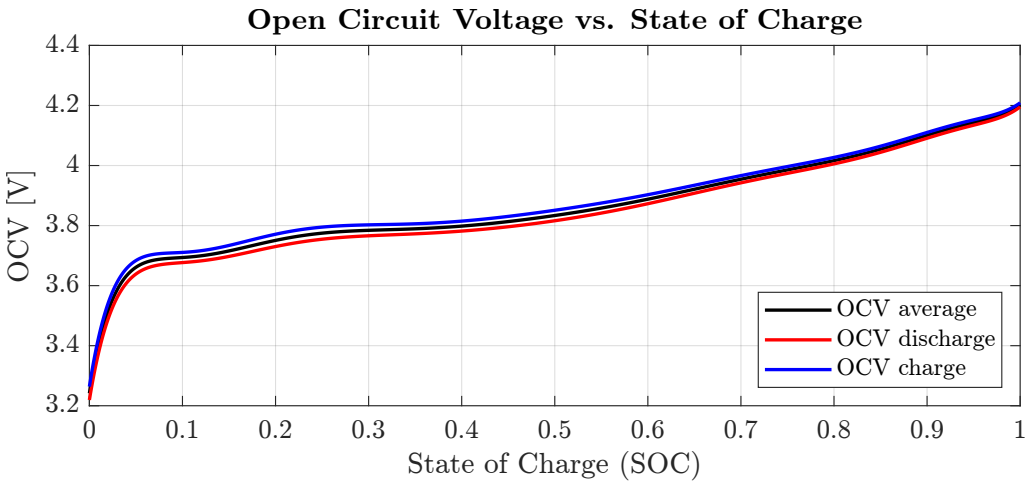

Figure 4.4: Low current approximation OCV curve of the cell.

4.3.4 Parameter identification

The inital battery parameters used in this thesis are identified using the least squares approach described in Section 3.6. This approach allows us to estimate the best-fitting parameters from the dataset and is advantageous because it enables the use of data from any point in the dataset where the capacity and initial SOC is known. The method utilized in MATLAB in its integrated `nlinfit` function is the *Levenberg–Marquardt* nonlinear least squares algorithm, which combines the concepts of gradient descent and Gauss-Newton [35].

Although a pulsed discharge response can be used to estimate the internal resistance and the parameters for the RC circuit in the RC1 model, this specific test is not available for all the data in the dataset. The following figure show a pulsed discharge test from an LCO cell, which could be used to initialize the parameters:

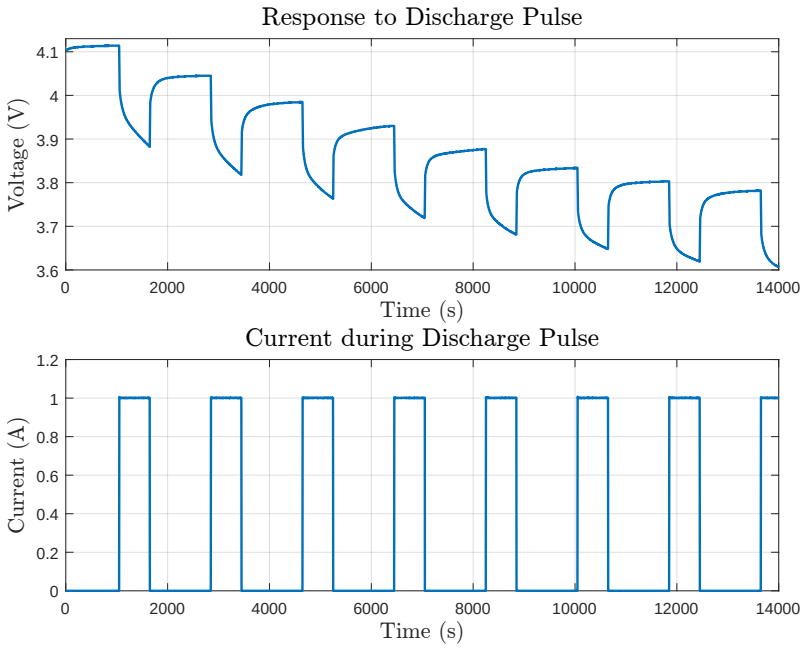

Figure 4.5: Pulsed discharge test.

From this data, the RC1 parameters could be stated using the rough parameter approach described by Plett [12]. This approach consists of the following steps:

$$R_0 = \frac{\Delta V_0}{\Delta i}, \quad R_1 = \frac{\Delta V_\infty}{\Delta i} - R_0, \quad C_1 = \frac{\Delta t_{stable}}{4R_1} \tag{4.26}$$

From using Equation 4.26 and Figure 4.5 the parameters can be estimated:

$$R_0 = 95m\Omega, \quad R_1 = 50m\Omega, \quad C_1 = 1800F$$

However, since the pulsed discharge test is not available for all data, the least squares algorithm is employed to regularly determine initial values for the dataset. This allows for continuous parameter estimation, providing comparisons with the estimates generated by the filters.

4.4 Test cases

The simulations of the test cases were conducted using MATLAB R2022b on a stationary Windows PC provided by NTNU, equipped with an i7-10700 CPU @ 2.90GHz processor and 32GB of RAM. Since a total of 7 individual filters are tested, the *Parallel Computing Toolbox* in Matlab is utilized to efficiently run all the filters simultaneously.

4.4.1 Ground truth

To quantify the accuracy and compare estimators to each other, the ground truth for the SOC has been determined using the Coulomb counting method from the current measurement. Since the accuracy of the Coulomb counting method and the SOC relies on precise current measurements and the correct battery capacity, the true SOC incorporates results from "reference capacity" tests conducted on the cell. Additionally, the SOC is maintained within the range of 0 to 100%. It should be noted that potential biases from the current sensor have not been addressed in this analysis. However, a reset to 100% SOC is systematically applied after each complete recharge to ensure consistency.

The ground truth for the battery capacity is established based on the reference capacity checks performed on the battery (Section 4.3.2). Linear interpolations between these tests are done, assuming that the cell degrades linearly over time in between.In addition, the least squares algorithm is periodically used to estimate parameters, which can be compared to the parameter estimations made by the filters. This applies to the parameters R_0, R_1, and C_1.

The estimations are then compared to the ground truth using the estimator performance metric RMSE and MAE (section 3.5).

4.4.2 Test case 1 - EKF versus Joint and Dual EKF

This test case utilizes the data for cell 21. In this data, the LCO cell is operated with skewed high currents under an ambient temperature of $40°C$ (Table 4.4). From this data, two sections from the dataset of around 200 hours each have been selected. The first part is from the initial 200 operational hours, and the second part is from the hours around 2000+. This test is designed to compare the performance of EKF with the Joint and Dual EKF. It is especially interesting to compare a new battery with accurate model parameters against an old battery with outdated initial parameters.

The next figures show excerpts of how the voltage, current, and temperature vary when the cell is new versus aged.

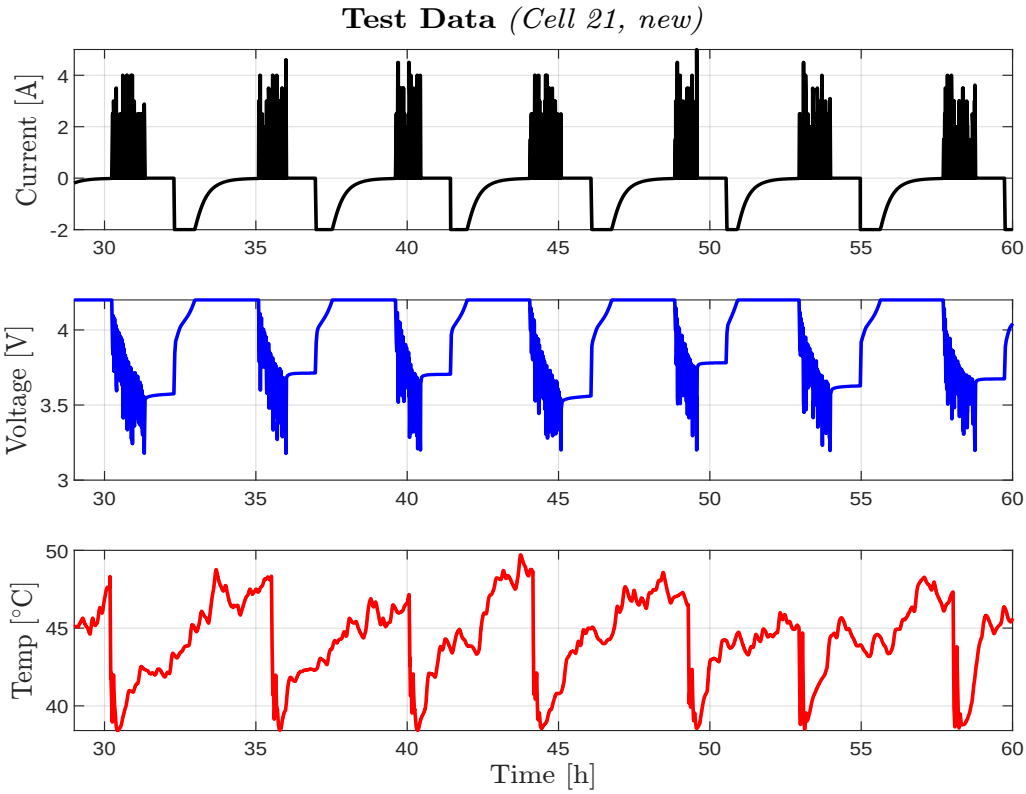

Figure 4.6: Extract from current, voltage and temperature measurements for new cell 21.

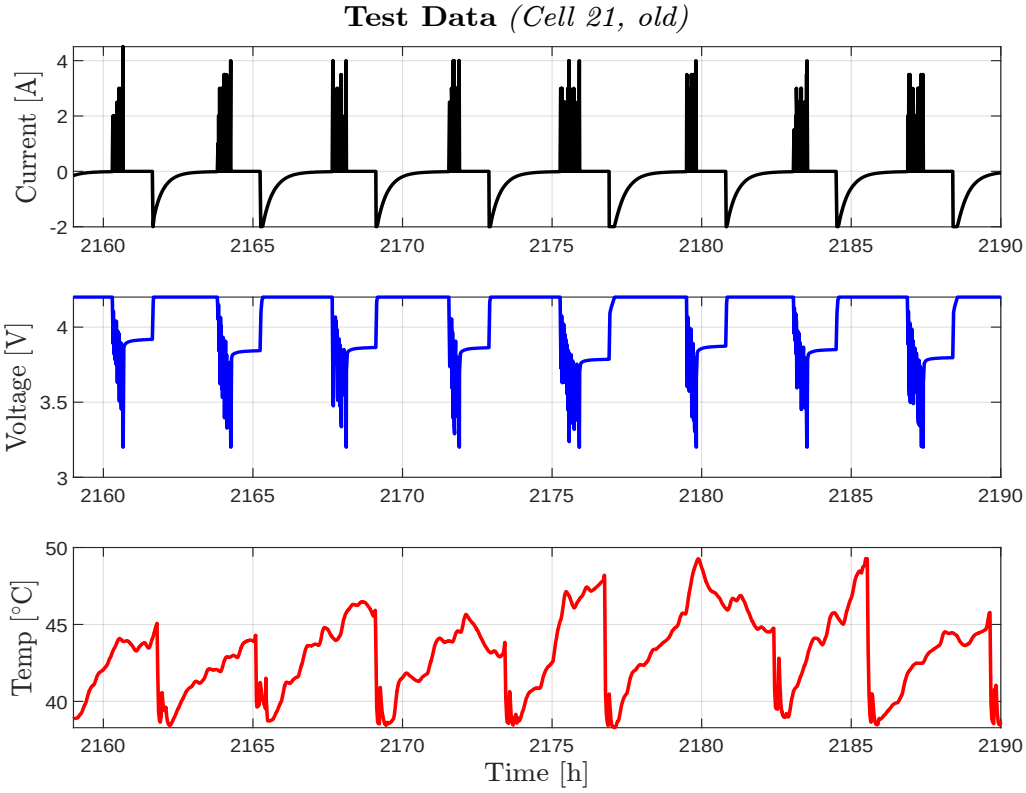

Figure 4.7: Extract from current, voltage and temperature measurements for aged cell 21.

4.4.3 Test case 2 - SOH estimation

In this test case, data from four cells that have undergone different tests are used. The four cells are numbered 13, 20, 21, and 25 from [34]. Cell number 13 was subjected to the "Skewed Low Room Temperature" test (Section 4.4). The next cell, number 20, underwent the "Skewed High Room Temperature" test. The following two cells (21 and 25) performed the same tests but at an ambient temperature of $40^{\circ}C$ instead of room temperature.

The simulation from the battery data is performed continuously over a period of more than 2200 hours (over 90 days). The purpose of this test is to observe how the implemented filters function over a longer period. This includes examining how they estimate capacity and internal resistance. The capacity estimates will be compared with the reference capacity checks performed on the respective cells, allowing us to assess the performance of the estimators.

The estimates for internal resistance and capacitance are also compared with estimates made using a least squares algorithm (Section 3.6). This comparison is for reference purposes only and should not necessarily be considered as the ground truth.

4.4.4 Test case 3 - Convergence of estimator

In this test case, the initial values of SOC are adjusted far from the true initial SOC. The purpose of the simulation is to assess how the estimators handle this in terms of convergence, stability, and correction of the initial error. This approach also aims to reveal any differences between JEKF and DEKF. It is important to note that since DEKF is divided into two parts, some covariance between SOC and battery parameters is lost.

These simulations will be conducted on cell 21 - Skewed High $40^{\circ}C$. Both for the new and aged states, in other words, the same data as for test case 1. The true initial SOC for this data is 1 (100%). Instead of initializing the filter at 0.6 like the other test, this simulation will initialize the SOC at 0%. Additionally, the initialization covariance for Σ_{SOC_0} will be increased from 10% to 50%. To increase robustness around the capacity estimate, Σ_Q will be decreased from 1% to 0.1% to state how confident we are in this initial value, compared to SOC.

Chapter 5

Results

In this chapter, the results of the parameter and OCV(SOC) function are presented, in addition to the results of test cases 1-3. The results aim to compare the performance of the seven implemented estimators: EKF-R, EKF-RC1, JEKF-R, JEKF-RC1, JEKF-RC1-Ext, DEKF-R, and DEKF-RC1. The designation R/RC1 indicates the battery model the estimator is based on.

The EKF estimators are used solely for SOC estimation, while the JEKF and DEKF estimators also estimate the SOH alongside SOC.

5.1 Identified initial parameters

With the use of nonlinear least squares, the initial parameters for the LCO cell are found [2].

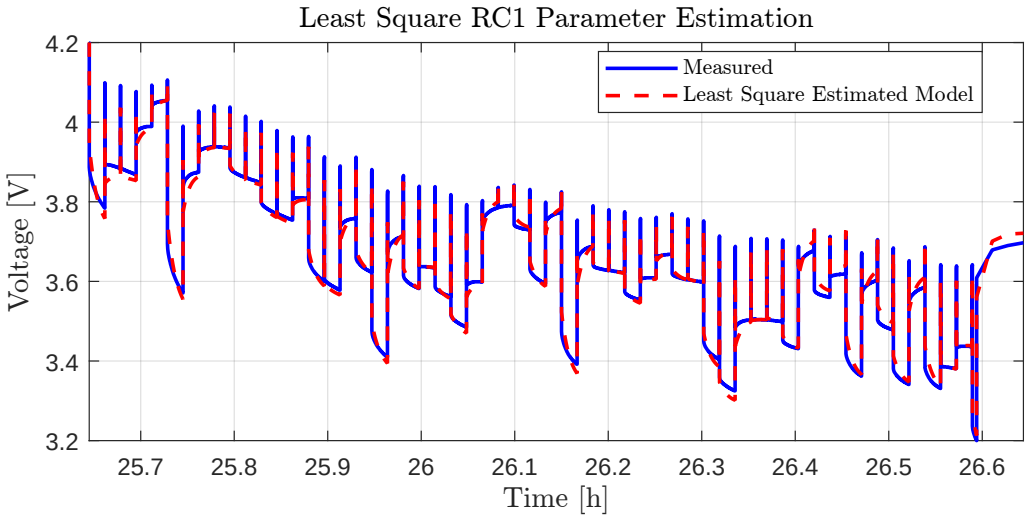

Figure 5.1: Least square algorithm solving parameter fitting to R and RC1 model.

From the least square algorithm (Section 3.6) used on cell 21 and its output shown in Figure 5.1, the initial battery parameters for the RC1 model are identified as follows:

$$R_0 = 86\,\text{m}\Omega, \quad R_1 = 56\,\text{m}\Omega, \quad C_1 = 500\,\text{F}$$

For the Rint model, the initial parameter identified using the least square algorithm:

$$R_0 = 135\,\text{m}\Omega$$

Since the dataset used contains 28 cells of the same type, the parameters are initiated the same for all tests conducted, even though the cells were not operated under the same conditions.

5.2 Identified OCV - SOC curve

As shown in Section 4.3.3 (Figure 4.4) a slow-dicharge charge cycle is performed on the LCO cell. The average voltage between these two curves is found, and by using the MATLAB `polyfit` function the approximation of this curve is created as a polynomial, where the degree is set to 12 to ensure good precision. Since all versions of the implemented filters involve differentiation at each timestep, the derivative of this function is derived using the `polyder` function in MATLAB. The resulting polynomial is listed below in Table 5.1.

Coefficient	**OCV** ($\times 10^5$)	**dOCV** ($\times 10^6$)
1	0.124775	0.137253
2	-0.729941	-0.729941
3	1.871935	1.684741
4	-2.765696	-2.212557
5	2.601213	1.820849
6	-1.623382	-0.974029
7	0.679167	0.339583
8	-0.187854	-0.075142
9	0.033048	0.009914
10	-0.003449	-0.000690
11	0.000193	0.000019
12	0.000032	

Table 5.1: Identified coefficients for the OCV and dOCV curves.

5.3 Test case 1 - EKF versus Joint and Dual EKF

This test case aims to compare a constant EKF against Joint and Dual EKF approaches on a battery cell, assessing estimator performance differences between the cell's new and aged condition. The tested cell, number 25 from the dataset, underwent the 'Skewed High 40°C' test. The simulation features several plots: SOC and voltage estimations for the Rint and RC1 models. Deviations between true and estimated values are calculated and displayed in tables and bar charts for both the new and aged conditions of the cell. The last part of this section includes figures of the parameter estimations done by the JEKF and DEKF.

5.3.1 New cell

The following plots are from test case 1 on cell number 25 when it was new, covering operational hours from 20 to 220.

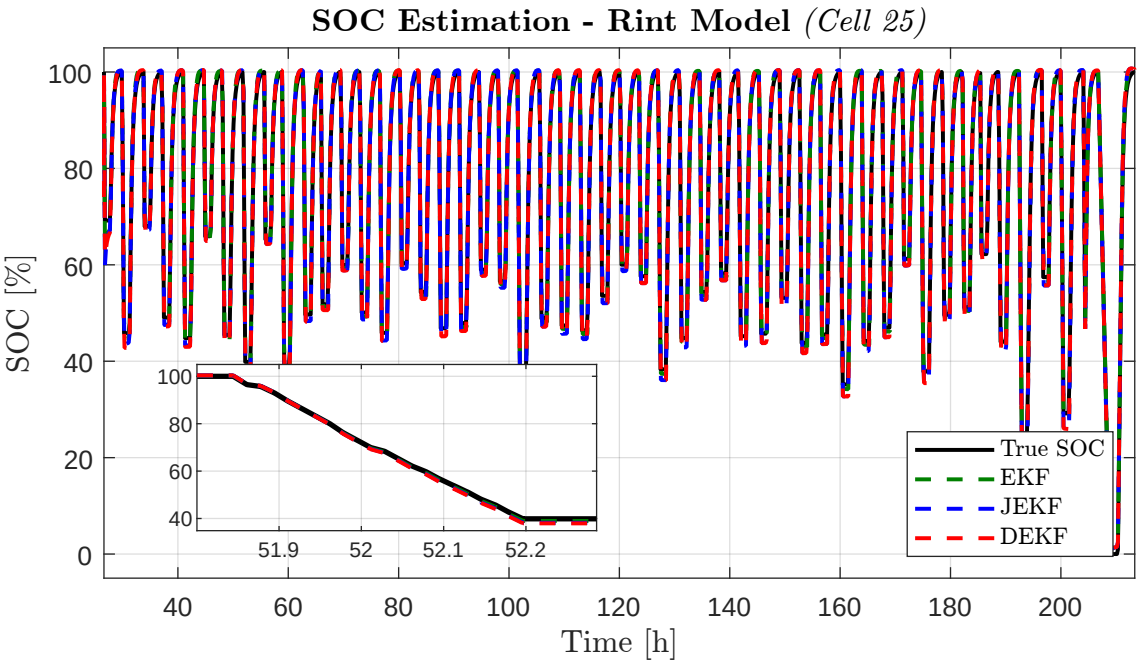

Figure 5.2: Comparison of SOC estimation using EKF-R, JEKF-R, and DEKF-R for new cell number 25, operated at an ambient temperature of 40°C.

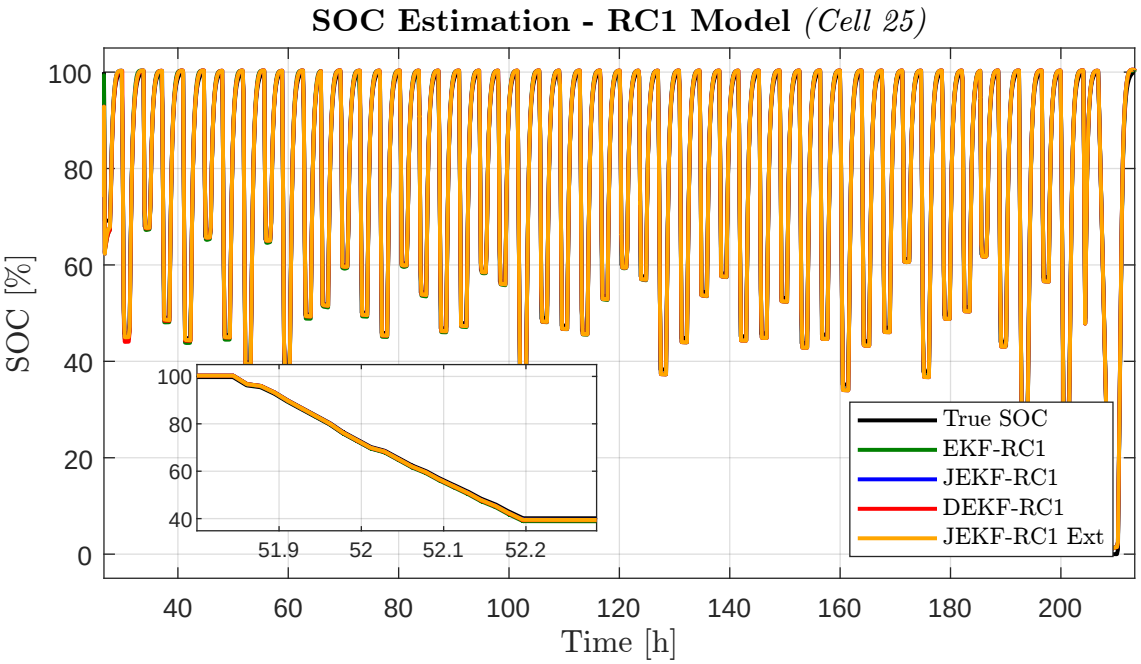

Figure 5.3: Comparison of SOC estimation using EKF-RC1, JEKF-RC1, JEKF-RC1-Ext, and DEKF-RC1 for new cell number 25, operated at an ambient temperature of 40°C. See Table 5.2 for estimation errors.

Estimator	**RMSE**	**MAE**
EKF R	0.84 %	0.72 %
EKF RC1	0.86 %	0.72 %
JEKF R	1.22 %	1.00 %
JEKF RC1	0.72 %	0.58 %
DEKF R	1.26 %	1.04 %
DEKF RC1	0.76 %	0.61 %
JEKF RC1 Ext	0.74 %	0.59 %

Table 5.2: Calculated RMSE and MAE SOC estimation errors for new cell number 25.

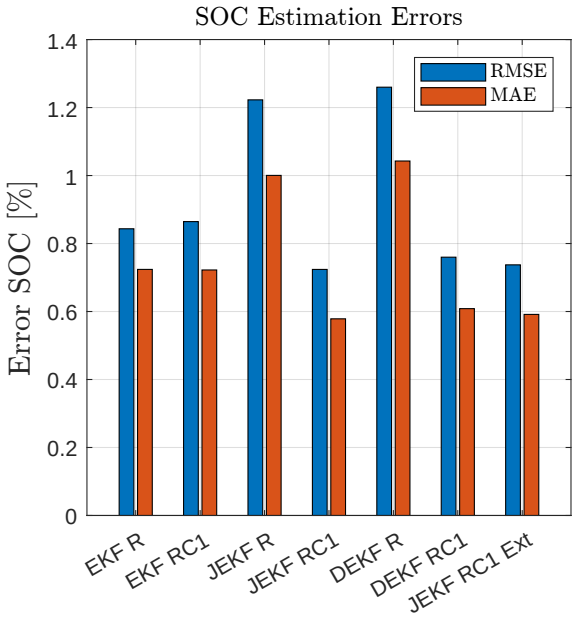

Figure 5.4: SOC estimation error bar chart for new cell number 25.

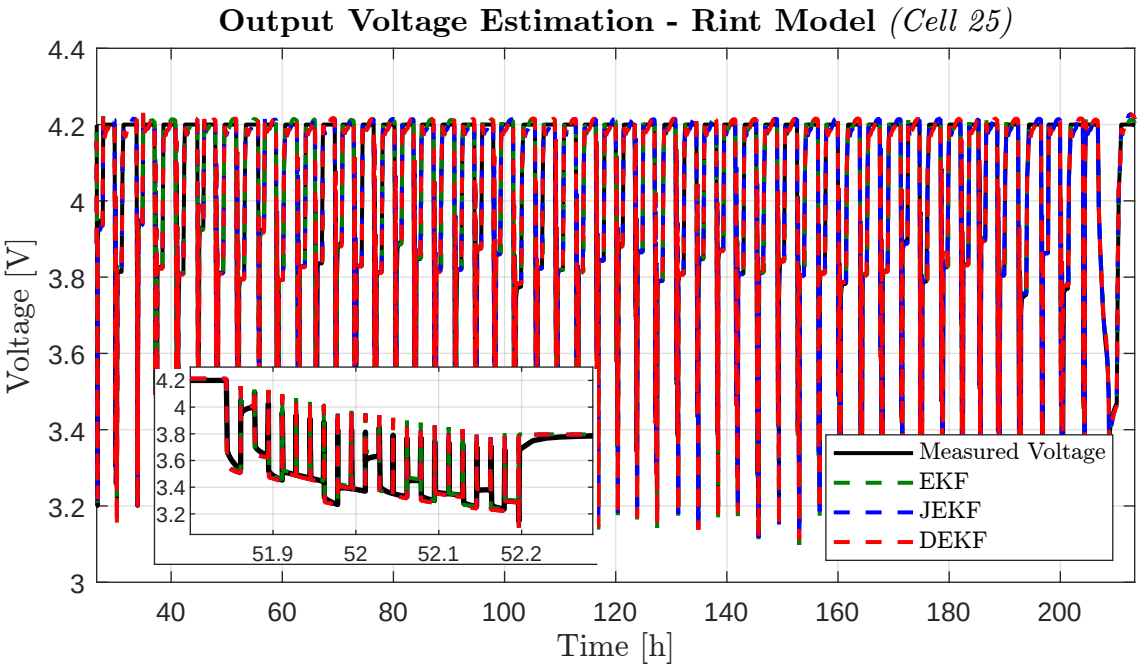

Figure 5.5: Comparison of output voltage estimation using EKF-R, JEKF-R, and DEKF-R for new cell number 25, operated at an ambient temperature of 40°C.

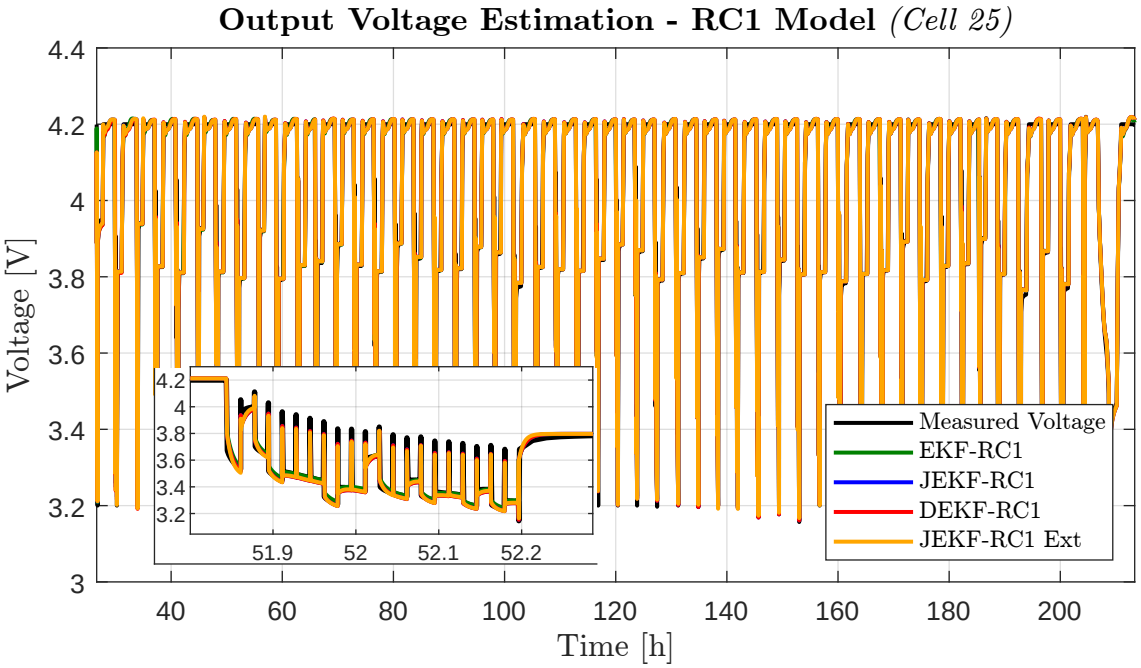

Figure 5.6: Comparison of output voltage estimation using EKF-RC1, JEKF-RC1, JEKF-RC1-Ext and DEKF-RC1 for new cell number 25, operated at an ambient temperature of 40°C.

Estimator	**RMSE**	**MAE**
EKF R	32.8 mV	13.4 mV
EKF RC1	22.4 mV	11.4 mV
JEKF R	32.8 mV	14.0 mV
JEKF RC1	22.5 mV	11.8 mV
DEKF R	32.8 mV	14.1 mV
DEKF RC1	22.5 mV	11.9 mV
JEKF RC1 Ext	22.5 mV	11.9 mV

Table 5.3: Calculated RMSE and MAE output estimation errors for new cell number 25.

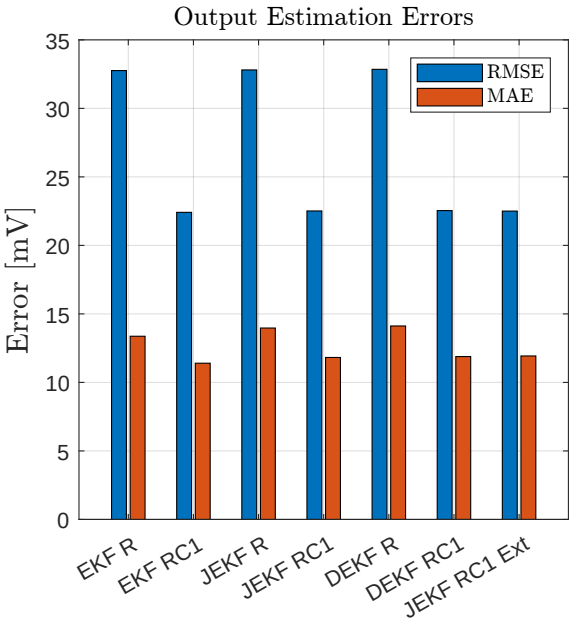

Figure 5.7: Output voltage estimation bar chart for new cell number 25.

5.3.2 Aged cell

The following figures are from test case 1 on cell number 25 when it was aged, covering operational hours from 1820 to 1980 after the test was initiated.

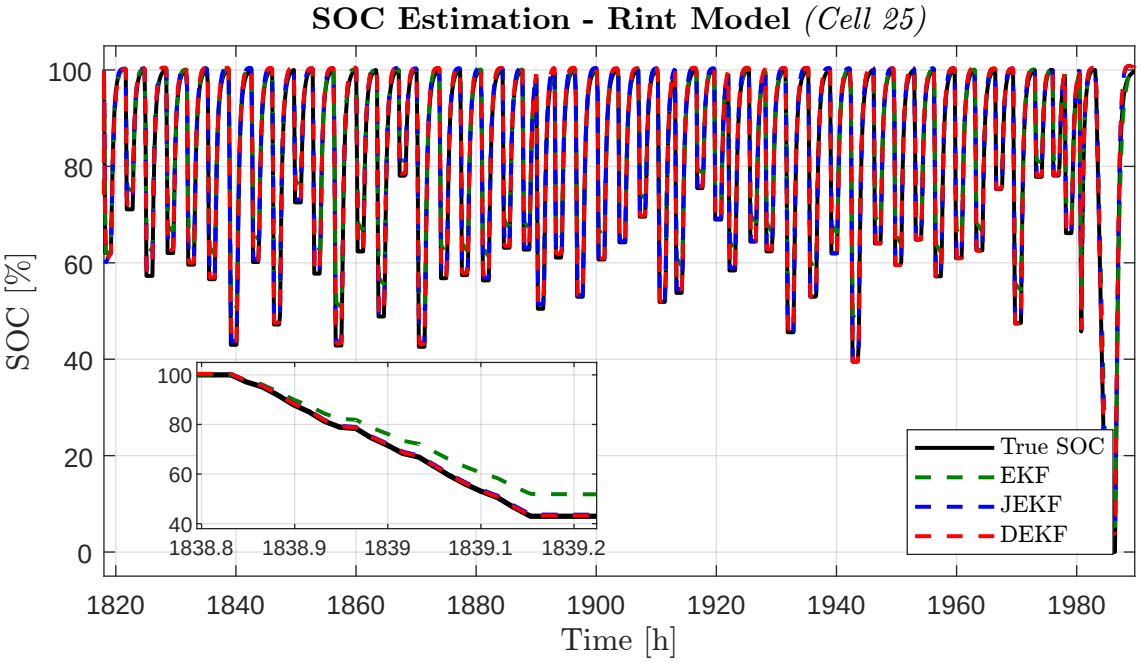

Figure 5.8: Comparison of SOC estimation using EKF-R, JEKF-R, and DEKF-R for aged cell number 25, operated at an ambient temperature of 40°C.

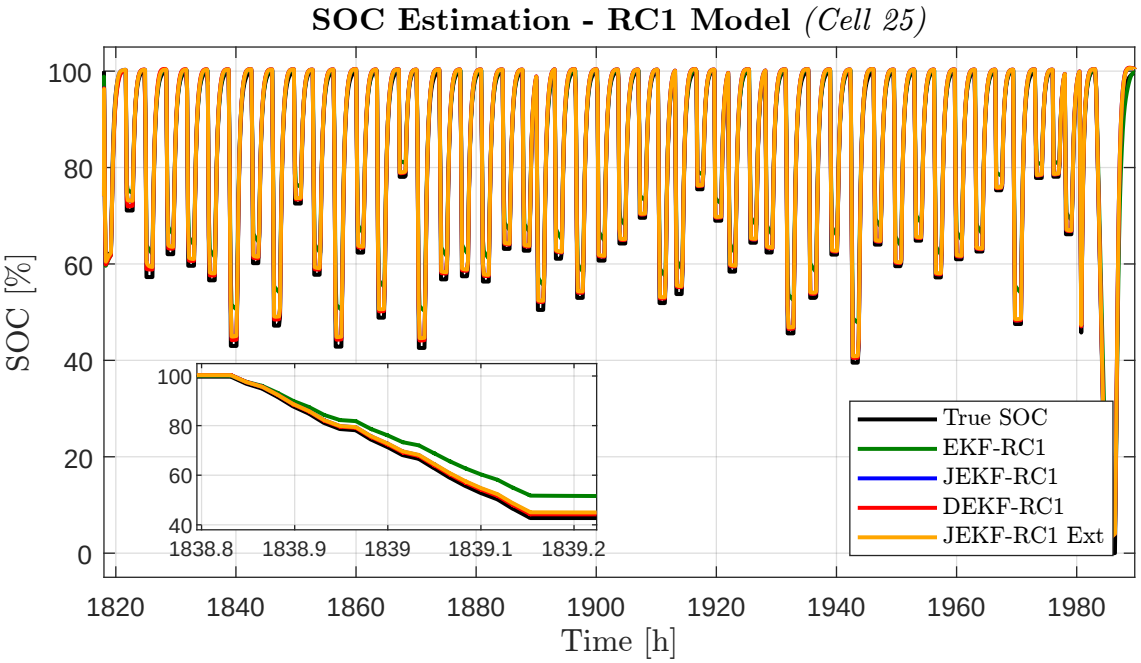

Figure 5.9: Comparison of SOC estimation using EKF-RC1, JEKF-RC1, JEKF-RC1-Ext and DEKF-RC1 for aged cell number 25, operated at an ambient temperature of 40°C.

Estimator	RMSE	MAE
EKF R	3.56 %	2.44 %
EKF RC1	3.43 %	2.33 %
JEKF R	0.92 %	0.74 %
JEKF RC1	1.06 %	0.93 %
DEKF R	0.93 %	0.72 %
DEKF RC1	1.04 %	0.92 %
JEKF RC1 Ext	1.11 %	0.98 %

Table 5.4: Calcultated RMSE and MAE SOC estimation errors for aged cell number 25.

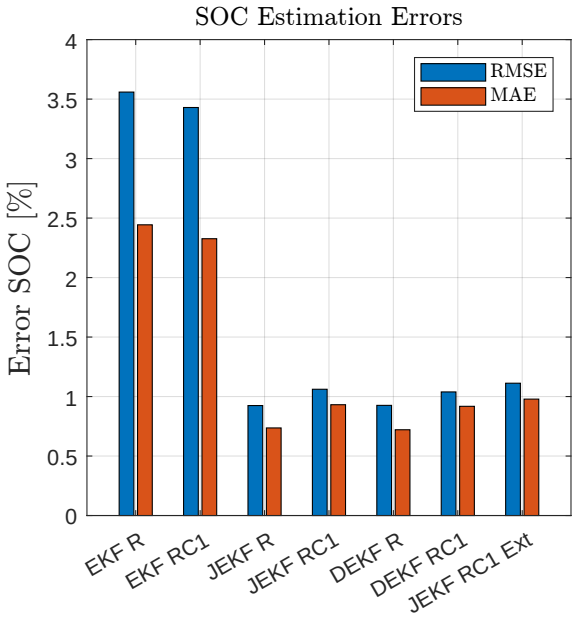

Figure 5.10: SOC estimation error bar chart for aged cell number 25.

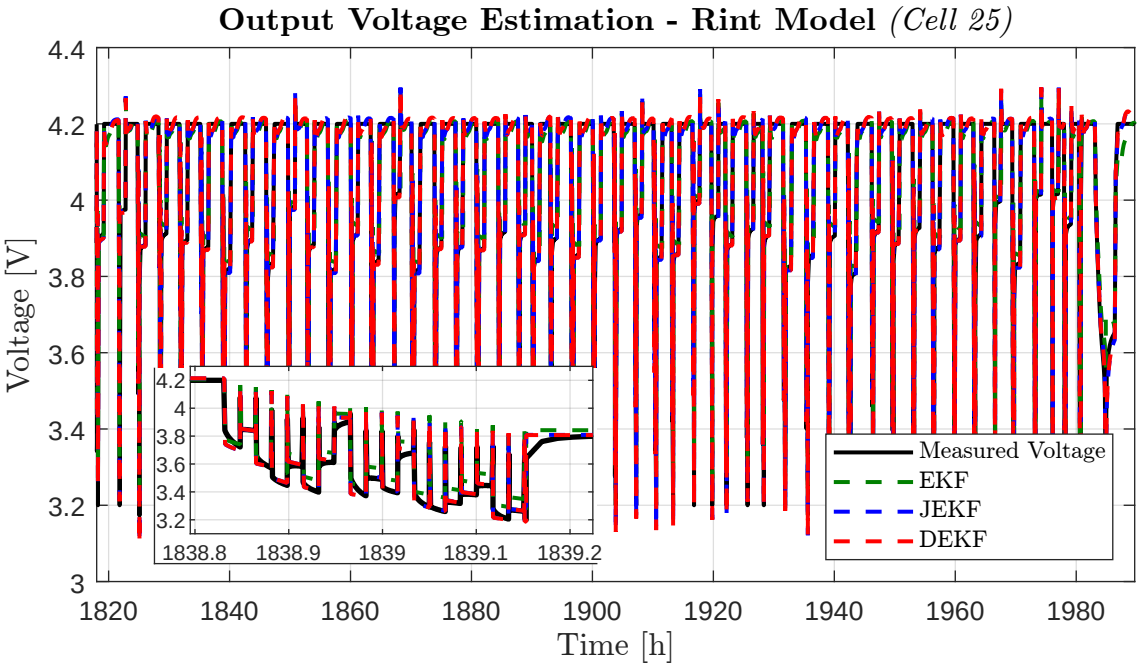

Figure 5.11: Comparison of Output Voltage Estimation using EKF-RC1, JEKF-RC1, JEKF-RC1-Ext and DEKF-RC1 for aged cell number 25, operated at an ambient temperature of 40°C.

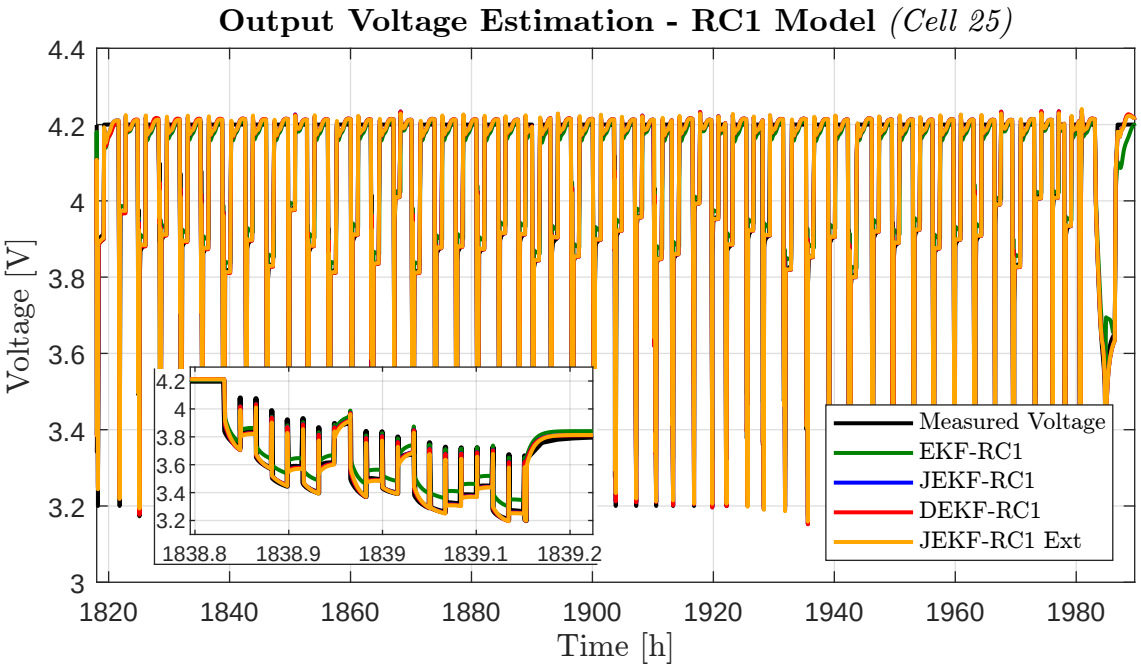

Figure 5.12: Comparison of output voltage estimation using EKF-RC1, JEKF-RC1, JEKF-RC1-Ext and DEKF-RC1 for aged cell number 25, operated at an ambient temperature of 40°C.

Estimator	**RMSE**	**MAE**
EKF R	45.4 mV	26.7 mV
EKF RC1	38.5 mV	25.2 mV
JEKF R	33.7 mV	15.4 mV
JEKF RC1	22.7 mV	12.2 mV
DEKF R	33.7 mV	15.6 mV
DEKF RC1	22.7 mV	12.3 mV
JEKF RC1 Ext	21.9 mV	12.4 mV

Table 5.5: Calcultated RMSE and MAE output estimation errors for aged cell number 25.

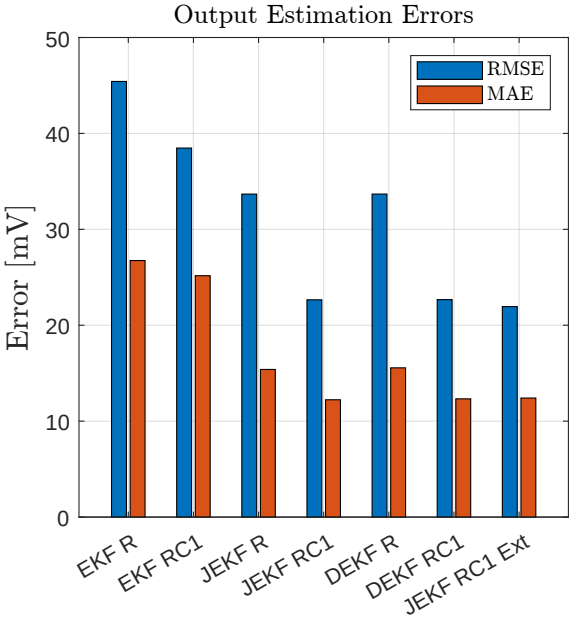

Figure 5.13: Output voltage estimation bar chart for aged cell number 25.

5.3.3 Capacity estimation error for new and aged cell

The following figures (Figure 5.14 and 5.15) and tables (Table 5.6 and 5.7) displays the predictions of battery capacity made by the dual estimators, along with the associated errors, for test case 1 conducted on new and aged cells. The convergence of the filter shows its good ability to quickly find the "true" value, in only a few hours of estimation.

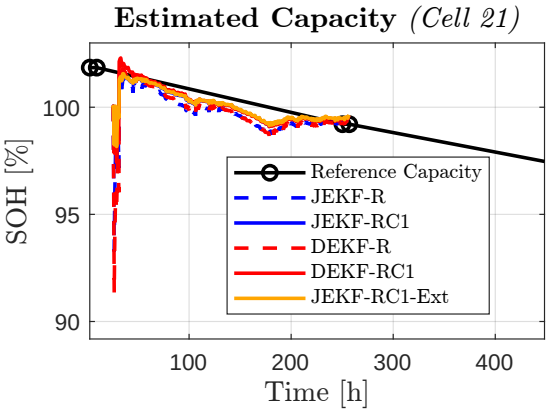

Figure 5.14: Capacity estimation for new cell.

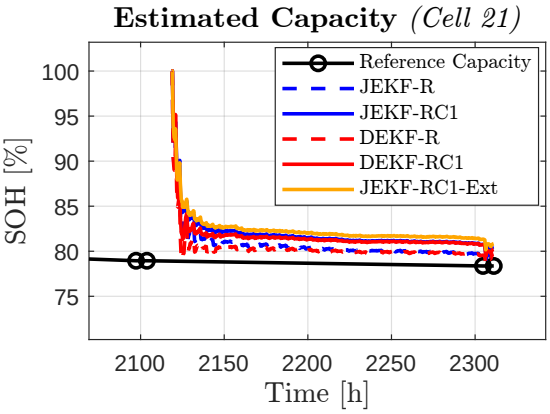

Figure 5.15: Capacity estimation for aged cell.

Estimator	**RMSE**	**MAE**
JEKF R	0.96 %	0.68 %
JEKF RC1	0.54 %	0.39 %
DEKF R	1.14 %	0.67 %
DEKF RC1	0.60 %	0.39 %
JEKF RC1 Ext	0.52 %	0.37 %

Table 5.6: Capacity estimation error for new cell.

Estimator	**RMSE**	**MAE**
JEKF R	2.62 %	2.03 %
JEKF RC1	3.65 %	3.20 %
DEKF R	2.19 %	1.64 %
DEKF RC1	3.33 %	2.91 %
JEKF RC1 Ext	4.06 %	3.71 %

Table 5.7: Capacity estimation error for aged cell.

Figure 5.14 and 5.15 shows how the dual filters estimated the capacity during test case 1.

5.3.4 Internal resistance estimation new versus aged

The following plots shows the estimated parameters for JEKF-R, JEKF-RC1, DEKF-R and DEKF-RC1 during the tests conducted in test case 1. The initial parameters and tuning variables for all the filters are the same for both the simulation for new and aged cell. The estimated values are here compared to the Least Squared Estimates done separately.

New cell

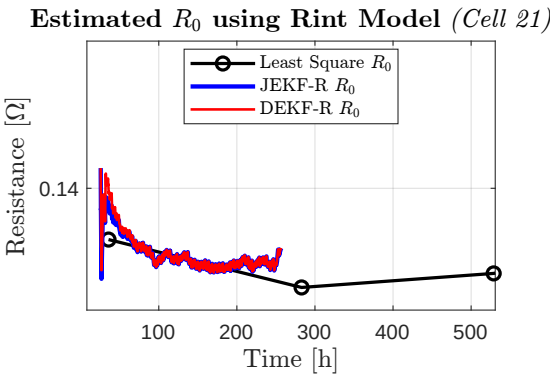

Figure 5.16: Estimated R_0 for new cell test case 1 for JEKF-R and DEKF-R.

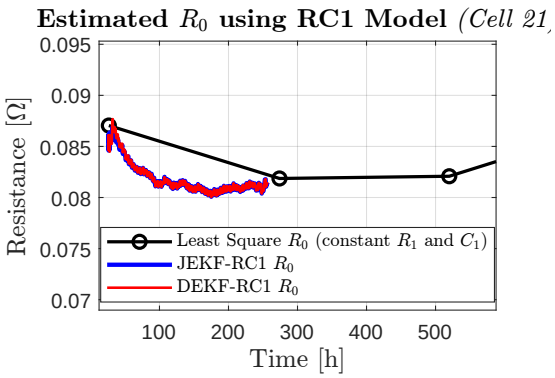

Figure 5.17: Estimated R_0 for new cell test case 1 for JEKF-RC1 and DEKF-RC1.

Aged cell

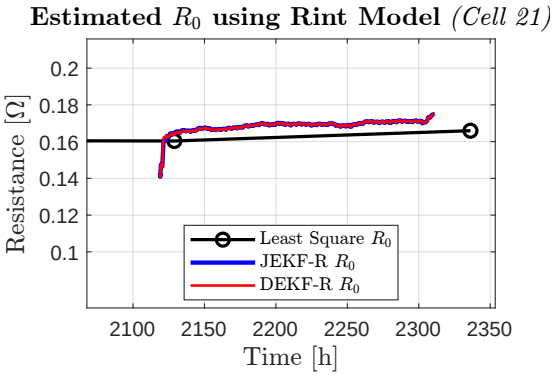

Figure 5.18: Estimated R_0 for aged cell test case 1 for JEKF-R and DEKF-R.

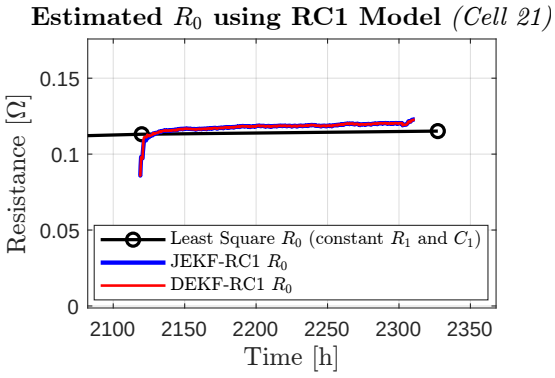

Figure 5.19: Estimated R_0 for aged cell test case 1 for JEKF-RC1 and DEKF-RC1.

5.4 Test case 2 - SOH estimation

The following results are from test case 2. Unlike test case 1, the estimators in this test were run on data spanning over 2000 hours. As this test was conducted on four different cells, the plots are organized cell by cell. For each cell, a plot of the capacity estimate is included, which includes all implemented SOH estimators, translated from estimated capacity to SOH [%]. This is followed by an estimation error table that calculates the deviation in terms of RMSE and MAE for the estimation, where the reference capacity tests performed on the battery are assumed to be ground truth.

Subsequent plots show the estimated internal resistance for JEKF-R and DEKF-R, compared with least square estimates performed periodically on the battery set. The following plot is the estimated resistance, R_0, for JEKF-RC1 and DEKF-RC1. The resistance estimated here will be lower than for models based on the Rint battery model, as in the RC1 model for these two filters includes a constant RC element. The estimation for this also includes a least square estimate where the RC element in the battery model is set constant.

The next plot is the estimated R_0 and R_1 for JEKF-RC1-Ext. This filter estimates capacity, R_0, R_1 and C_1 in addition to SOC. The results for this are compared with least square estimates where all parameters are calculated. This is followed by the last plot for estimated capacitance in the RC1 circuit, C_1, for JEKF-RC1-Ext, compared against the same least square estimate.

5.4.1 Cell 13 - Skewed low room temperature

Cell tested in room temperature, with current skewed towards lower values (Section 4.3).

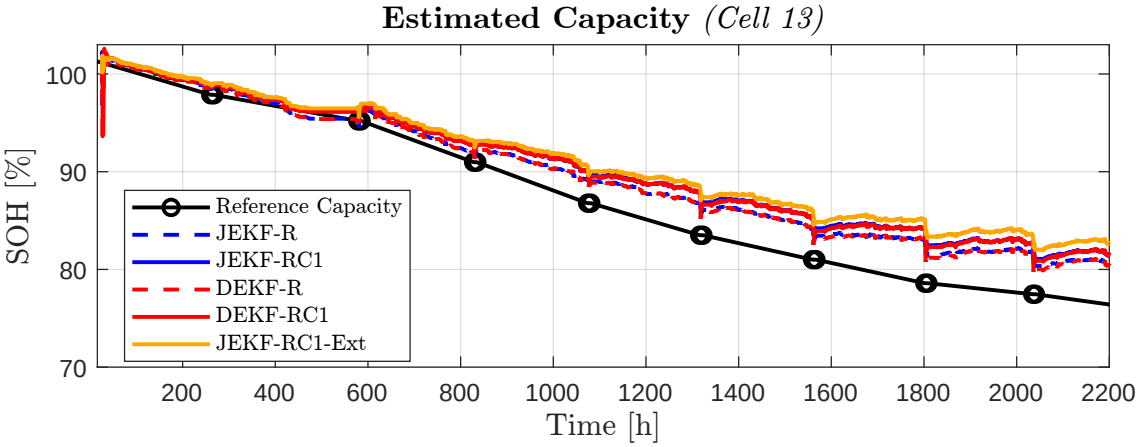

Figure 5.20: Comparison of capacity estimates from JEKF and DEKF against reference capacity test for cell number 13.

Estimator	**RMSE**	**MAE**
JEKF R	2.80 %	2.44 %
JEKF RC1	3.59 %	3.18 %
DEKF R	2.74 %	2.37 %
DEKF RC1	3.56 %	3.13 %
JEKF RC1 Ext	4.23 %	3.74 %

Table 5.8: Capacity estimation errors cell 13 (RMSE and MAE).

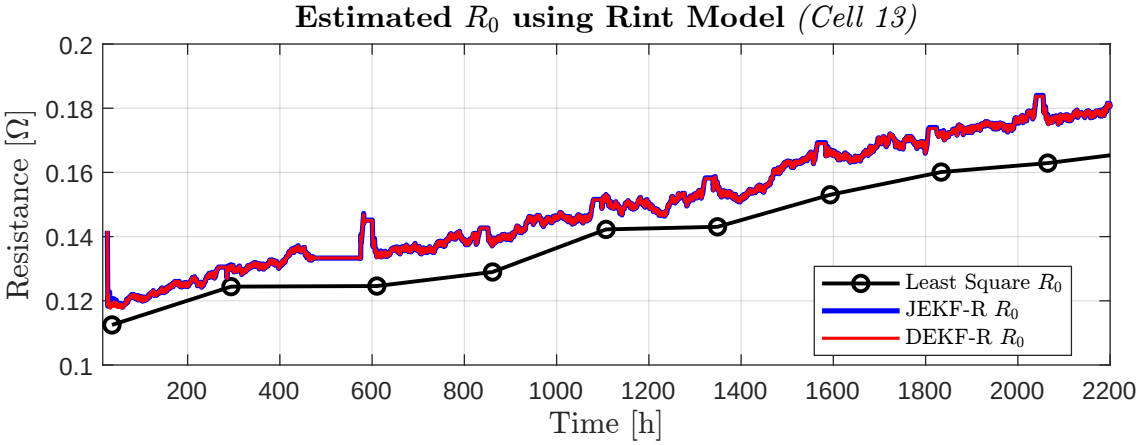

Figure 5.21: Simulation results for estimated R_0 using JEKF-R and DEKF-R filter of cell number 13, compared to least square estimates.

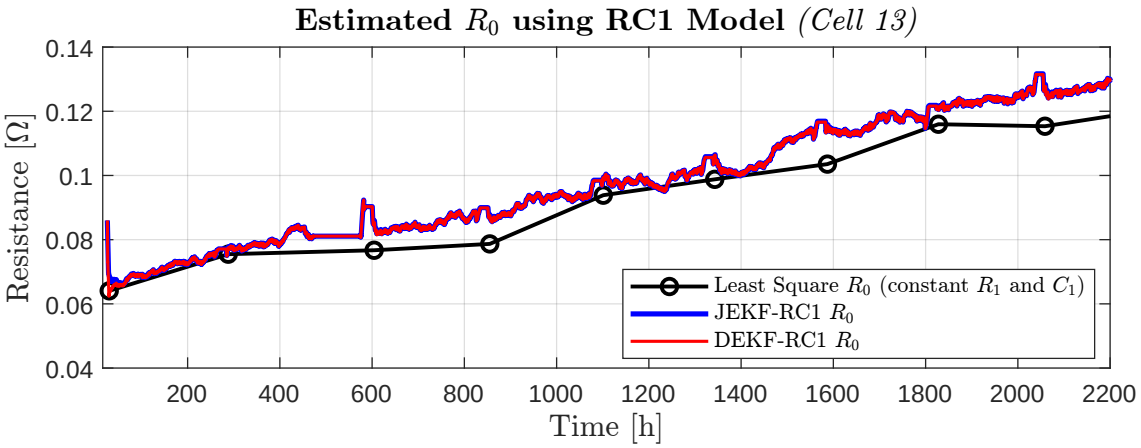

Figure 5.22: Simulation results for estimated R_0 using JEKF-RC1 and DEKF-RC1 filter of cell number 13, compared to least square estimates.

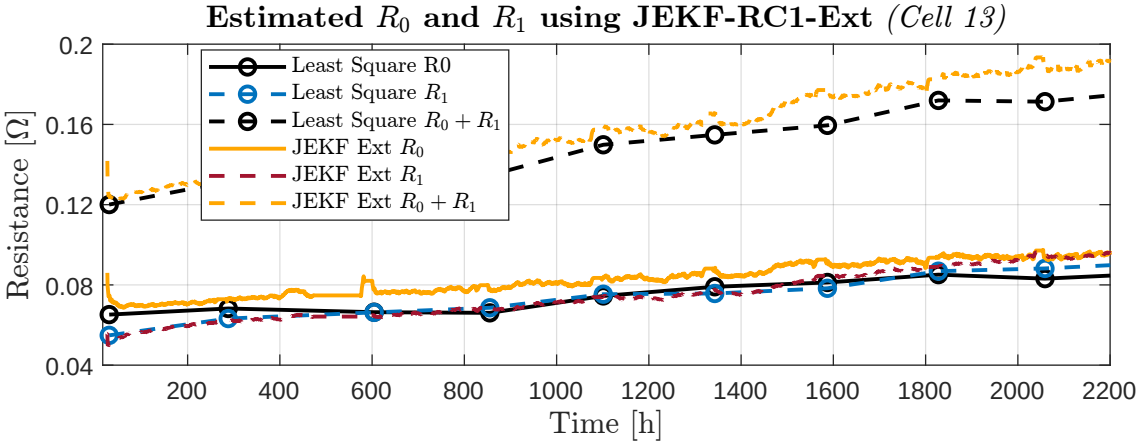

Figure 5.23: Simulation results for estimated R_0 and R_1 using JEKF-RC1-Ext filter of cell number 13, compared to least square estimates.

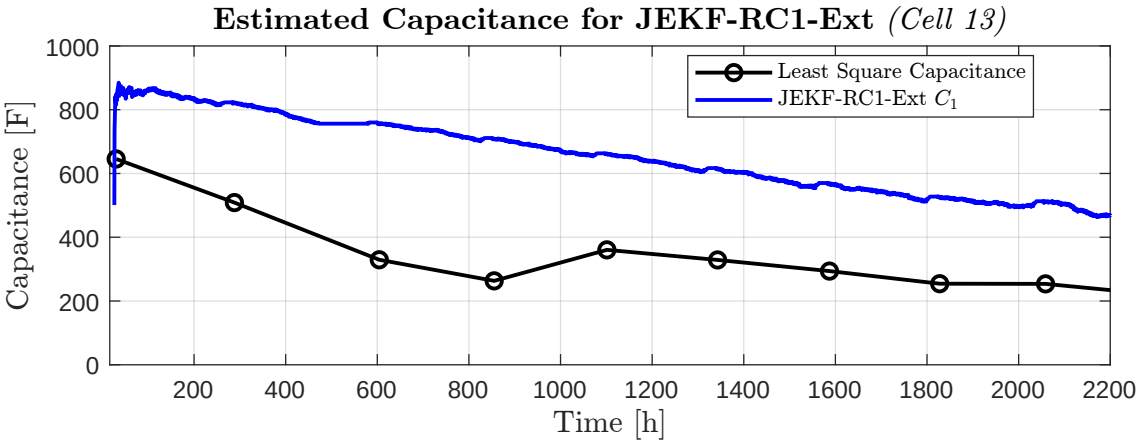

Figure 5.24: Simulation results for estimated C_1 using JEKF-RC1-Ext filter of cell number 13, compared to least square estimates.

5.4.2 Cell 20 - Skewed high room temperature

Cell 20 tested in room temperature, with current skewed towards higher values (Section 4.3).

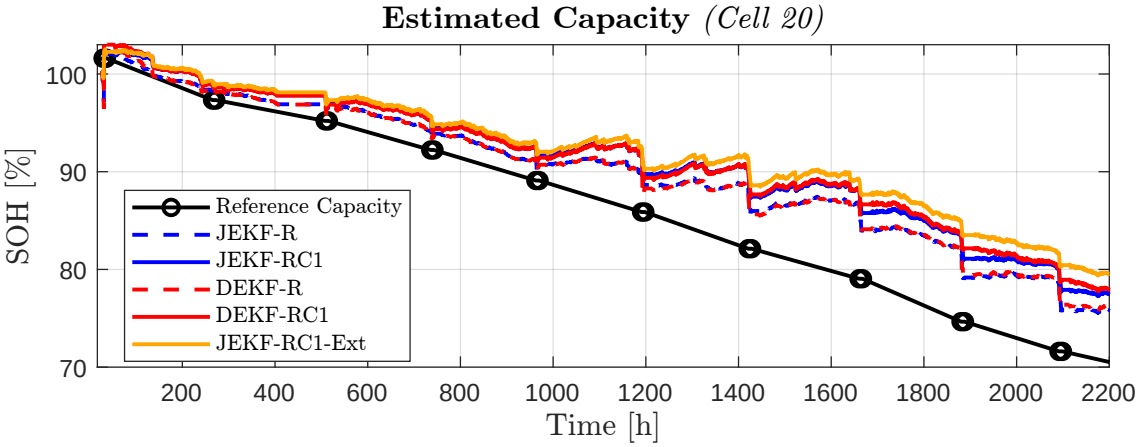

Figure 5.25: Comparison of capacity estimates from JEKF and DEKF against reference capacity test for cell number 20.

Estimator	**RMSE**	**MAE**
JEKF R	4.48 %	3.87 %
JEKF RC1	5.79 %	5.18 %
DEKF R	4.51 %	3.89 %
DEKF RC1	5.98 %	5.32 %
JEKF RC1 Ext	6.88 %	6.12 %

Table 5.9: Capacity estimation errors cell 20 (RMSE and MAE).

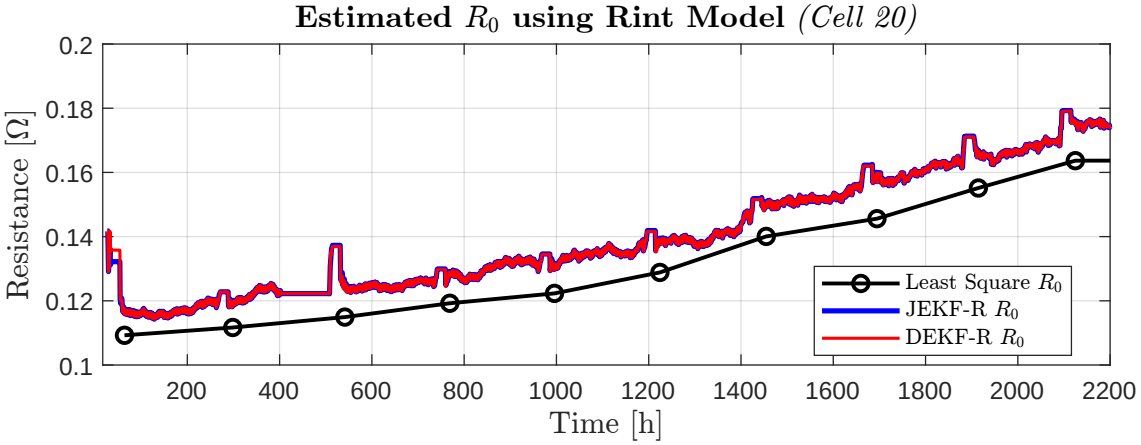

Figure 5.26: Simulation results for estimated R_0 using JEKF-R and DEKF-R filter of cell number 20, compared to least square estimates.

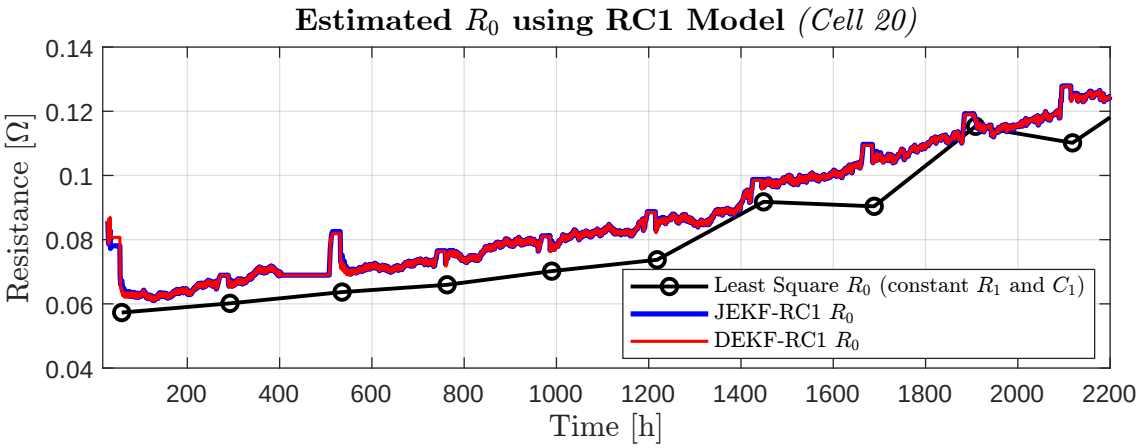

Figure 5.27: Simulation results for estimated R_0 using JEKF-RC1 and DEKF-RC1 filter of cell number 20, compared to least square estimates.

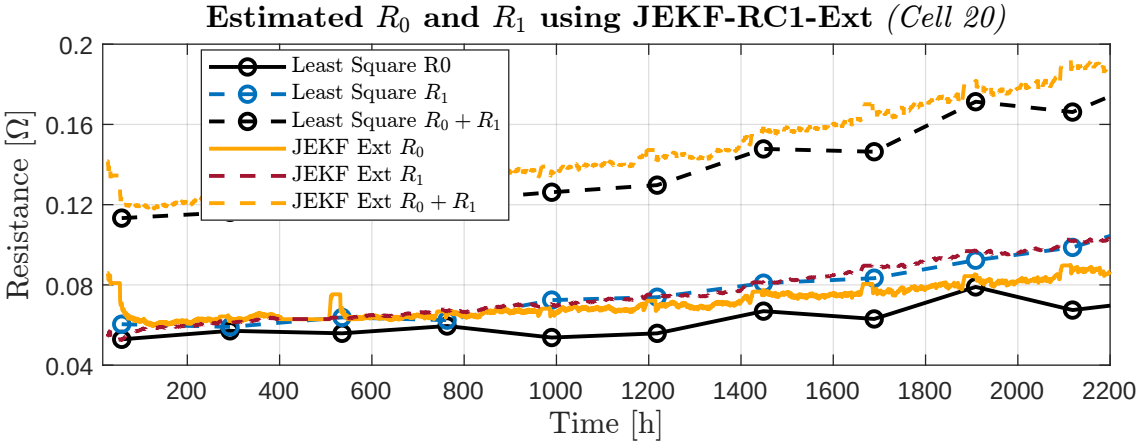

Figure 5.28: Simulation results for estimated R_0 and R_1 using JEKF-RC1-Ext filter of cell number 20, compared to least square estimates.

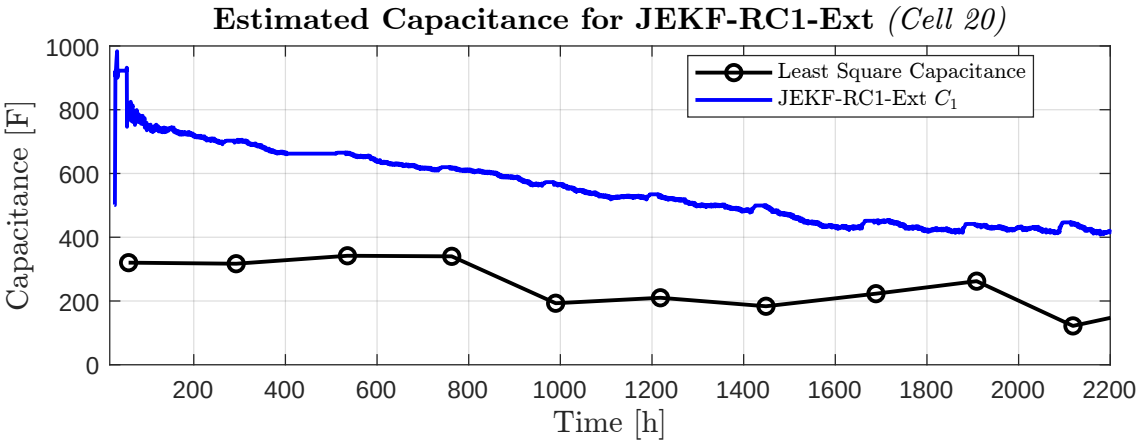

Figure 5.29: Simulation results for estimated C_1 using JEKF-RC1-Ext filter of cell number 20, compared to least square estimates.

5.4.3 Cell 21 - Skewed low 40°C

Cell tested in 40°C, with current skewed towards lower values (Section 4.3).

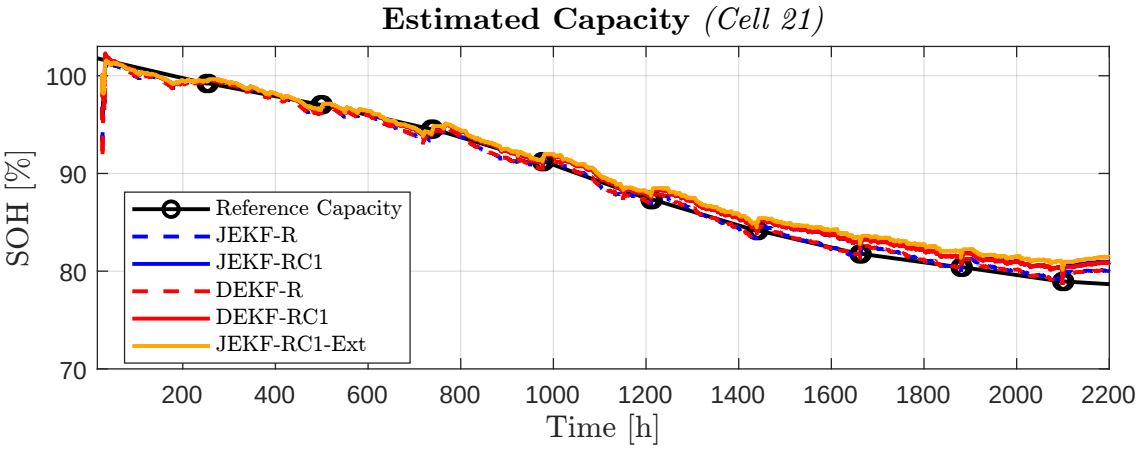

Figure 5.30: Comparison of capacity estimates from JEKF and DEKF against reference capacity test for cell number 21.

Estimator	**RMSE**	**MAE**
JEKF R	0.65 %	0.49 %
JEKF RC1	1.03 %	0.82 %
DEKF R	0.68 %	0.50 %
DEKF RC1	1.02 %	0.81 %
JEKF RC1 Ext	1.33 %	1.06 %

Table 5.10: Capacity estimation errors cell 21 (RMSE and MAE).

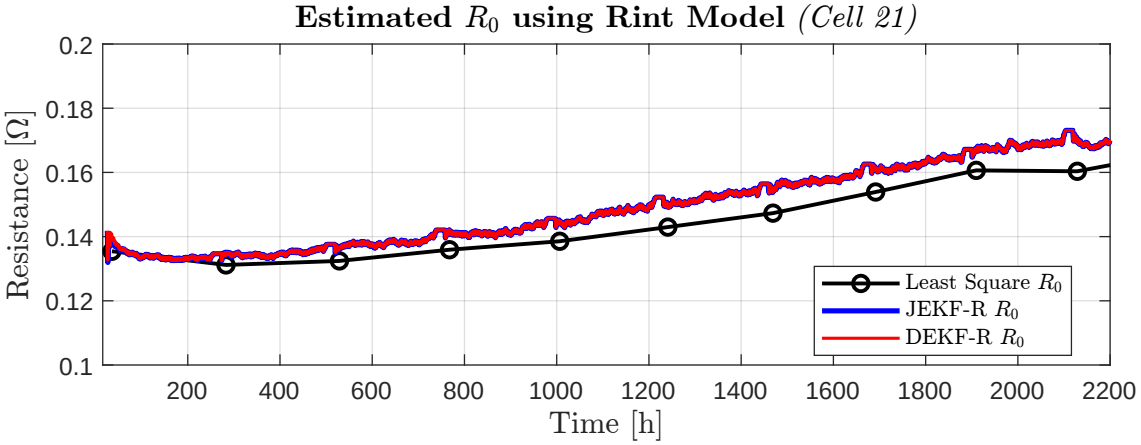

Figure 5.31: Simulation results for estimated R_0 using JEKF-R and DEKF-R filter of cell number 21, compared to least square estimates.

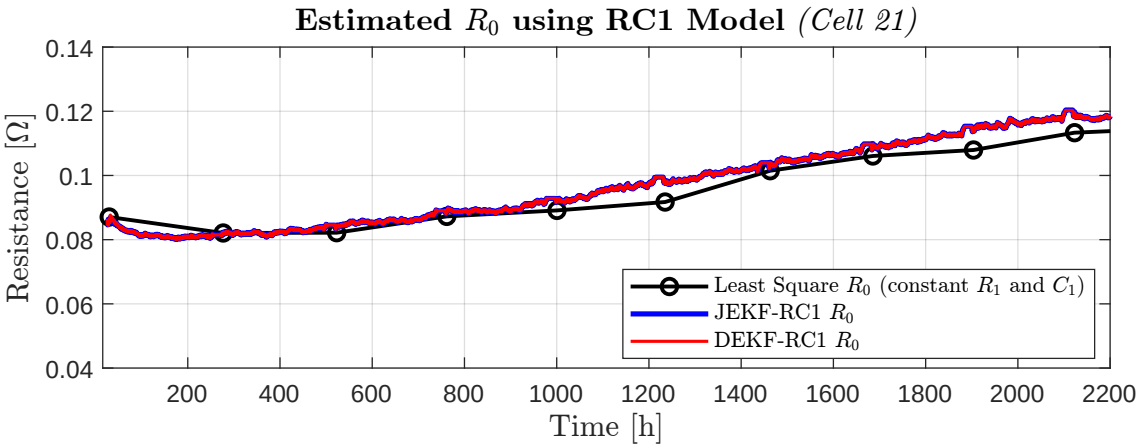

Figure 5.32: Simulation results for estimated R_0 using JEKF-RC1 and DEKF-RC1 filter of cell number 21, compared to least square estimates.

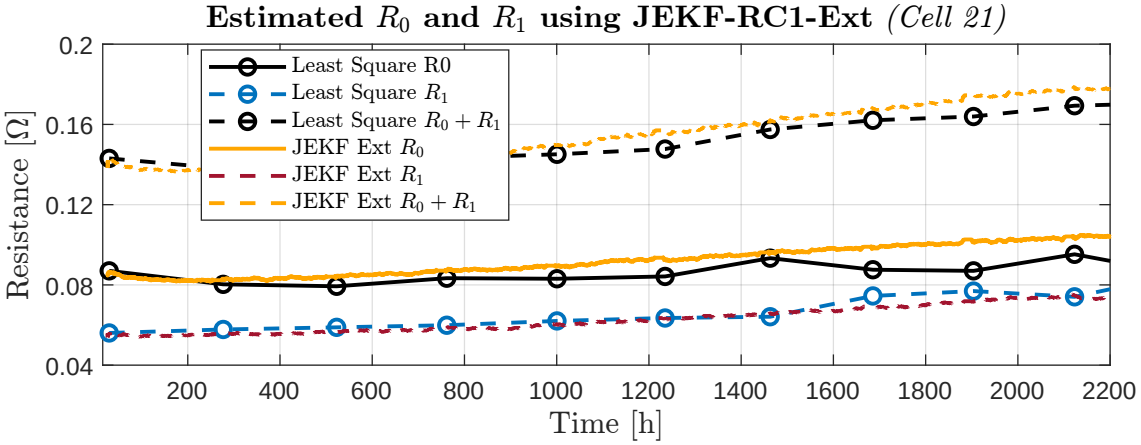

Figure 5.33: Simulation results for estimated R_0 and R_1 using JEKF-RC1-Ext filter of cell number 21, compared to least square estimates.

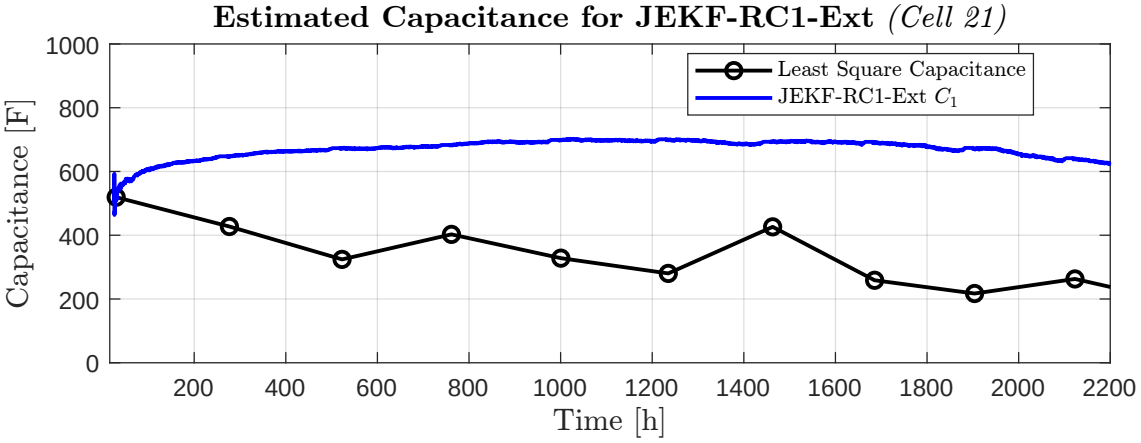

Figure 5.34: Simulation results for estimated C_1 using JEKF-RC1-Ext filter of cell number 21, compared to least square estimates.

5.4.4 Cell 25 - Skewed high 40°C

Cell tested in 40°C, with current skewed towards higher values (Section 4.3).

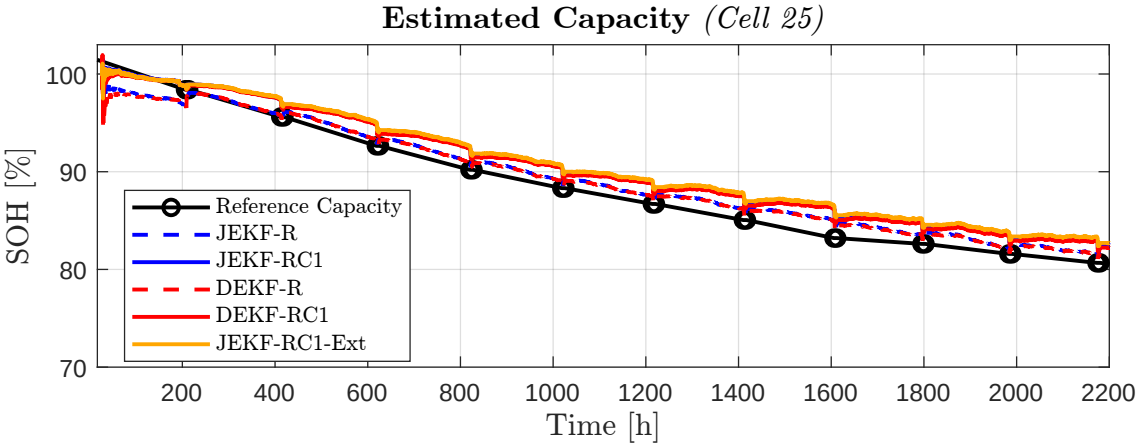

Figure 5.35: Comparison of capacity estimates from JEKF and DEKF against reference capacity test for cell number 25.

Estimator	**RMSE**	**MAE**
JEKF R	1.17 %	1.06 %
JEKF RC1	2.02 %	1.94 %
DEKF R	1.18 %	1.04 %
DEKF RC1	1.91 %	1.83 %
JEKF RC1 Ext	2.23 %	2.13 %

Table 5.11: Capacity estimation errors cell 25 (RMSE and MAE).

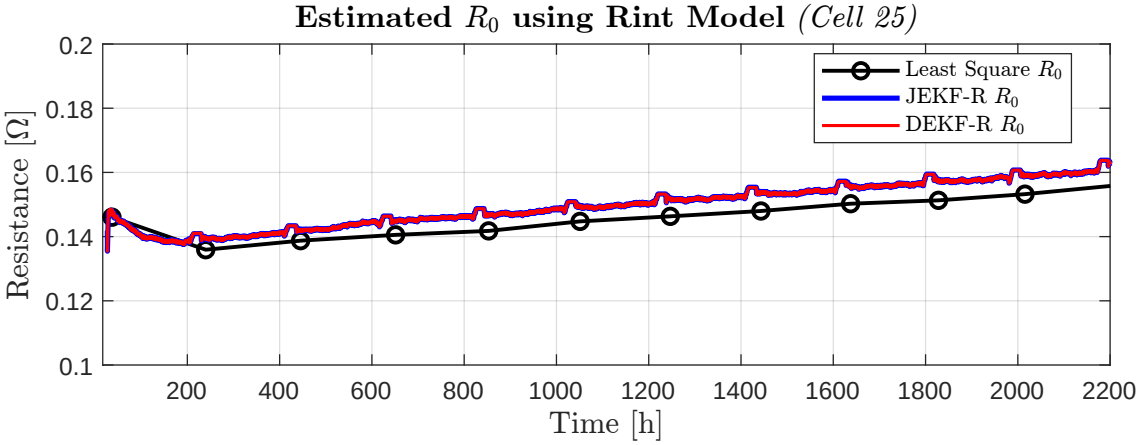

Figure 5.36: Simulation results for estimated R_0 using JEKF-R and DEKF-R filter of cell number 25, compared to least square estimates.

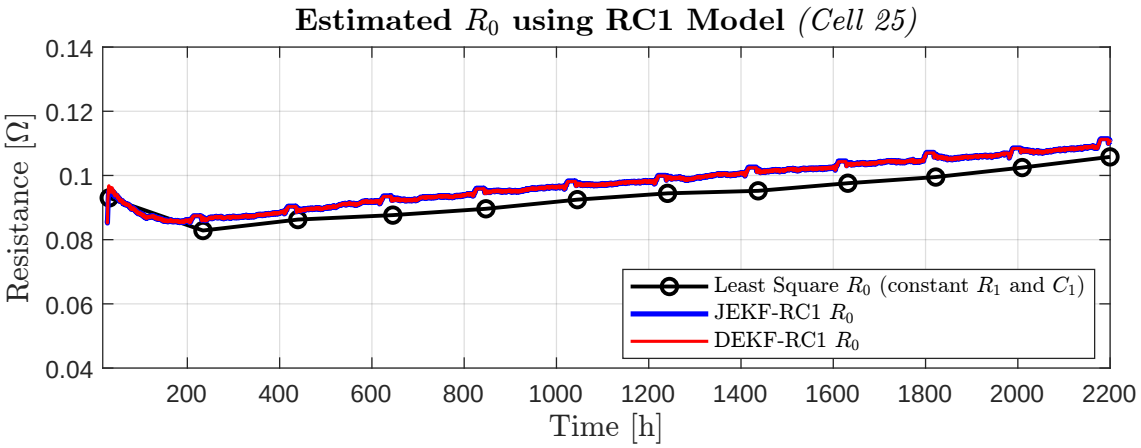

Figure 5.37: Simulation results for estimated R_0 using JEKF-RC1 and DEKF-RC1 filter of cell number 25, compared to least square estimates.

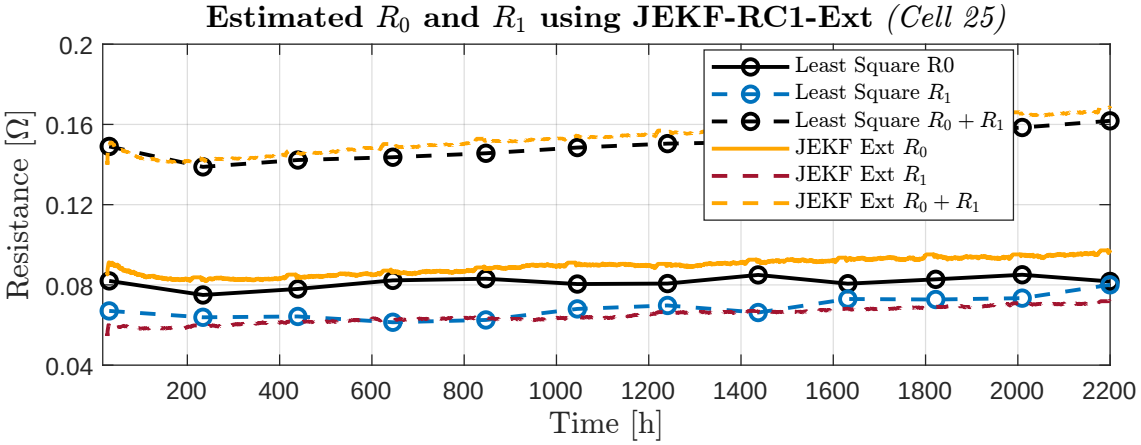

Figure 5.38: Simulation results for estimated R_0 and R_1 using JEKF-RC1-Ext filter of cell number 25, compared to least square estimates.

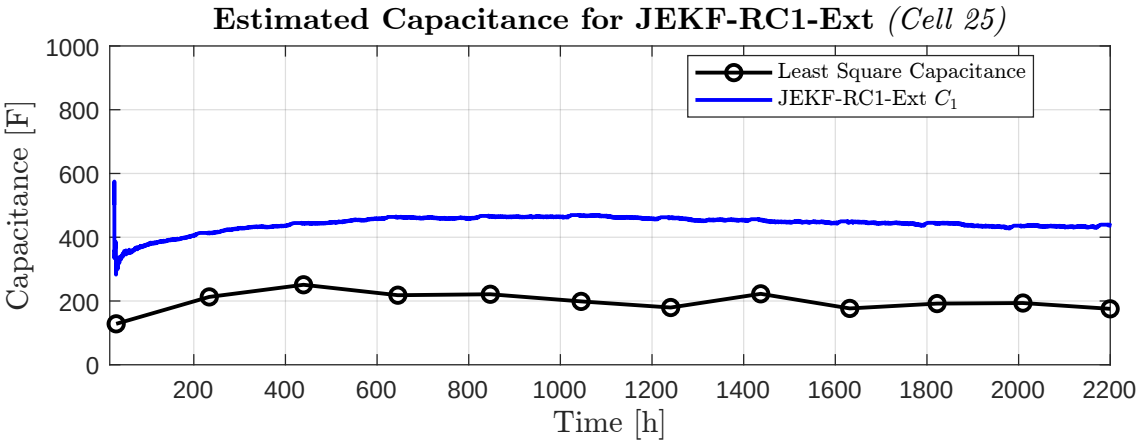

Figure 5.39: Simulation results for estimated C_1 using JEKF-RC1-Ext filter of cell number 25, compared to least square estimates.

5.5 Test case 3 - Convergence of estimator

In this test case, the SOC is initialized at 0%, aiming to evaluate the robustness of the DEKF and JEKF estimators when the initialization is not accurate. The following figures show how parameter estimation performs under such circumstances. Since the actual SOC is equivalent to 100%, deviations and convergence times are expected.

5.5.1 Capacity estimates

Plots showing capacity estimates from new and aged cell for test case 3.

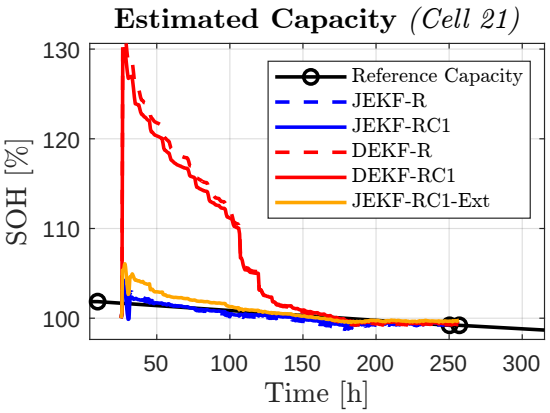

Figure 5.40: Estimated capacity for *new* cell in test case 3.

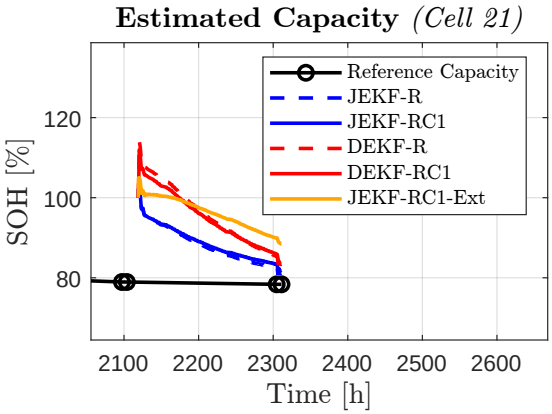

Figure 5.41: Estimated capacity for *aged* cell in test case 3.

5.5.2 Internal resistance Rint model

Plots showing resitance estimates from new and aged cell for test case 3, from Rint model for JEKF-R and DEKF-R.

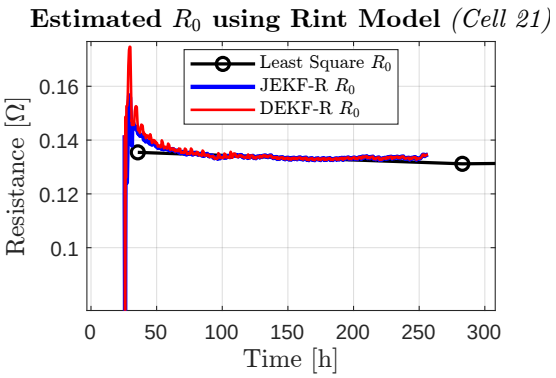

Figure 5.42: Estimated R_0 for *new* cell in test case 3 for JEKF-R and DEKF-R.

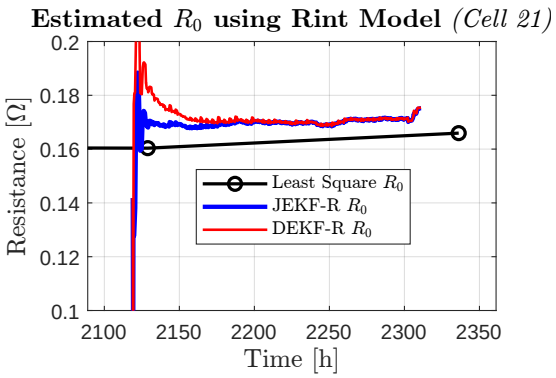

Figure 5.43: Estimated R_0 for *aged* cell in test case 3 for JEKF-R and DEKF-R.

5.5.3 Internal resistance RC1 model

Plots showing resitance estimates from new and aged cell for test case 3, from RC1 model for JEKF-R and DEKF-R.

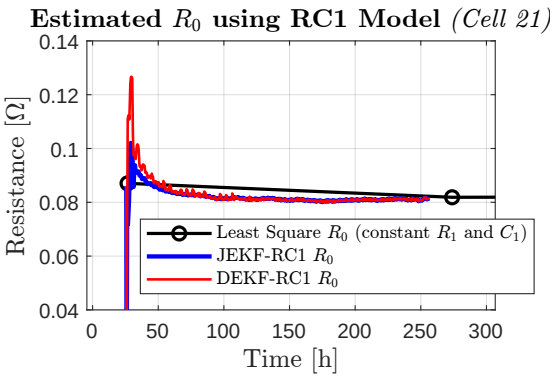

Figure 5.44: Estimated R_0 for *new* cell in test case 3 for JEKF-RC1 and DEKF-RC1.

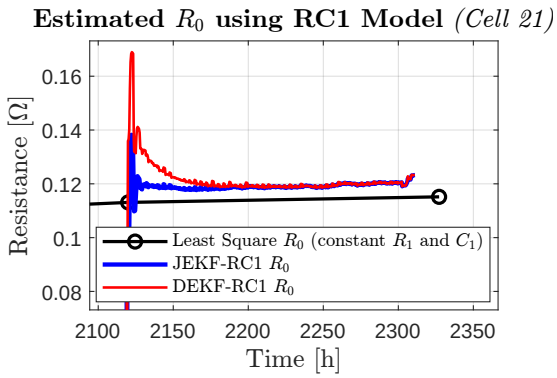

Figure 5.45: Estimated R_0 for *aged* cell in test case 3 for JEKF-RC1 and DEKF-RC1.

5.6 Computation time

Table 5.12 shows the results of average computation time per iteration using the setup described in Section 4.4. The most efficient filter for Matlab is the EKF-R, with JEKF-R closely following. EKF-RC1, JEKF-RC1, and JEKF-RC1-Ext also perform well, though they take slightly longer. Surprisingly, the DEKF, which theoretically involves simpler matrix operations than the JEKF, takes about twice as long as the JEKF.

Filter	Avg. Time per Iteration
EKF-R	$5.26 \cdot 10^{-6}$ s
EKF-RC1	$8.06 \cdot 10^{-6}$ s
JEKF-R	$6.59 \cdot 10^{-6}$ s
JEKF-RC1	$8.31 \cdot 10^{-6}$ s
JEKF-RC1-Ext	$7.96 \cdot 10^{-6}$ s
DEKF-R	$14.4 \cdot 10^{-6}$ s
DEKF-RC1	$18.1 \cdot 10^{-6}$ s

Table 5.12: Average computation time per iteration for the implemented Kalman filters using Matlab, and simulation setup from 4.4.

Chapter 6

Discussion

The discussion chapter is structured in the same order as the results are presented in the results chapter. First, the comparison of SOC estimates from primarily test case 1 is discussed in Section 6.1. Next, the results from the SOH estimators in test case 2 are discussed in Section 6.2. The discussion on the convergence of these estimators based on the results from test case 3 follows in Section 6.3. Finally, the computation time of the estimators is discussed before suggestions for further work are presented.

6.1 Comparison of SOC estimates - Test case 1

From test case 1 (Section 5.3), two parts of battery data from the same cell were simulated: one when the cell was new and the other when the cell was aged. A remarkable, yet expected, result was that with a new cell, where the battery parameters for all filters were correctly initialized, the performance of all filters, except for JEKF-R and DEKF-R, was within a 1% error margin for SOC estimation. It is noteworthy that both JEKF-RC1 and DEKF-RC1 performed better than EKF-RC1. One reason for this can be that the cell was continuously cycled for 200 hours, leading to significant changes in capacity and internal resistance during this timespan. These parameter changes are shown in Figure 5.14, where the estimated capacity and reference are plotted. From this figure, it is evident that the calculated capacity closely follows the reference capacity during the test phase.

However, it can be said that with updated battery parameters, a standard EKF solely for SOC estimation would be sufficient to obtain good SOC estimates. When it comes to voltage estimates from the different EKFs, there is a clear pattern as to which estimators perform best. Looking at the RMSE, estimators based on the RC1 model are the best. This is expected as they take the dynamic behavior of the battery into account.

The most notable results, however, come from the simulation on the aged cell. Figures 5.8 and 5.9 show the estimated SOC from this cell. It can be seen that there is a clear distinction in the precision of EKF compared to JEKF and DEKF. According to Table 5.4, the error for EKF-R and EKF-RC1 is at 3.56% RMSE, compared to JEKF and DEKF which still maintains around a 1% error margin RMSE. In other words, they remain much more stable in SOC estimation over time than EKF, which estimates SOC increasingly poorly as the cell parameters change due to aging.

For the voltage estimate on the aged cell, the trend is similar to SOC. EKF output estimates become worse, from 32.8 mV and 22.4 mV in RMSE in new condition to 38.5 mV and 54.4 mV RMSE in aged condition for EKF-R and EKF-RC1, respectively. This can be seen in Figure 5.7 and 5.13. The voltage estimate particularly depends on the parameters R_0 and R_1 and the SOC. Since the EKF-R and EKF-RC1 do not update these parameters, this leads to decreased accuracy in the SOC estimation.

6.2 Comparison of SOH estimators - Test case 2

The estimations performed in test case 2 (Section 5.4) show good results and precision. These tests were conducted on four different cells under varying ambient temperatures, meaning the cells underwent different test case scenarios. Therefore, variations between the cells, in capacity and internal resistance are expected. Since the voltage drop across a cell depends on Ohm's law, $U = R \cdot I$, cells experiencing higher currents will have a greater voltage drop and reach the 3.2V threshold sooner than cells with lower currents. The same applies if the internal resistance is high versus low. This means that cells with high current and high resistance will reach 3.2V early, resulting in a lower DOD, compared to cells with low current and low resistance which can discharge longer and thus achieve a higher DOD. This is further influenced by the fact that internal resistance is generally higher at lower temperatures, resulting in an even higher voltage drop. Consequently, in these test scenarios, the 3.2V threshold will be reached at different DOD levels. The cell with a high current and low temperature will have the lowest DOD, while the cell with the least current and higher ambient temperature will have the highest DOD. By this evaluation, cell 21 has the highest DOD and cell 20 will have the lowest DOD.

The results for the capacity estimation (SOH) show that the estimation for cell 21 is the best, with an RMSE error margin of around 1%. The estimation for cell 25 is also good, but with around a 2% error margin. These two cells operated at ambient temperatures of $40^{\circ}C$. Considering that cell 21 also experienced lower current flow and therefore operated more across the entire SOC, this would increase the precision of the estimation in terms of observability. Based on the results around the observability analysis (Section 4.2), which concludes that the more

nonlinear the OCV(SOC) relationship is, the greater the observability. When the cell operates within the entire OCV-SOC range, this property is maximized, and observability is increased. On the opposite end, the capacity estimation for cell 20, which experienced the *Skewed High* current test at room temperature, has a lower DOD. As discussed in the previous paragraph, this smaller DOD can lead to decreased observability, which can be confirmed by the bad SOH estimation, which is at 4% - 7% for this cell, compared to the 1% RMSE for cell 21.

For all cells, it can be seen that for each capacity check performed (the dots on the reference capacity curve), the capacity estimation approaches the true value (reference capacity). This can be compared to the fact that the DOD is 100% for these tests, and observability is greatly increased during these periods. It is also worth noting that all estimators tend to overestimate capacity.

Regarding resistance estimates, typically higher temperatures lead to lower internal resistance. The results from the test case do not show this effect. While all cells show a gradual increase in internal resistance over time, the increase is more pronounced for cells operated at $40°C$ compared to those at room temperature. This faster increase in resistance at higher temperatures is consistent with the theory for LIBs. The estimations from the various Kalman filters appear to be very similar to the individual estimates made by the least square estimator, both for the Rint model and the RC1 model.

The capacitance estimates show a significant difference for the cells operated at room temperature versus those operated at $40°C$. As the cell ages, changes in the internal structure can affect this capacitance, resulting in variations in the time constants of the RC circuit. The trend for the cells at room temperature (Figure 5.39 and 5.34) is clear; it first stabilizes at 800 F and then gradually decreases. The capacitance for the two cells at $40°C$ has a slightly different tendency, with a gradual increase in the first 1000 hours followed by a gradual decrease in the next 1000 hours (Figure 5.24 and 5.29) . This indicates that temperature has a significant impact on the behavior of the RC circuit parameters, potentially due to changes in the electrolyte conductivity and other temperature-dependent factors affecting the internal resistance and capacitance of the cells.

6.3 Convergence of estimation - Test case 3

From test case 3 (Section 5.5), where the SOC is initialized poorly in the filter, a clear difference between JEKF and DEKF can be observed. Since JEKF integrates all states and parameters into one system, it always maintains updated covariances among all the states. In contrast, DEKF divides states and parameters into a system consisting of two separate filters. Especially from the capacity estimates in Figure 5.40 and Figure 5.41, it is evident that the filters based on DEKF perform significantly worse, even though the capacity is correctly initiated. The reason for this

overestimation and overshoot could be that the filter is initiated to believe that SOC = 0%, when in reality it is 100%. The estimator will then assume there is even more available charge in the cell, leading to an overestimation in capacity. Since DEKF lacks the critical covariances to recognize this error, it takes over 100 hours to find the correct capacity (5.41). JEKF, on the other hand, oscillates a bit at the start but is quite stable around the correct capacity after less than 10 hours.

For the resistance estimates during this test case, the differences are not as big, though there is a difference, where JEKF performs solidly better than DEKF. The convergence time is not as significant here as for capacity and is around 20 hours, as seen from Figure 5.42 and Figure 5.43. DEKF also performs slightly worse on the aged cell than when the cell is new. Both show an overestimation of resistance at the beginning of the simulation. The estimation of resistance for the RC1 models is approximately the same as for the Rint model (Figure 5.44 and Figure 5.45). This shows the importance of correct initialization to maintain good estimates.

When estimators become this complex, it is crucial to consider whether it is necessary to estimate all parameters simultaneously. Estimating a larger number of parameters increases the overall uncertainty in the system. A key principle to keep in mind is to avoid estimating parameters that are already known or not essential.

6.4 Estimator computation time comparison

The computation time of the different estimators varies significantly. The tests conducted in this project were performed on a stationary PC with windows i7-10700 CPU @ 2.90GHz (Section 4.4 for setup), using Matlab, which is an advanced computation programming language optimized for matrix calculations among other tasks. An interesting result regarding computation time (Section 5.6, Table 5.12) is that DEKF takes about twice as long as JEKF. According to the theory [16], this method was recommended over JEKF because it increases the number of matrix operations while reducing the dimensions of the matrices involved, which should lead to a less time-consuming process overall. It would therefore be interesting to test the estimators on a less powerful computer or microcontroller for comparison.

The results for the computation time test show EKF-R as the fastest by far. JEKF-R is not far behind, taking up to $1.3 \cdot 10^{-6}$ seconds longer per iteration. It is worth noting that the increase in computation time is more affected by switching from the Rint model to the RC1 model (which adds 1 state) than by switching from EKF to JEKF (which adds 2 states). The reason for this is the more complex calculations required by the RC1 discretization compared to the random walk estimations introduced by JEKF.

6.5 Further work

Further work could involve testing nonlinear filters, such as Joint and Dual Unscented Kalman filters, to improve the accuracy of the estimations. Additionally, implementing and modeling temperature effects could be beneficial. This includes considering the impact of temperature on R_0 and the open-circuit voltage (OCV). Estimating sensor bias for current measurements using a random walk model can also enhance the system's robustness by accounting for potential drift in sensor readings over time, thereby ensuring more reliable long-term performance.

Implementing fault detection mechanisms for periods of missing data could involve resetting the filter and reinitializing with larger covariances to account for the increased uncertainty. Assessing the robustness of the initialization process and developing strategies for handling scenarios where the estimator does not converge could also be beneficial.

Testing the computation time on a smaller controller or a more dedicated battery management system would provide insights into computational performance and potential issues in practical applications.

Testing the estimators on other cell chemistries, such as LFP or NMC cells, is recommended to evaluate how changes in the OCV-SOC relationship and other factors affect the convergence and overall performance of the SOH estimators.

Additionally, testing the estimators on various current profiles, where the SOC varies more significantly as it would in real-world applications, could be valuable. For instance, testing between 30% and 80% SOC, or using entirely different profiles that represent actual battery usage scenarios, would provide a more comprehensive evaluation of the estimator's performance.

Chapter 7

Conclusion

This thesis has examined the implementation of three types of Kalman filters for battery health (SOH) and SOC estimation. The first filter implemented was the EKF, which focuses solely on SOC estimation. The second is the JEKF, an expanded version of the EKF that simultaneously estimates SOC and SOH by accounting for changes in capacity and internal resistance. The third filter is the DEKF, an advanced type of JEKF that also estimates both SOC and SOH. The primary goal was to determine if incorporating SOH estimation improves the accuracy of SOC estimates compared to estimators that only focus on SOC without considering parameter changes in the battery. Additionally, the thesis aimed to evaluate the precision and reliability of the SOH estimates provided by the estimators.

The key findings from the test cases indicate that for new LCO cells, the difference in SOC estimation accuracy between the EKF and the more advanced JEKF and DEKF is minimal. In these cases, the EKF has a slight advantage. In this scenario where the cell is new, all estimators achieved a SOC RMSE of approximately 1%. However, for aged cells, the JEKF and DEKF demonstrated superior performance, maintaining an error margin of around 1%, while the error margin for the EKF increased significantly to nearly 4%. This highlights the effectiveness of JEKF and DEKF in providing accurate SOC and SOH estimates for batteries as they age.

SOH estimates from JEKF and DEKF are accurate and stable, with fast convergence times, from a couple of hours to 50 hours. It is important to note that JEKF and DEKF require longer computation time than the EKF. Poor initialization also leads to more unstable SOH estimates and increased convergence times, particularly for DEKF, which was found to be less robust than JEKF.

This work indicates that DEKF, and especially JEKF, are effective estimators for the simultaneous estimation of SOC and SOH for LCO cells, providing reliable and efficient performance.

Bibliography

[1] K. Halse, "Comparison of Nonlinear Kalman Filter and Particle filter as State of Charge estimators on Lithium-ion batteries," en, no. no, p. 33, Jun. 2023.

[2] D. Dreyer Svendsen, *Implementation and Comparison of Nonlinear State of Charge Estimators using Equivalent Circuit Models for Two Lithium-Ion Battery Cell Chemistries*, 2023.

[3] M. Hutson. "The renewable-energy revolution will need renewable storage." (Apr. 2022), [Online]. Available: https://www.newyorker.com/magazine/2022/04/25/the-renewable-energy-revolution-will-need-renewable-storage (visited on 10/11/2023).

[4] T. Kim, W. Song, D.-Y. Son, L. K. Ono, and Y. Qi, "Lithium-ion batteries: Outlook on present, future, and hybridized technologies," en, *Journal of Materials Chemistry A*, vol. 7, no. 7, pp. 2942–2964, 2019, ISSN: 2050-7488, 2050-7496. DOI: 10.1039/C8TA10513H. [Online]. Available: https://xlink.rsc.org/?DOI=C8TA10513H (visited on 04/22/2024).

[5] L. L. Ping Shen Minggao Ouyang and J. Li, "State of charge, state of health and state of function co-estimation of lithium-ion batteries for electric vehicles," 2016.

[6] Z. Chen, H. Sun, G. Dong, J. Wei, and J. Wu, "Particle filter-based state-of-charge estimation and remaining-dischargeable-time prediction method for lithium-ion batteries," *Journal of Power Sources*, vol. 414, pp. 158–166, 2019, ISSN: 0378-7753. DOI: https://doi.org/10.1016/j.jpowsour.2019.01.012. [Online]. Available: https://www.sciencedirect.com/science/article/pii/S0378775319300138.

[7] M. Thingvad, L. Calearo, A. Thingvad, R. Viskinde, and M. Marinelli, "Characterization of NMC Lithium-ion Battery Degradation for Improved Online State Estimation," en, in *2020 55th International Universities Power Engineering Conference (UPEC)*, Torino, Italy: IEEE, Sep. 2020, pp. 1–6, ISBN: 978-1-72811-078-3. DOI: 10.1109/UPEC49904.2020.9209879. [Online]. Available: https://ieeexplore.ieee.org/document/9209879/ (visited on 04/29/2024).

[8] C. Liao, "Fundamentals of rechargeable lithium ion and beyond lithium ion batteries," Sep. 2021.

[9] L. Spitthoff, P. R. Shearing, and O. S. Burheim, "Temperature, Ageing and Thermal Management of Lithium-Ion Batteries," en, *Energies*, vol. 14, no. 5, p. 1248, Feb. 2021, ISSN: 1996-1073. DOI: 10.3390/en14051248. [Online]. Available: https://www.mdpi.com/1996-1073/14/5/1248 (visited on 05/30/2024).

[10] J. B. Goodenough. "How we made the li-ion rechargeable battery." (Mar. 2018), [Online]. Available: https://doi.org/10.1038/s41928-018-0048-6 (visited on 10/11/2023).

[11] H. Rubenbauer, "Battery energy storage systems – usable capacity regarding constant battery power values and associated minimum charge and discharge durations," Sep. 2017.

[12] G. L. Plett, *Battery management systems. Volume 1: Battery modeling: Gregory L. Plett*. Boston, Mass.: Artech House, 2015.

[13] P. Lin, Z. Wang, P. Jin, and J. Hong, "Novel polarization voltage model: Accurate voltage and state of power prediction," *IEEE Access*, vol. 8, pp. 92 039–92 049, 2020. DOI: 10.1109/ACCESS.2020.2993930.

[14] M. Winter and R. J. Brodd, "What are batteries, fuel cells, and supercapacitors?" *Chemical Reviews*, vol. 104, no. 10, pp. 4245–4270, 2004, PMID: 15669155. DOI: 10.1021/cr020730k. eprint: https://doi.org/10.1021/cr020730k. [Online]. Available: https://doi.org/10.1021/cr020730k.

[15] J. Vetter, P. Novák, M. R. Wagner, C. Veit, K. .-. Möller, J. O. Besenhard, M. Winter, M. Wohlfahrt-Mehrens, C. Vogler, and A. Hammouche, "Ageing mechanisms in lithium-ion batteries," *Journal of Power Sources*, vol. 147, no. 1, pp. 269–281, Sep. 2005, ISSN: 0378-7753. DOI: 10.1016/j.jpowsour.2005.01.006. [Online]. Available: https://www.sciencedirect.com/science/article/pii/S0378775305000832 (visited on 03/19/2024).

[16] G. L. Plett, *Battery management systems Volume 2, Equivalent-circuit methods* (Artech House Power engineering series), en. Boston: Artech house, 2016.

[17] H. Rubenbauer and S. Henningerb, "Definitions and reference values for battery systems in electrical power grids," Apr. 2017.

[18] Z. P. Wenlu Zhou Yanping Zheng and Q. Lu, "Review on the battery model and soc estimation method," Sep. 2021.

[19] G. L. Plett, *Battery Management Systems: Volume 1 - Battery Modeling*. Artech House, Massachusetts, United States of America, 2015.

[20] M. Pattnaik, M. Badoni, and Y. Tatte, "Application of Gaussian-sequential-probabilistic-inference concept based Kalman filter for accurate estimation of state of charge of battery," en, *Journal of Energy Storage*, vol. 54, p. 105 244, Oct. 2022, ISSN: 2352152X. DOI: 10.1016/j.est.2022.105244. [Online]. Available: https://linkinghub.elsevier.com/retrieve/pii/S2352152X22012439 (visited on 04/04/2024).

[21] E. Brekke, *Fundamentals of Sensor Fusion*. 2023.

[22] A. Rouhani and A. Abur, "Observability Analysis for Dynamic State Estimation of Synchronous Machines," en, *IEEE Transactions on Power Systems*, vol. 32, no. 4, pp. 3168–3175, Jul. 2017, ISSN: 0885-8950, 1558-0679. DOI: 10.1109/TPWRS.2016.2614879. [Online]. Available: http://ieeexplore.ieee.org/document/7581045/ (visited on 04/13/2024).

[23] H. K. Khalil, *Nonlinear systems*, eng, Pearson new internat. ed., 3. ed. Harlow: Pearson Education, 2014, ISBN: 978-1-292-03921-3.

[24] G. Plett, "Extended Kalman filtering for battery management systems of LiPB-based HEV battery packsPart 1. Background," en, *Journal of Power Sources*, Jun. 2004, ISSN: 03787753. DOI: 10.1016/S0378-7753(04)00359-3. [Online]. Available: https://linkinghub.elsevier.com/retrieve/pii/S0378775304003593 (visited on 02/09/2024).

[25] S. Haykin, *Kalman filtering and neural networks* (Adaptive and learning systems for signal processing, communications, and control), eng. New York: Wiley, 2001, ISBN: 978-0-471-36998-1.

[26] J. Van Lint, S. P. Hoogendoorn, and A. Hegyi, "Dual EKF State and Parameter Estimation in Multi-Class First-Order Traffic Flow Models," en, *IFAC Proceedings Volumes*, vol. 41, no. 2, pp. 14 078–14 083, 2008, ISSN: 14746670. DOI: 10.3182/20080706-5-KR-1001.02383. [Online]. Available: https://linkinghub.elsevier.com/retrieve/pii/S1474667016412486 (visited on 02/05/2024).

[27] D. Simon, *Optimal State Estimation: Kalman, H_inf, and Nonlinear Approaches*, en, 1st ed. Wiley, May 2006. (visited on 04/05/2024).

[28] L. Ling and Y. Wei, "State-of-Charge and State-of-Health Estimation for Lithium-Ion Batteries Based on Dual Fractional-Order Extended Kalman Filter and Online Parameter Identification," en, *IEEE Access*, vol. 9, pp. 47 588–47 602, 2021, ISSN: 2169-3536. DOI: 10.1109/ACCESS.2021.3068813. [Online]. Available: https://ieeexplore.ieee.org/document/9386077/ (visited on 02/19/2024).

[29] T. O. Hodson, "Root-mean-square error (RMSE) or mean absolute error (MAE): When to use them or not," English, *Geoscientific Model Development*, vol. 15, no. 14, pp. 5481–5487, Jul. 2022, ISSN: 1991-959X. DOI: 10.5194/gmd-15-5481-2022. [Online]. Available: https://gmd.copernicus.org/articles/15/5481/2022/ (visited on 05/11/2024).

[30] J. Nocedal and S. J. Wright, *Numerical Optimization*, 2nd ed. Springer Science, 2006.

[31] G. L. Plett, "Extended Kalman filtering for battery management systems of LiPB-based HEV battery packs Part 2," en, *Journal of Power Sources*, vol. 134, no. 2, pp. 262–276, Aug. 2004, ISSN: 03787753. DOI: 10.1016/j.jpowsour.2004.02.032. [Online]. Available: https://linkinghub.elsevier.com/retrieve/pii/S037877530400360X (visited on 02/09/2024).

[32] S. Zhao, S. R. Duncan, and D. A. Howey, "Observability analysis and state estimation of lithium-ion batteries in the presence of sensor biases," en, *IEEE Transactions on Control Systems Technology*, vol. 25, no. 1, pp. 326–333, Jan. 2017, ISSN: 1063-6536, 1558-0865. DOI: 10.1109/TCST.2016.2542115. [Online]. Available: http://arxiv.org/abs/1510.06553 (visited on 04/15/2024).

[33] B. Bole, C. S. Kulkarni, and M. Daigle, "Adaptation of an Electrochemistry-based Li-Ion Battery Model to Account for Deterioration Observed Under Randomized Use," en, 2014.

[34] B. Bole, C. Kulkarni, and M. Daigle, *Randomized Battery Usage Data Set*, https://www.nasa.gov/intelligent-systems-division/discovery-and-systems-health/pcoe/pcoe-data-set-repository/, Accessed: 2024-03-14, Moffett Field, CA, 2013.

[35] M.-K. Tran, A. DaCosta, A. Mevawalla, S. Panchal, and M. Fowler, "Comparative Study of Equivalent Circuit Models Performance in Four Common Lithium-Ion Batteries: LFP, NMC, LMO, NCA," en, *Batteries*, vol. 7, no. 3, p. 51, Sep. 2021, ISSN: 2313-0105. DOI: 10.3390/batteries7030051. [Online]. Available: https://www.mdpi.com/2313-0105/7/3/51 (visited on 05/03/2024).

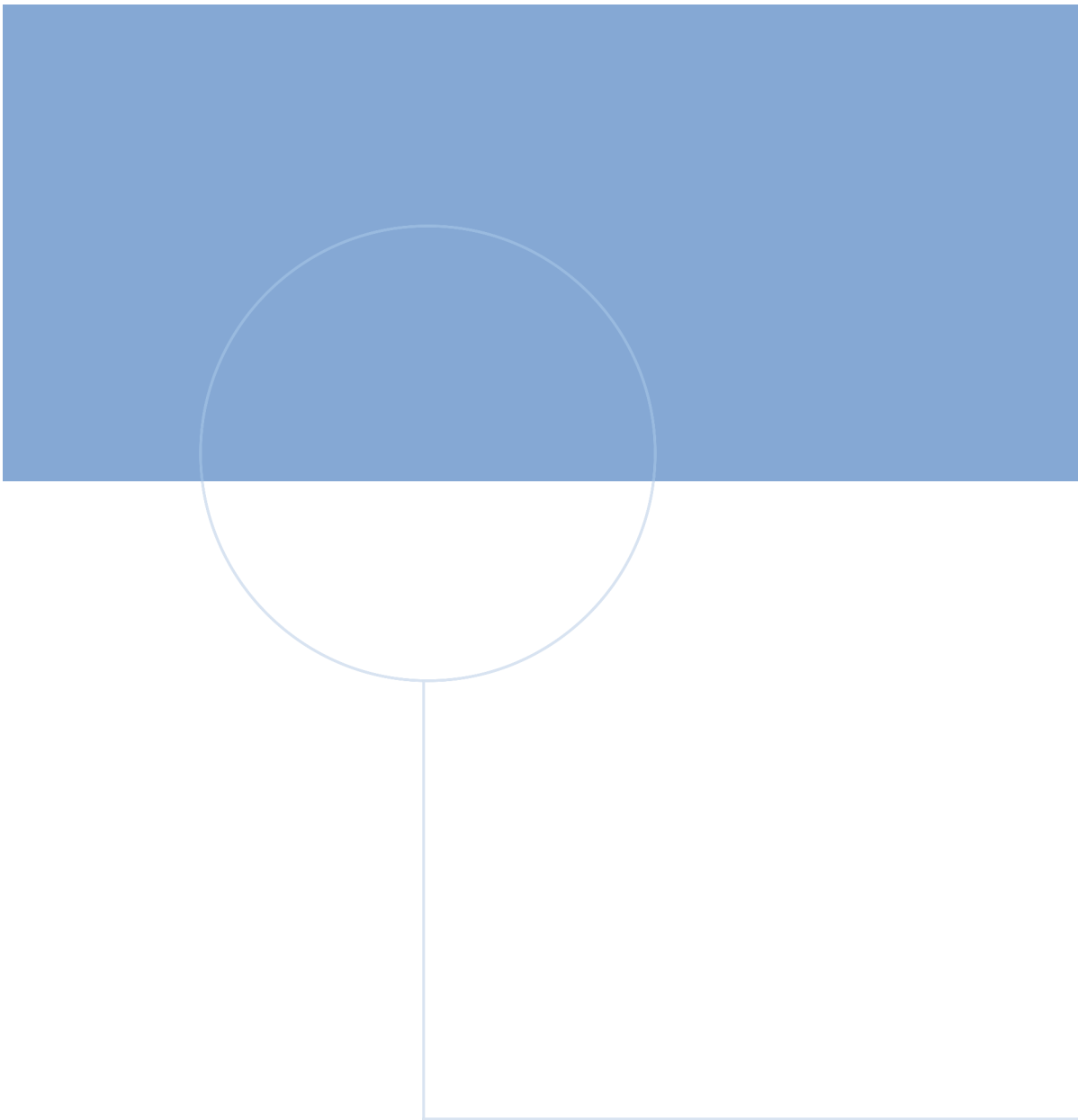

NTNU

Norwegian University of
Science and Technology